Department of Physics
Indian Institute of Technology Guwahati
Ph.D. Thesis

Accretion-ejection mechanism from advective accretion disc around rotating black holes

Md Ramiz Aktar

Thesis Supervisor: Dr. Santabrata Das

October, 2018.

Accretion-ejection mechanism from advective accretion disc around rotating black holes

A Thesis submitted for the award of the degree of
Doctor of Philosophy in Physics
by

Md Ramiz Aktar

Thesis Supervisor: **Dr. Santabrata Das**

Department of Physics
Indian Institute of Technology Guwahati
Guwahati - 781039, Assam, India

October, 2018

Statement

The work contained in the thesis entitled "**Accretion-ejection mechanism from advective accretion disc around rotating black holes**" has been carried out at the Department of Physics, Indian Institute of Technology Guwahati, India by me under the supervision of Dr. Santabrata Das. The material of this thesis has not been submitted elsewhere for any other degree. Works presented in the thesis are all my own unless referenced to the contrary in the text.

(Md Ramiz Aktar) Date:
October, 2018
Department of Physics
Indian Institute of Technology Guwahati
Guwahati - 781039, India

Disclamer

The bibliography included in this thesis is, by no means complete but contains the ones which are consulted thoroughly by me. I apologize for inadvertently missing out some of the research papers, review articles and other scientific documents pertaining to the focus of this thesis which should also have been cited. For illustration purpose some of the figures in this thesis are taken from other sources and properly cited.

Certificate

It is certified that the work contained in the thesis entitled "**Accretion-ejection mechanism from advective accretion disc around rotating black holes**" by Mr. Md Ramiz Aktar (Roll no.-126121003), a Ph.D. student of the Department of Physics, Indian Institute of Technology Guwahati is carried out under my supervision and has not been submitted elsewhere for the award of any other degree.

(Dr. Santabrata Das) Date:
October, 2018
Associate Professor
Department of Physics
Indian Institute of Technology Guwahati
Guwahati - 781039, India

To

All My Dropout Childhood Friends...

Acknowledgement

First and foremost, I express my sincere gratitude to my thesis supervisor Dr. Santabrata Das for his constant guidance, continuous support and complete freedom to explore new scientific understandings during my Ph.D tenure. I have been always motivated by his expert supervision and dedication for work. I am also thankful to him for giving me the opportunity to be involved in different types of problems and collaborations that helped me a lot to increase my experience and knowledge about the subject.

I would like to thank Dr. Anuj Nandi, one of my collaborators, for his continous support and valuable discussions to improve the quality of research works. I would like to express my sincere gratitude to Prof. Toru Okuda for helping me to learn various aspects of numerical simulations. I would also like to thank Mr. Sreehari Harikesh for his observational inputs, technical support and fruitfull discussions. I am fortunate enough to interact with Prof. Sandip Chakrabarti and Dr. Indranil Chattopadhyay during my visit in conferences. I have always enrichenced with their theoretical and observational opinion about the subject.

I would like to acknowledge my doctoral committee members - Prof. Subhradip Ghosh, Dr. Dipankar Bandopadhyay and Dr. Udit Raha for their useful suggestions to improve my scientific understanding during the yearly assessments of my research work. I also thank all HODs (Prof. Saurabh Basu, Prof. Poulose Poulose and Prof. Subhradip Ghosh) for their various academic help during my Ph.D. I would like to thank all the technical assistants, academic and non-academic staff of the department who helped me in various ways during my research period. I specially thank Basab-da for his support in different computer related issues. I am also thankful to Param Ishan, IIT Guwahati for the supercomputer facility. I thank the department of Physics IIT Guwahati, India for allowing me to utilize Newton cluster, funded under the FIST programme by DST, India.

I would like to thank my group members, Dr. Biplob Sarkar and Mr. Indu Kalpa Dihingia for their continuous support and wonderful friendship. I have learned a

lot from them about the various aspects of the fields. I would also like to thank Dr. Susmita Ghosh, Priyadarshini Kapri, Indranil Banerjee and Dipanweeta Bhattacharyya for their constant help and encouragement during my initial period of Ph.D.

I am fortunate enough to have a great friend circle, seniors like Bishu-da, Himangsu-da, Tapas-da, Bappa-da, Kartik-da, Arnab-da, Ramesh-da, Bhargav-da, Amit-da. I am extremely lucky to have my friends like Kallol, Sourav, Ashis, Abhijit, Koushik, Sudin, Atanu, Noor, Sahu, Rahul, Srikrishna, and Anabil-da. I had lot of great memories with them which I will never forget. I would like to thank my batchmates Venki, Bibhuti, Ram Kumar, Prahlad and my juniors Sanjib, Sayan, Pankaj, Pratap, Sumit, Karuna, Rishav, Sneha, Sheuly, Dipti and others. Most importantly, I would like to thank all my school friends like Imrul, Biswa, Sukanta, Newton, Sahadeb, Bhola, Biswa(M), Sanjay, Tirtha, Souvik, Anirban, Umesh-da and college friends like Sahabuddin, Anindya, Sabuj, Suman, Kapil, Somnath, Poulomy, Arpita and others for their wonderful friendship throughout the years.

As a filmgoer, I would like to thank all the members of Cinephile Production, Krishnanjan, Basabendu, Srimoy, Bony, Sunando-da and Ashmita-di. Filmmaking, editing and cinematography always gives me immense pleasure and happiness.

I am extremely fortunate to have teachers like late Anil kumar Karmakar, late Brahmamohon Roy, Pradip Rakshit, Pabitra Saha, Hirok Roy, Dr. Parthosarathi Majumdar and Dr. Debapriya Shyam.

I would like to thank my elder brother Washim Aktar for motivating me to continue higher studies after B.Sc and constant support during tough times. I would like to thank my uncle Abdul Alil for his financial support during my early education. My special thanks goes to my uncle Abdul Khalil and aunt Rexina Bibi for their love, support and motivation in many ways. I would also like to thank my two sisters Rubina and Lajina, my cousins Feroz, Babul Aktar, Tuhina, Tasmi, Wakkiya, Hadid, Javed, niece Barsa, Aayat and nephew Afrid for their unconditional love.

Finally, I would like to thank all my family members, specially my parents and grand parents for their unconditional love, support, freedom and sacrifices for me.

October, 2018 Md Ramiz Aktar

Abstract

Powerful jets and outflows are commonly observed in accreting black hole systems including active galactic nuclei (AGNs) and X-ray binaries (XRBs). In spite of the rigorous investigations carried out in both theoretical as well as observational fronts, the physical mechanism of jet generation and its powering processes are still remain elusive. In this context, the earlier theoretical investigations predicted that the powering of jets may be due to the spin of the black holes. However, the contradictory claims have been made in the observational front. Motivating with this, we investigate the effect of spin on mass loss from the accretion disc around rotating black holes.

In the first work, we investigate the effect of spin on the mass outflow rates from a steady, advective, inviscid, geometrically thin accretion flow around a rotating black hole. For this purpose, we adopt pseudo-Kerr potentials to mimic the space-time geometry around rotating black holes. We observe that the accretion-ejection solutions exist for prograde as well as retrograde flow. We separate the shock parameter spaces in terms of flow energy and angular momentum for various spin and adiabatic index values. We find that a wide range of inflow parameters admits shock solutions. Further, we calculate maximum outflow rates in terms of spin of the black holes. Interestingly, we observe a weak correlation between the spin and the maximum outflow rates from our model. Finally, we apply our accretion-ejection model to estimate the kinetic jet power for various black hole sources.

In the second work, we consider a steady, dissipative, geometrically thin accretion flow around a rotating black hole. Here also we consider pseudo-Kerr potentials for mimicking the space-time geometry around rotating black holes. We obtain the global shocked accretion solutions in terms of viscosity parameters around rotating black holes. We find that the shock waves exist for a wide range of dissipative parameters. We also calculate critical limit of viscosity parameters in terms of spin of the black holes that permits shock solutions. We observe that the critical viscosity parameter decreases with the spin of the black hole. Further, we estimate maximum outflow rates in terms of viscosity parameter. We also calculate the maximum QPO frequency in terms of the black hole spin using our accretion-ejection model. Finally, we apply our formalism to constrain the spin parameter of the black hole source GRO J1655-40.

In the third work, we perform a comparative study of a steady, dissipative, geometrically thin accretion flow around a rotating black hole using three pseudo-

Kerr potentials. While doing this, we solve the governing equations for dissipative accretion flow around the rotating black hole. We observe that a wide range of flow parameters admits shock transition in the accretion flow variables for all the potentials. We calculate the critical viscosity parameters for shocks in terms of spin of the black hole for all the potentials. We observe that in case of weakly rotating black holes, the critical viscosity parameters for all the pseudo-potentials agrees quite well, but differs considerably from each other for rapidly rotating black holes. We apply our accretion-ejection model to compute the kinetic jet power and then compare it with the observed radio jet power of the black hole X-ray binaries (BH-XRBs). We indicate that BH-XRBs along the 'outliers' track seems to be rapidly rotating.

In the fourth work, we study the dynamics of advective inviscid accretion flow using time-dependent hydrodynamical simulation around rotating black holes. With the appropriate choice of the input parameters, we find that inflowing matter passes through the shock wave which at the same instance also oscillates. Due to the shock compression, the post-shock corona (hereafter PSC) usually becomes very hot and dense and therefore, acts as a source of high energy radiations. When PSC modulates, the high energy photon flux coming out from PSC is also oscillates that eventually exhibits Quasi-periodic Oscillations (QPOs). When PSC executes very fast oscillation, it demonstrates high frequency QPOs (HFQPOs). We carry out the numerical investigation of HFQPOs for various sets of input parameters and compare our results with the observation of *LAXPC/AstroSat* and *RXTE* for galactic black hole source GRS 1915+105. Based on this comparative study, we indicate the possible range of mass and spin values of this source.

List of Publications

Journal Publications

1. **Ramiz Aktar**, Santabrata Das, Anuj Nandi, *Mass-loss from advective accretion disc around rotating black holes*, Monthly Notices of the Royal Astronomical Society **453**, 3414 (2015)*

2. **Ramiz Aktar**, Santabrata Das, Anuj Nandi, H. Sreehari, *Estimation of mass outflow rates from dissipative accretion disc around rotating black holes*, Monthly Notices of the Royal Astronomical Society **471**, 4806 (2017)*

3. **Ramiz Aktar**, Santabrata Das, Anuj Nandi, H. Sreehari, *Advective accretion flow properties around rotating black holes - application to GRO J1655-40*, Journal of Astrophysics and Astronomy **39**, 17 (2018)*

4. A. Nandi., S. Mandal., H. Sreehari., D. Radhika., S. Das., I. Chattopadhyay., N. Iyer., V. K. Agrawal., **Ramiz Aktar** *Accretion Flow Dynamics During 1999 Outburst of XTE J1859+226 - Modeling of Broadband Spectra and Constraining the Source Mass*, Astrophysics and Space Science **363**, 90 (2018)

Pre-Publications

5. **Ramiz Aktar**, Anuj Nandi, Santabrata Das, *Accretion-ejection in rotating black holes: a model for 'outliers' track of radio-X-ray correlation in X-ray binaries*, (Submitted to Astrophysics and Space Science, Under Review)*

Publications marked with *are included in the thesis

6. Toru Okuda, Chandra B. Singh, Santabrata Das, **Ramiz Aktar**, Anuj Nandi, Elisabete M. de Gouveia Dal Pino, *A possible model for the long-term flares of Sgr A**, (Submitted to Publications of the Astronomical Society of Japan)

7. Santabrata Das, Anuj Nandi, **Ramiz Aktar** , Indu Kalpa Dihingia, H. Sreehari, Toru Okuda, Samir Mandal, *Simulation of High Frequency Quasi-periodic Oscillations (HFQPOs) around rotating black holes*, (To be submitted soon)

Conference Publications

8. Santabrata Das, **Ramiz Aktar**. *Dynamically induced shock oscillation in the accretion disc around black holes.* Recent Trends in the Study of Compact Objects (RETCO-II): Theory and Observation. ASI Conference Series, 2015, **12**, 47-50, (2015).

9. **Ramiz Aktar** , Santabrata Das, *Estimation of the mass outflow rates around rotating black holes*, Recent Trends in the Study of Compact Objects (RETCO-II): Theory and Observation. ASI Conference Series, 2015, **12**, 89-90, (2015).

National Schools/workshops/Conferences attended

1. **IUCAA Sponsored Introductory Workshop on Relativistic Astrophysics (IWRAP)**, 21-23 August, 2014, Department of Physics, Gauhati University, Guwahati.

2. The conference, **Hard X-ray Astronomy: Astrosat and Beyond**, International Center, Goa, September 24-26, 2014, organized by TIFR.

3. National conference on **Recent Trends in the Study of Compact Objects: Theory and Observation (RETCO-II)**, May 6-8, 2015, ARIES, Nainital, India.

4. One day symposium on **100 years of General Relativity: Where do we stand?**, 13 February, 2016, Department of Physics, IIT Guwahati.

5. The conference, **Wide Band Spectral and Timing Studies of Cosmic X-ray Sources**, January 10-13, 2017, organized by TIFR, Mumbai, India.

6. **29th meeting of the Indian Association for General Relativity and Gravitation (IAGRG)**, May 18-20, 2017, organized by Department of Physics, IIT Guwahati, Assam, India.

7. National conference on **Recent Trends in the Study of Compact Objects: Theory and Observation (RETCO-III)**, June 5-7, 2017, Indian Institute of Space Science and Tech- nology (IIST), India.

Contents

List of Figures

List of Tables

Chapter 1

Introduction

1.1 Accretion process as power source

The extraction of gravitational potential energy through accreting matters is considered to the compelling mechanism to power the astrophysical sources in the universe. When matter falls onto a compact objects under the free-fall condition from infinity, it gains kinetic energy from the gravitational potential energy. More specifically, as protons fall from infinity onto a star of mass M and radius R, we have

$$\frac{1}{2}m_p v_{\rm ff}^2 = \frac{GMm_p}{r}, \tag{1.1}$$

where m_p, G and $v_{\rm ff}$ are the mass of the proton, gravitational constant and free-fall velocity, respectively. Now, when matter reaches the star surface i.e., $r = R$, it decelerates and releases away its kinetic energy in the form of thermal energy. As the star starts accreting matter at a rate $\dot{m}$, the rate of dissipation of kinetic energy of the matter at the star surface (commonly known as the luminosity of the source L) is given by,

$$L = \frac{1}{2}\dot{m}v_{\rm ff}^2 = \frac{GM\dot{m}}{R}. \tag{1.2}$$

For convenience, luminosity of the source can be expressed using Schwarzschild radius ($r_g = 2GM/c^2$, c being the speed of light) as $L = 0.5 \times \dot{m}c^2(r_g/R)$. Therefore, luminosity of the source can be expressed in terms of the rest mass energy as $L = \eta\dot{m}c^2$, where η stands for the conversion efficiency of the rest mass energy. This clearly indicates that the efficiency of energy conversion directly depends on the compactness (M/R) of the star. In case of white dwarf, $\eta \sim 3 \times 10^{-4}$, where

$M = M_\odot$ and $R = 5 \times 10^6$ m. For a typical neutron star of $M = M_\odot$ and $R = 15$ km, $\eta \sim 0.1$. For a black hole, η strictly depends on its spin angular momentum values: for Schwarzschild black hole, $\eta = 0.06$ and for maximally rotating black holes, $\eta = 0.426$ [5, 6].

Next, we consider the fully ionized infalling matter on to a star mainly consists of hydrogen. The main source of energy of the star comes from the fusion reaction i.e., the conversion of hydrogen to helium (H→He). The outward radiation pressure force is developed due to the Thompson scattering radiation by the electrons in the plasma. This outward radiation pressure force balances the inward gravitational force acting on the electron-proton pair. So, the gravitational force ($f_{\rm grav}$) acting on the electron-proton pair at a distance r is given by,

$$f_{\rm grav} = \frac{GM(m_p + m_e)}{r^2} \approx \frac{GMm_p}{r^2}. \tag{1.3}$$

The plasma is neutral in nature and the radiation pressure force acts mostly on the electrons. Hence, the momentum imparted on the electron by the photon in each collision is $p = h\nu/c$, where h, and ν are the Planck's constant and the frequency of photon, respectively. Accordingly, the radiation force exerts on the electron is $f_{\rm rad} = \sigma_T N_{\rm ph} p$, where $N_{\rm ph}$ and σ_T are the photons flux and Thomson scattering cross-section, respectively. At a distance r from the source, the photons flux can be estimated as $N_{\rm ph} = L/4\pi r^2 h\nu$ and therefore, $f_{\rm rad} = \sigma_T L/4\pi r^2 c$. Equating the inward gravitational force and outward radiation pressure force, we get

$$\begin{aligned} \frac{\sigma_T L_E}{4\pi r^2 c} &= \frac{GMm_p}{r^2}, \\ L_{\rm E} &= \frac{4\pi GMm_p c}{\sigma_T}, \end{aligned} \tag{1.4}$$

where $L_{\rm E}$ refers the Eddington luminosity. In particular, it is the maximum luminosity that a spherically symmetric source of mass M can emit in the steady state. It may be noted that Eddington luminosity remains independent on the radius r, but depends only on the mass M of the source. Therefore, it can be written in terms of mass by introducing Schwarzschild radius as

$$L_{\rm E} = \frac{2\pi r_g m_p c^3}{\sigma_T} = 1.3 \times 10^{38} \left(\frac{M}{M_\odot}\right) \text{erg sec}^{-1}. \tag{1.5}$$

It is noteworthy to mention that the X-ray luminosities reach the Eddington limit for the sources masses as $1 - 10M_\odot$ source. However, in case of non-steady state

sources, namely supernovae explosion etc., the luminosities can exceed far beyond the Eddington limit.

1.2 Accretion disc models

Considering the aspects discussed in §1.1, almost eighty years ago, Hoyle & Lyttleton (1939) [7] first initiated to study the accretion processes considering pressure-less matter around moving star. Subsequently, Bondi & Hoyle (1944) [8] and Bondi (1952) [9] included gas pressure in their study and developed the spherical accretion solution ignoring the angular momentum of the inflowing matter. Unfortunately, these simplistic models were unable to explain the high luminosities of quasars and AGNs. Later, the era of modern accretion disc theory has begun with two classical articles, one by Shakura & Sunyaev (1973) [10] (hereafter SS73) and the general relativistic version of it by Novikov & Thorne (1973) [11] (hereafter NT73). In these works, accreting matter is assumed to posses angular momentum while falling towards the black hole. In fact, because of the angular momentum, the inflowing matter starts to rotate around the black hole and eventually forms a disc-shaped geometry, known as accretion disc. In the below, we describe various accretion disc models around black holes.

1.2.1 Shakura-Sunyaev Disc (SSD)

The foundation of first complete accretion disc physics has been started by Shakura & Sunyaev (1973) [10], popularly known as 'standard disc' model. Later, Novikov & Thorne (1973) [11] generalized this disc model by extending it using general relativistic formalism. In this model, the accretion disc is assumed to be geometrically thin and inside the disc, the inflowing matter obeys the Keplerian angular momentum distribution where the radial velocity of the accreting matter effectively becomes smaller compared to the the free-fall velocity. Moreover, the transport of the angular momentum of the flow is guided by the viscous stress tensor which is assumed to be proportional to the vertically-averaged pressure as

$$W_{x\phi} = \alpha W, \tag{1.6}$$

where, α denotes the proportionality constant and W is the vertically integrated pressure. Further, in this model, it is assumed that the accreted gas is cooled efficiently resulting the disc to become radiatively efficient. Because of this, all the

radiative energy is dissipated through viscous dissipation energy $Q_{\rm vis}$ as,

$$Q_{\rm rad} = Q_{\rm vis} >> Q_{\rm adv}, \tag{1.7}$$

where $Q_{\rm rad}$ and $Q_{\rm adv}$ denote the energy radiated and advected in the disc, respectively. With this, the effective temperature of the disc becomes quite low for this model and is expressed as,

$$T_{\rm eff} = (6 \times 10^7)\ M_{\rm BH}^{-1/4}\ \dot{M}^{1/4}\ r^{-3/4}, \tag{1.8}$$

where $\dot{M}$ is the mass accretion rate in Eddington unit and $M_{\rm BH}$ refers the mass of the black hole, respectively. Interestingly, observational study indicates that the characteristic temperature of the radiation often exceeds its value as 10^9 K for the cases of both stellar-mass and supermassive black holes. Therefore, this model bears limitation to explain the origin of the observed hard X-ray radiations although it can successfully accounts for the black body component of the emitted spectra for the black hole sources.

1.2.2 SLE

In order to study the low accretion rate flow, a two temperature accretion model was proposed by Shapiro, Lightman, and Eardley (1976) [12] (SLE). In this model, accreting plasma is considered to be optically thin and also composed of two-temperature flow in the vicinity of the black hole, with the ions being significantly hotter than the electrons. The electrons are cooled by Comptonization of soft photons and achieve the temperatures up to $\sim 10^8 - 10^9$ K. The observed spectra in accreting black holes containing both soft and hard X-ray and γ-ray power-law components can be explained by the co-existence of both hot (SLE) and cold (SSD) disc. But, the major disadvantage of this model is that the accreting gas is thermally unstable [13]. At equilibrium, when the temperature of the electrons is slightly perturbed, the gas either cools catastrophically to the thin disc solution or heats up catastrophically without bound.

1.2.3 Slim Disc

Abramowicz et al. (1988) [14] first showed that a new kind of accretion disc solution is possible at moderately super-Eddington rates. In particular, when the mass accretion rate is close to Eddington or super-Eddington rate, the radiation escape-time

exceeds the time scale of accretion process [15]. As a result, a part of the energy due to radiation is advected into the black hole. Accordingly, the energy balance equation takes the following form as,

$$Q_{\rm vis} = Q_{\rm rad} + Q_{\rm adv}. \tag{1.9}$$

In this model, the flow becomes optically thick and the total pressure of the accreting plasma is primarily dominated by the radiation pressure. Interestingly, because of the presence of advection, the flow now becomes stable. Here, the transonic flow enters into the black hole after crossing the critical point with sub-Keplerian angular momentum and this model is commonly known as 'Slim Disc' model. The local vertical thickness of this disc is computed from the solution of this model. Usually, it produces small thickness for low accretion rate and tends to become of the order of radial distance ($h \sim r$) as the accretion rate approaches to the critical Eddington limit. What is more is that the relativistic version of this model is also being investigated in the literature [16, 17]. Unfortunately, it becomes difficult to calculate the radiation spectrum when the disc is optically thick at low accretion rates.

1.2.4 ADAF

Ichimaru (1977) [18] first investigated a new kind of accretion solution, named as advection-dominated accretion flow (ADAF). In this disc model, the radiative cooling remains inefficient and a large amount of accretion energy due to viscous dissipation is advected with the accreting gas as stored entropy. Subsequently, more rigorous investigation of the model has been carried out [19–27]. The model has been applied to various black hole systems e.g., supermassive black hole (Sgr A*), low-luminosity AGNs (LLAGNs), and BH-XRBs in their hard and quiescent states. There are two variants of ADAF model: one is the adiabatic inflow-outflow solution (ADIOS) and the other is the convection-dominated accretion flow (CDAF). These two models are developed based on two completely different physical phenomena, namely outflow generation and convection mechanism.

- **ADIOS**

Blandford & Begelman (1999) [28] first proposed the advection dominated inflow-outflow (ADIOS) accretion model based on 1D and 2D self-similar solutions. In this model, the inward decrease of inflow mass accretion rate ($\dot{M}_{\rm in}$) is continue to happen

due to the mass loss from the disc in the form of wind [28, 29]. Here, the accretion rate is assumed to satisfy the power law dependence on radial coordinate as $\dot{M}_{\rm in} \propto r^s$ with s being a parameter in the range $0 \leq s < 1$. Recently, Begelman (2012) [30] proposed a new version of ADIOS where they considered the inflow and outflow zones on an equal footing and found that s goes to unity.

• **CDAF**

Convection dominated accretion flow (CDAF) has been introduced by [31–34] and this model is developed based on the fact that the hot inflowing matter is convectively unstable [20]. Moreover, in this model, the inward angular momentum is transported by convection which roughly cancels the outward transport of angular momentum via viscous stress. In addition, in this model, the gas constantly moves in and out as inflowing and outflowing matter due to the production of turbulent convective eddies although, in reality, the outflowing gas never really escapes from the disc and the overall the net accretion rate remains small.

1.2.5 TCAF

In this Section, we discuss one of the most successful accretion disc model, known as two-component advective flow (TCAF) model proposed by Chakrabarti & Titarchuk (1995) [35] (hereafter CT95). This model was developed based on the theoretical works of Chakrabarti (1990) [36] which comprises two disc components where a high viscosity standard Keplerian disc component resided in the disc equatorial plane is flanked by the low viscosity sub-Keplerian halo component (CT95). During accretion, the rotating inflowing matter experiences a virtual barrier due to the repulsive centrifugal force against gravity in the vicinity of the black hole. Depending on the flow parameters, such a virtual barrier may trigger the discontinuous transition of the flow variables in the form of the shock waves (see §1.7). In reality, accretion flow containing shock wave possesses high entropy content and therefore, advective accretion flow prefers to pass through the shock as it is thermodynamically favorable [37–39]. Due to the shock compression, the post-shock flow becomes hot as well as dense and acts as an effective boundary around the black hole, known as post-shock corona (equivalently Compton corona, hereafter PSC). It is noteworthy to mention that accretion flow harbors shock wave when the standing shock conditions are satisfied [40] . Moreover, needless to mention that the shock properties strictly depend on the various flow parameters like specific energy, specific angular momentum, heating and cooling mechanisms present in the flow. In addition, a

part of the inflowing matter is deflected by PSC and then further driven out in the vertical direction by the excess thermal gradient force across the shock, producing bipolar outflows [41–45].

In this model, a part of the soft photons emitted from the Keplerian disc is intercepted by the hot electrons of PSC (sub-Keplerian flow) and further reprocessed by the inverse-Compton scattering mechanism to emerge out as hard X-ray radiations. Therefore, the emitted radiation spectrum carries the signature of both the disc components [35]. In a way, the accretion rates of disc and halo components collectively determine the characteristics of the spectrum. Eventually, the smooth state transitions are successfully explained by suitably tuning the mass accretion rates of the two-component disc [46–48, and references therein]. On the other hand, when shock oscillates, the hard X-ray radiations coming out from PSC also modulates. This possibly causes the Quasi-periodic Oscillation (QPOs) of the emitted radiations that are commonly observed from the black hole sources [49–51].

Keeping all these in mind, in the following sections, we describe two fascinating observational phenomena of black hole astrophysics, namely jets/outflows and quasi-periodic oscillations (QPOs). Subsequently, we discuss their connections with the accretion flow properties and the spin of the black hole.

1.3 Jets or outflows

Astrophysical jets are long, collimated, supersonic stream of matters emanating from the compact celestial objects such as young stellar objects (YSOs), white dwarfs (WDs), neutron stars (NSs) and black holes (BHs), respectively. In the course of accretion, a part of the accreting matter emerges out from the disc along the axis of rotation of the black holes in the form of outflows and the outflows are believed to be the precursor of jets. Recently, with the huge development of radio astronomy, bipolar jets are commonly observed in the accreting black hole systems [52–63]. One such radio image of the black hole source Cyg A has been shown in Fig 1.1. It is observed that the jet emissions do not occur universally. Their existence solely depends on the accretion states. It is also observed that the jets are produced in the relativistic and/or ultra relativistic regime. The corresponding Lorentz factors for the jets are usually found to be $\Gamma \lesssim 10$ for AGNs but some rare sources may reach up to $\Gamma \sim 50$ [64]. However, for GBHs sources, the typical Lorentz factor lies in the range $\Gamma \lesssim 2$ [65].

There are mainly three distinct modes of radio emission which are connected to

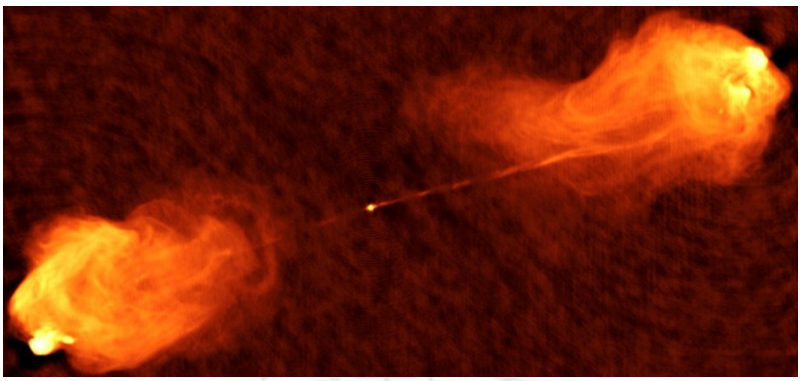

Figure 1.1: Radio image of the extragalactic radio source Cygnus A with lobes, hot spots, jet and core. (Image courtesy of NRAO/AUI [1]).

the accretion states. They are namely the steady jets, transients jets and off states, respectively [63]. In the below, we briefly discuss how the jets and accretion states are closely connected.

1.3.1 Jets and accretion states

In the recent years, several efforts have been made to develop a phenomenological connection between accretion and jet mechanisms in the context of in BH-XRBs. Fender & Belloni (2012) [2, and reference therein] constructed a simplified phenomenological relation between the accretion and jets for various XRBs. These XRBs spend most of the time in the quiescent states and undergo transient outbursting phase lasting for months to years. One such evolution of outburst has been represented by Fender & Belloni (2012) [2] for the source GX 339-4, depicted in Fig 1.2. **Top** panel represents the hardness-intensity diagram (HID) diagram i.e., the hardness of X-ray emission vs X-ray luminosity and **Bottom** panel shows the disc-jet geometrical pictures from soft to hard states. This HID diagram is popularly known as 'Q-diagram'. The outburst evolves in the following stages:

Quiescence to hard state ($A \rightarrow B$): This is the rising phase of the outburst of the source. In that phase, the luminosity increases rapidly and gets brighter in short time scales ($\sim$ days). The corresponding luminosities in the quiescence phase for most of the XRBs are $\sim 10^{30-32}$ erg sec^{-1}. However, some of the sources are stable in the quiescence phase with higher luminosity $\sim 10^{34}$ erg sec^{-1} (e.g. V404 Cyg). In the outbursting phase, the luminosity changes very rapidly and reaches up to $\geq 10^{38}$ erg sec^{-1}. XRBs with this range of luminosities are always in the hard X-ray state and the state is characterized by broad-band X-ray spectrum with photon index $\sim 1.6 - 2.1$ observed within a cutoff energy between $\sim 50 - 100$ keV [66]. Also, in

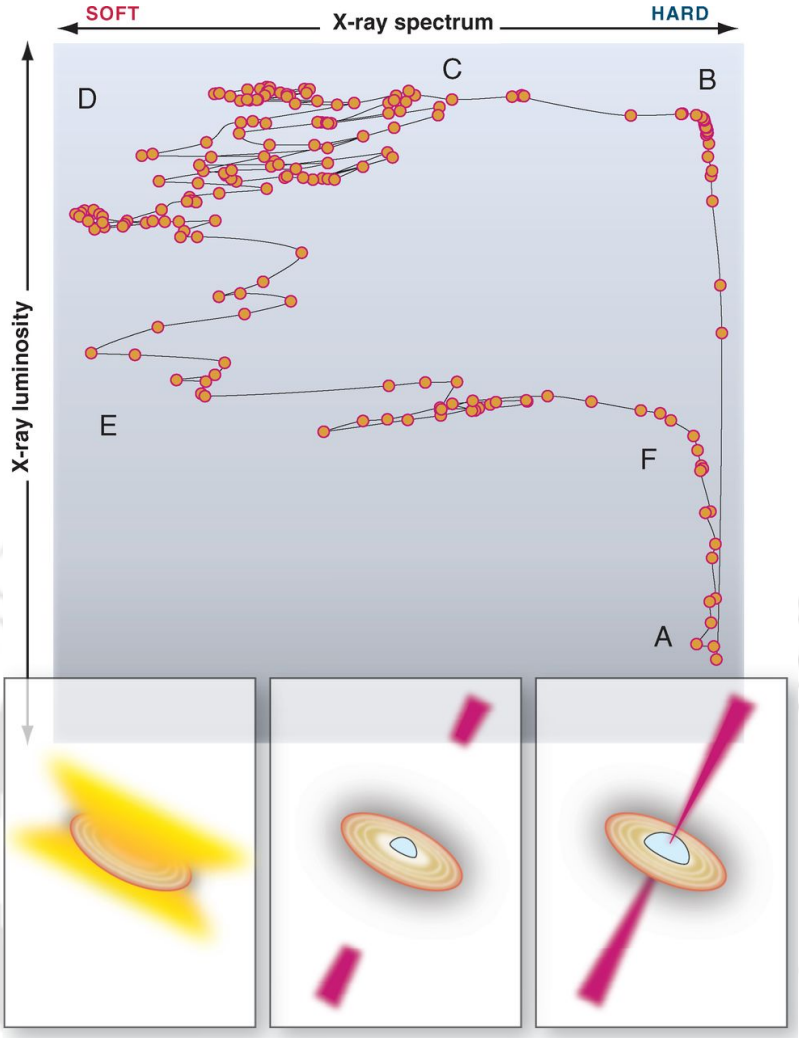

Figure 1.2: Top: Hardness-intensity diagram (HID) for the black hole binary GX 339-4 source. The horizontal and vertical axis represent hardness or color of the X-ray emission and X-ray luminosity from the source, respectively. **Bottom:** Schematic diagram of disc-jet geometrical system from soft to hard states (left to right) [2].

this state, the source exhibits steady radio emission at GHz radio frequencies.

Transition from hard to soft states ($B \rightarrow C \rightarrow D$): In these states, the luminosities lie in the range of 10 to 50% of the Eddington luminosity. The hard X-ray component becomes steep and the blackbody-like component dominates and as a result, the X-ray spectrum becomes soften. It is observed that the spectral transition from hard to soft states can take days to weeks for BH-XRBs and the state transition shows a number of very interesting characteristics. Interestingly, some phases during the transition can be completely dominated by QPOs like features [67]. The radio emission also varies dramatically in this state and shows oscillations. It is observed that the radio flares are more luminous than the previous steady jet in the

hard state. High-resolution radio observations also show that the radio flare moves away from the central black hole in this state transition [53, 54, 68, 69].

The soft state ($D \rightarrow E$): This state exists for a longer period of time, often persisting for a weeks or more. The X-ray spectrum is dominated by a blackbody-like component which peaks around 1 keV. The core radio jet drops dramatically in this soft state [68, 70]. Also, the core-jet is completely switched off and dominates with the strong accretion disc wind.

Return to the quiescence state ($E \rightarrow F \rightarrow A$): In this state, the mass accretion rate of the black hole continues to fall and make a transition from soft to hard state. The luminosity is lower compared to the earlier state transition from hard to soft state. The luminosity is typically around 1% of the Eddington X-ray luminosity and wind completely switches off and jet activity reappears.

1.3.2 Jet power and black hole spin

1.3.2.1 Theoretical investigation

It has been a long quest about the exact mechanism of powering the jets. It started from the theoretical proposition by Penrose (1969) [71]. According to Penrose, a particle falling into the rotating black hole decays into two parts in the ergosphere, one particle carrying positive energy, and another particle carrying negative energy. Since the total energy has to be conserved, if the negative energy particle crosses the event horizon and the positive energy particle leaves the ergosphere reaching the observer, its energy is higher than the energy of the initial particle. For example, a particle falls into ergosphere with energy E_1 and it decays into two fragments with energy E_2 and E_3. Let us consider $E_2 < 0$ and if it allows to fall into the black hole, other fragment of energy E_3 comes out with enhanced energy $E_3 = E_1 - E_2 > E_1$, since $E_2 < 0$. Later Blandford & Znajek (1977) [72] (BZ) investigated that the magnetic field has the potential to power the jets by extracting the electromagnetic energy around rotating black holes. In BZ process, the large-scale poloidal magnetic field passes through the ergosphere of the rotating black hole and also threads the event horizon. Due to the frame dragging effect, it creates a toroidal magnetic field and a Poynting flux. The negative energy flux enters into the horizon and reduces mass-energy and momentum of the black hole. The corresponding outgoing positive energy flux contributes to the jets that carry the positive energy and angular

momentum. According to BZ model, the outflowing jet power is given by [73] ,

$$P_{\rm jet}^{\rm BZ} = \frac{\kappa}{4\pi c}\Psi^2\Omega_{\rm H}^2, \tag{1.10}$$

where Ψ and $\Omega_{\rm H}$ $(= a_k c/2r_{\rm H})$ are the magnetic field threading the horizon and the angular velocity of the horizon, respectively. Here, a_k is the spin of the black hole. The numerical coefficient κ weakly depends on the magnetic geometry and its value is ~ 0.05. It clearly indicates that the jet power solely depends on the ordered magnetic field and the spin of the black hole. Various numerical simulation results are also in agreement of the BZ jet power relation [74–83]. Further, the rearranged BZ jet power can be written by adjusting the coefficient as [84]

$$P_{\rm jet}^{\rm BZ} \approx 2.5\left(\frac{a_k}{1+\sqrt{1-a_k^2}}\right)^2\left(\frac{\Psi}{\Psi_{\rm MAD}}\right)^2 \dot{M}_{\rm BH}c^2, \tag{1.11}$$

where $\Psi_{\rm MAD}$, Ψ and $\dot{M}_{\rm BH}$ are the limiting magnetic flux, actual flux threading the event horizon and mass accretion rate, respectively.

1.3.2.2 Observational investigation

In this section, we investigate the jet kinetic power associated with different types of radio emission.

Steady jets

Various observations reported that in the low-hard state, the radio emission is empirically related to the X-ray luminosity as $L_{\rm R} \propto L_{\rm X}^b$, where $0.6< b <0.7$ for the best sample sources, particularly for GX 339-4 [4], known as 'universal' track. In this regard, Körding et al. (2006) [85] introduced a relation between jet power and radio luminosity for XRBs as well as for some low Eddington AGNs as

$$L_{\rm jet} \sim 4\times10^{36}\left(\frac{L_{8.6}}{10^{30}}\right)^{12/17} \ {\rm erg\ sec^{-1}}, \tag{1.12}$$

where $L_{8.6}$ $(= 4\pi D^2\nu_{8.6}S_{8.6})$ is the radio luminosity measured at frequency $\nu_{8.6} = 8.6$ GHz, D is the distance of the source and $S_{8.6}$ is the measured flux. Similarly, Merloni & Heinz (2013) [86] presented almost identical relation between radio luminosity and

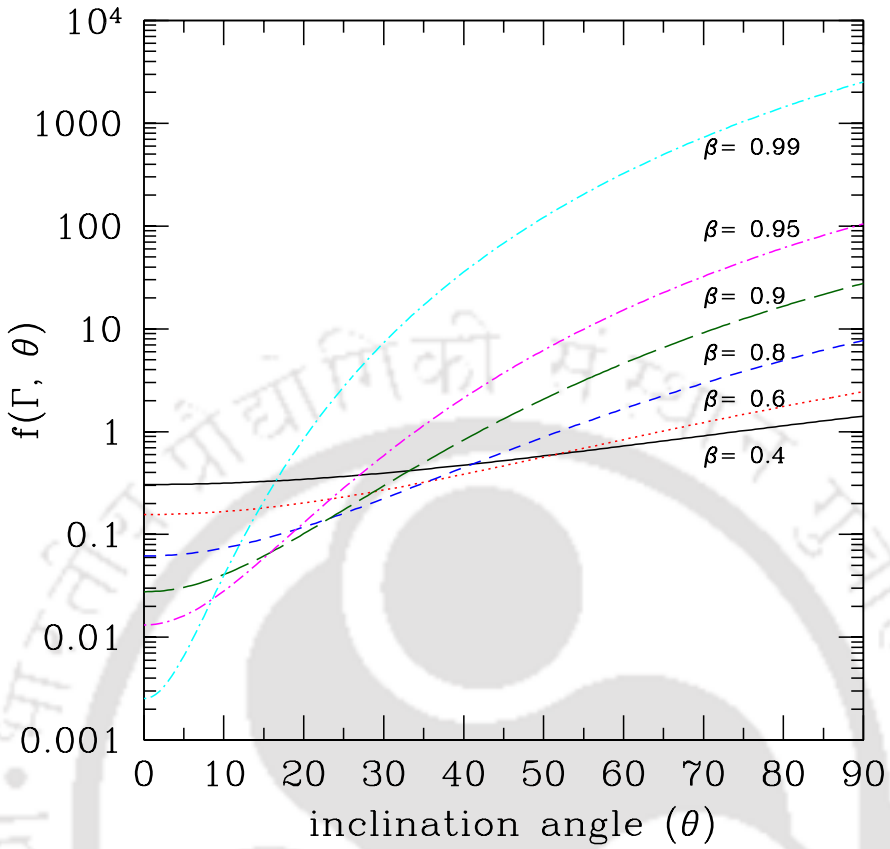

Figure 1.3: Correction factor $f(\Gamma, \theta)$ due to Doppler boosting for estimating kinetic jet power as a function of inclination angle θ for different intrinsic bulk velocities ($\beta = v/c$).

jet power as

$$L_{\rm jet} \sim 1.6 \times 10^{36} \left(\frac{L_{\rm R}}{10^{30}}\right)^{0.81} \ {\rm erg\ sec^{-1}}. \tag{1.13}$$

This is a remarkable relation between core radio luminosity and jet power in the mass range from XRBs to AGNs.

However, in recent years, it is observed that a growing number of sources e.g., H1743-322, Swift 1753.3-0127, XTE J1650-500, XTE J1752-233 [87–92] deviate from the 'universal' track and follow a steeper correlation as $b \sim 1.4$, known as 'outliers' sources [88].

Transient jets

The power associated with the transient jet is calculated by considering the synchrotron luminosity within a given volume. Following the prescription of Longair

(1994) [93], one can estimate the minimum energy associated with the synchrotron emitting plasma within the given volume. So, for a source with luminosity L_ν at frequency ν in a volume V, the minimum energy can be obtained as,

$$E_{\rm min} \approx 8 \times 10^6 \eta_{\rm jet}^{4/7} \left(\frac{V}{\rm cm^3}\right)^{3/7} \left(\frac{\nu}{\rm Hz}\right)^{2/7} \left(\frac{L_\nu}{\rm erg\ sec^{-1} Hz^{-1}}\right)^{4/7} {\rm erg}, \tag{1.14}$$

where $\eta_{\rm jet}$ and V are the jet efficiency factor and volume of the source, respectively. The value of jet efficiency factor is close to unity [94]. If Δt is the rise time of the event, then the volume of the source is $V = (4/3)\pi(c\Delta t)^3$, where c being the speed of light. Now using $L_\nu = 4\pi D^2 S_\nu$, we rewrite the Eq. 1.14 as,

$$E_{\rm min} \approx 3 \times 10^{33} \left(\frac{\Delta t}{\rm sec}\right)^{9/7} \left(\frac{\nu}{\rm GHz}\right)^{2/7} \left(\frac{S_\nu}{\rm mJy}\right)^{4/7} \left(\frac{D}{\rm kpc}\right)^{8/7} {\rm erg}, \tag{1.15}$$

where S_ν is the radio flux in unit of mJy. So, the kinetic power of jet is obtained as,

$$L_{\rm jet}^{\rm kin} = \frac{E_{\rm min}}{\Delta t} \approx 3 \times 10^{33} \left(\frac{\Delta t}{\rm sec}\right)^{2/7} \left(\frac{\nu}{\rm GHz}\right)^{2/7} \left(\frac{S_\nu}{\rm mJy}\right)^{4/7} \left(\frac{D}{\rm kpc}\right)^{8/7} {\rm erg\ sec^{-1}}. \tag{1.16}$$

If the jets are moving with velocity (v) comparably to the speed of light (c), the emitted radiations coming from the jet are expected to be relativistically Doppler boosted towards (or away from) the observer. Thus, we need to include the correction factor due to Doppler effect in the estimated observed kinetic jet power as [94],

$$L_{\rm jet}^{\rm obs} = L_{\rm jet}^{\rm kin} \times f(\Gamma, \theta), \tag{1.17}$$

where $f(\Gamma, \theta)$ $(= \Gamma\delta^{-3})$ is the correction factor due to Doppler effect. The Doppler factor due to the radiation emitted by a source moving at an angle θ to the line of sight is $\delta = 1/[\Gamma(1 - \beta\cos\theta)]$. Here, Γ $[= (1 - \beta^2)^{-1/2}]$ is the bulk Lorentz factor and $\beta = v/c$. The correction factor due to Doppler effect in terms of inclination angle for various bulk velocities is shown in Fig 1.3. The corresponding average value of correction factors are calculated as $f(\Gamma, \theta) = 7$, 36, 114 and 423 for bulk Lorentz factors lie in the range $2 \leq \Gamma \leq 3$, $2 \leq \Gamma \leq 5$, $2 \leq \Gamma \leq 7$ and $2 \leq \Gamma \leq 10$, respectively. Thus, upon neglecting Doppler correction, the observed jet power would be overestimated for lower Lorentz factor ($\Gamma \leq 2$, see Fig. 1.3) and underestimated for higher Lorentz factor ($\Gamma \geq 2$, see 1.3). Therefore, it is necessary

to consider the Doppler correction while estimating the kinetic jet power of the source.

Over the last decade or so, the measurement of black hole spin using continuum fitting (CF) method provides consistent results for various black hole sources through multiple observations [95–99]. In particular, five transient black holes sources, namely A0620-00, XTE J1550-564, GRO J1655-40, GRS 1915+105 and 4U 1543-47 are considered which are known to produce ballistic jets. For these sources, Narayan & Mcclintock (2012) [100] reported that the jet power is proportional to the peak 5 GHz radio flux density and scaled by the mass ($M_{\rm BH}$) of the black hole. Therefore, the proxy for the jet power in natural units is obtained as,

$$P_{\rm jet} = \left(\frac{\nu}{5\ {\rm GHz}}\right)\left(\frac{S_\nu^{\rm tot}}{\rm Jy}\right)\left(\frac{D}{\rm kpc}\right)^2\left(\frac{M_{\rm BH}}{M_\odot}\right)^{-1}, \tag{1.18}$$

where $S_\nu^{\rm tot}$ is the maximum flux density with beaming correction for approaching and receding jets. Steiner et al. (2013) [101] and McClintock et al. (2014) [102] compared the proxy jet power using the above empirical relation (Eq. 1.18) to the theoretically predicted scaled jet power and spin i.e., $P_{\rm jet} \propto a_k^2$ [72] (see Eq. 1.10). They showed that jet power and black hole spin are well correlated for these five black hole sources. On the contrary, Russell et al. (2013) [103] and Fender & Gallo (2014) [66] reported the absence of any of such correlation between the transient jet and black hole spin. They pointed out that the use of peak flux in calculating the proxy power in lieu of total power is not justified. Overall, no general consensus on the correlation between the jet power and spin of the black hole is achieved.

1.4 Quasi-periodic oscillations (QPOs)

The high energy emission from black holes is generally powered by the accretion process around it. In case of XRBs, the variability of X-ray light curve in different time scales ranging from milliseconds to days are frequently observed. Interestingly, such X-ray variabilities are often visualized as QPOs in the power density spectrum (PDS). QPOs were first observed several decades ago in the X-ray flux emitted from accreting neutron stars [104, and references therein]. It is noteworthy that the QPO signatures are the common characteristics in the accreting black holes (BHs) [105], neutron stars (NSs) [106–108], cataclysmic variables (CVs) [109, 110], ultra-luminous X-ray sources [111, 112] and even in active galactic nuclei (AGNs) [113, 114]. In general, the frequency of the QPOs ($\nu_{\rm QPO}$) lies in the range $0.1 - 450$

Hz for galactic black hole sources [105] and the QPOs are broadly classified into two categories in terms of their frequency range as (a) low-frequency QPOs (LFQPOs), $0.1 \leq \nu_{\rm QPO} \leq 40$ Hz and (b) high-frequency QPOs (HFQPOs), $\nu_{\rm QPO} > 40$ Hz [105, 115].

1.4.1 Low frequency QPOs (LFQPOs)

LFQPOs are commonly observed in almost all transients black hole sources and they are classified into three categories, namely type-A, B, and C based on their intrinsic properties. Type-A QPOs are identified by a weak and broad peak where $\nu/\Delta\nu \leq 3$, ν being the frequency of QPOs and its peak lies around 6 - 8 Hz. Usually, the amplitude of the oscillation becomes very small for A-type QPOs and the harmonics do not appear. Moreover, it is observed in the High/Soft State (HSS), just after the transition from the Hard Intermediate State (HIMS) to Soft state [115]. Type-B QPOs are characterized by a relatively strong and narrow peak i.e., $\nu/\Delta\nu \leq 6$ compared to type-A. Its narrow range of centroid frequency is found to be around 6 Hz. Sometimes a weak second harmonic, together with a subharmonic peak is observed. Type-B QPOs are observed in Soft-Intermediate State (SIMS). Finally, type-C QPOs are identified by a strong and narrow peak i.e., $\nu/\Delta\nu \leq 10$. Its centroid frequency varies in few days and the peak lies in the range $0.1 - 15$ Hz. These QPOs are usually observed at the bright end of low-hard state (LHS) and during the HIMS. Sometimes, it can be found in the HSS state with frequency ~ 30 Hz. Presence of harmonics are quite common for C-type QPOs.

By now, several models have been proposed to explain the LFQPOs. One of such model is the relativistic precision model (RPM) based on the Lense-Thirring effect [116–118]. When a test particle moves around a black hole, the orbital plane of the particle will not coalign with the equatorial plane of the black hole due to the relativistic frame-dragging effects. This leads to the relativistic precession of the particle orbits having frequencies compatible with the observed QPO frequencies. This model provides a good explanation of the type-C QPOs. Tagger & Pellat (1999) [119] proposed another model based on accretion-ejection instability (AEI) at the inner part of the disc. They considered that the inner part of the disc is threaded by the moderately strong poloidal magnetic fields. A spiral density wave is produced in the disc due to the magnetic stresses and the disc becomes unstable by exchanging the angular momentum with a Rossby vortex. This instability generates low azimuthal wave numbers which are believed to generate LFQPOs [120, 121].

Meanwhile, Chakrabarti & Titarchuk (1995) [35] proposed that a low angular momentum disc can be produced by mixing both Keplerian and sub-Keplerian components and such a disc may harbor shock wave as a result of the centrifugal barrier. Due to shock transition, PSC becomes hot and it is capable of producing the high energy radiations. Molteni et al. (1996) [122] showed that when the cooling time scale roughly matches the infall timescale of accretion flow, shock starts to oscillate and exhibits QPOs [123–125]. Few other models also present in the literature to explain LFQPOs which are namely the radial and orbital oscillation model [126], global disc oscillation model [127] and drift blob model [128, 129] etc.

1.4.2 High frequency QPOs (HFQPOs)

Among all the fascinating discoveries by *Rossi X-ray Timing Explorer (RXTE)*, the most important one is the detection of HFQPOs. The frequency of HFQPOs lies in the range ≥ 40 Hz [105]. Morgan et al. (1997) [130] first observed the HFQPOs of frequency ~ 67 Hz for the source GRS 1915+105. Since then, a remarkably high number of HFQPOs have been observed in galactic black hole transients [131]. They are observed in single or double peaks [132]. The origin of HFQPOs is of great interest as these oscillations are transient and subtle. Also, it is believed that the HFQPOs are the manifestations of various general relativistic effects in the orbits close to the black hole. Therefore, a general consensus is that it can be used to probe the concepts of general relativity in the strong gravitational field limit.

Several efforts have been made to explain the HFQPOs of black hole sources and most of them involve some form of the predictions of General Theory of relativity (GTR). The relativistic precision model (RPM) which was originally proposed by Stella & Vietri (1998) [116] for explaining LFQPOs, can be used for HFQPOs for black holes as well [117, 118, 133]. In this model, the nodal precession frequency (or Lense-Thirring frequency) corresponds to Type-C QPOs LFQPOs, while the periastron precession frequency and the orbital frequency are associated with the HFQPOs. Subsequently, the nonlinear resonance model has been introduced to understand HFQPO by Abramowicz & Kluzniak (2001) [134] and Kluzniak & Abramowicz (2001) [135]. Later, more studies have been carried out extensively based on nonlinear resonance model to explain HFQPOs [136]. However, it is noteworthy to mention that the exact origin of HFQPOs is still remain elusive.

1.5 Fluid Dynamics of Accretion Flow

In order to understand the basic underline physics involved in jets and QPOs signatures, it is necessary to investigate the fluid dynamics around black holes. Towards this, in the present section, we briefly discuss the various conservation laws in fluid dynamics. These conservation laws explicitly describe the nature of the flow dynamics when the equation of state of the fluid is known. Of course, the flow characteristics must depend on the initial boundary conditions of the system under consideration.

1.5.1 Basic equations

The fluid dynamics is related to the study the motion of gasses or liquids. If the spatial length is much greater than the mean free path of the fluids, the fluids are regarded as the continuous medium. We describe the fluid at a particular moment by its velocity $\boldsymbol{v}(x, y, z, t)$, pressure $p(x, y, z, t)$, density $\rho(x, y, z, t)$ and temperature $T(x, y, z, t)$ at each point. The total amount of mass in an elementary volume is $\int \rho dV$ and the mass flow in unit time through the elementary surface bounded by that elementary volume is $\rho \boldsymbol{v}.d\boldsymbol{s}$. Also, the total mass flowing out from the volume is $\oint \rho \boldsymbol{v}.d\boldsymbol{s}$. So, the continuity equation can be written by equating the total outflowing fluid to the loss of fluid from the volume as,

$$\frac{d}{dt}\int \rho dV = -\oint \rho \boldsymbol{v}.d\boldsymbol{s}. \tag{1.19}$$

Applying Green's theorem, we can transform surface integral to volume integral i.e., $\oint \rho \boldsymbol{v}.d\boldsymbol{s} = \int \boldsymbol{\nabla}.(\rho \boldsymbol{v}) dV$. So, from Eq. 1.19, we obtain

$$\int \left[\frac{\partial \rho}{\partial t} + \boldsymbol{\nabla}.(\rho \boldsymbol{v})\right] dV = 0. \tag{1.20}$$

As this equation holds for any volume, the integral must vanish. With this, hence we obtain the continuity equation which is given by [5, 40],

$$\frac{\partial \rho}{\partial t} + \boldsymbol{\nabla}.(\rho \boldsymbol{v}) = 0, \tag{1.21}$$

where $\rho \boldsymbol{v}$ denotes the mass flux.

The total force acting on the volume is $-\oint p d\boldsymbol{s}$. Changing it in to a volume

integral, we get $-\oint pd\boldsymbol{s} = -\int \boldsymbol{\nabla} p dV$. Also, we equate the force to the pressure as $\rho d\boldsymbol{v}/dt = -\boldsymbol{\nabla} p$. Now, using the relation $d\boldsymbol{v} = \frac{\partial \rho}{\partial t}dt + dx\frac{\partial v}{\partial x} + dy\frac{\partial v}{\partial y} + dz\frac{\partial v}{\partial z} = \frac{\partial \rho}{\partial t}dt + (d\boldsymbol{r}.\boldsymbol{\nabla})\boldsymbol{v}$ and dividing by dt we get,

$$\frac{d\boldsymbol{v}}{dt} = \frac{\partial v}{\partial t} + (\boldsymbol{v}.\boldsymbol{\nabla})\boldsymbol{v}, \tag{1.22}$$

and

$$\frac{\partial v}{\partial t} + (\boldsymbol{v}.\boldsymbol{\nabla})\boldsymbol{v} = -\frac{1}{\rho}\boldsymbol{\nabla} p. \tag{1.23}$$

Therefore, the momentum conservation of gas elements can be obtained from the Euler's equation as,

$$\frac{\partial v}{\partial t} + (\boldsymbol{v}.\boldsymbol{\nabla})\boldsymbol{v} = -\frac{1}{\rho}\boldsymbol{\nabla} p + f_{\text{ext}}, \tag{1.24}$$

where f_{ext} refers the external forces like gravity, viscosity, body forces etc.

The energy contains in a fixed volume element is $(\frac{1}{2}\rho v^2 + \rho\varepsilon)$, where $\frac{1}{2}\rho v^2$ and $\rho\varepsilon$ are the measure of kinetic energy density and internal energy density, respectively. So, the rate of change of energy is given by,

$$\frac{\partial}{\partial t}\left(\frac{1}{2}\rho v^2 + \rho\varepsilon\right) = \frac{1}{2}\frac{\partial}{\partial t}(\rho v^2) + \frac{\partial}{\partial t}(\rho\varepsilon). \tag{1.25}$$

The first term in the right hand side is simplified using continuity Eq. 1.21 and Eq. 1.22 as,

$$\frac{\partial}{\partial t}\left(\frac{1}{2}\rho v^2\right) = \frac{1}{2}v^2\frac{\partial \rho}{\partial t} + \rho\boldsymbol{v}.\frac{\partial \boldsymbol{v}}{\partial t} = -\frac{1}{2}v^2(\boldsymbol{\nabla}.\rho\boldsymbol{v}) - \boldsymbol{v}.\boldsymbol{\nabla} p - \rho\boldsymbol{v}.(\boldsymbol{v}.\boldsymbol{\nabla})\boldsymbol{v}. \tag{1.26}$$

Now, from the thermodynamic relation, we know $d\varepsilon = Tds - pdV = Tds + (p/\rho^2)d\rho$. Since, the heat function can be written as $w = \rho\varepsilon + p = \rho\varepsilon + pV$, we obtain

$$d(\rho\varepsilon) = \varepsilon d\rho + \rho d\varepsilon = \rho T ds + w d\rho. \tag{1.27}$$

Again, using Eq. 1.21 and adiabatic equation of motion for entropy, namely $\frac{\partial s}{\partial t} + \boldsymbol{v}.\boldsymbol{\nabla} s = 0$, as $\frac{ds}{dt} = 0$, we get,

$$\frac{\partial(\rho\varepsilon)}{\partial t} = w\frac{\partial \rho}{\partial t} + \rho T\frac{\partial s}{\partial t} = -w\boldsymbol{\nabla}.(\rho\boldsymbol{v}) - \rho T\boldsymbol{v}.\boldsymbol{\nabla} s. \tag{1.28}$$

Hence, the rate of change of energy is obtained from Eq. 1.26 using Eq. 1.27 and Eq. 1.28 as,

$$\begin{aligned}\frac{\partial}{\partial t}\left(\frac{1}{2}\rho v^2+\rho\varepsilon\right) &= -\left(\frac{1}{2}v^2+w\right)\boldsymbol{\nabla}.(\rho\boldsymbol{v})-\rho\boldsymbol{v}.\boldsymbol{\nabla}\left(\frac{1}{2}v^2+w\right)\\ &= -\boldsymbol{\nabla}.\left[\rho\left(\frac{1}{2}v^2+w\right)\boldsymbol{v}\right]. \end{aligned} \tag{1.29}$$

Finally, the energy equation in presence of external energy sources is calculated as [5],

$$\frac{\partial}{\partial t}\left(\frac{1}{2}\rho v^2+\rho\varepsilon\right)+\boldsymbol{\nabla}.\left[\left(\frac{1}{2}\rho v^2+\rho\varepsilon+p\right)\boldsymbol{v}\right]=\boldsymbol{f}_{\text{ext}}.\boldsymbol{v}-\boldsymbol{\nabla}.\boldsymbol{F}_{\text{rad}}-\boldsymbol{\nabla}.\boldsymbol{q}, \tag{1.30}$$

where the term $-\boldsymbol{\nabla}.\boldsymbol{F}_{\text{rad}}$ represents the rate of loss of energy due to radiation and $\boldsymbol{F}_{\text{rad}}$ is the radiative flux vector. Also, $-\boldsymbol{\nabla}.\boldsymbol{q}$ is the rate of loss of conductive heat due to the random motion and $\boldsymbol{q}$ denotes the conductive heat flux. In general, most of the cases in fluid dynamics, the temperature gradients are small enough that we can ignore conductive flux term from energy equation.

From Eq. 1.30, it is clear that the identification of the appropriate external forces (f_{ext}) is the utmost important task to solve fluid dynamics correctly. In the case of black hole accretion, we need to consider appropriate gravitational forces to obtain correct results. Therefore, in the following section, we discuss the different forms of gravitational potentials (pseudo potentials) that satisfactorily describes the space-time geometry around black holes.

1.6 Gravitational potentials around black holes

Astrophysical black holes are described only by two parameters: mass and spin. Newton's theory of gravitation is inadequate to describe the massive compact objects like black holes. Thus, we need Einstein's general theory of relativity (GTR) for proper descriptions of black holes. In this context, the Schwarzschild solution describes the spherical black holes with no charge or angular momentum. On the other hand, the Kerr solution describes rotating but uncharged black holes. Here we briefly discuss these two black hole solutions.

1.6.1 Schwarzschild Solution

In this section, we explore Schwarzschild metric which properly describes the external field of a non-rotating black hole. In fact, Schwarzschild (1916) [137] first introduced one of the simplest solutions to describe the gravitational field exterior to a static, spherical, uncharged mass without angular momentum. Here, we use the unit system as $G = M_{\rm BH} = c = 1$. In spherical polar coordinate system (r, θ, ϕ), the Schwarzschild metric can be written as,

$$ds^2 = -\left(1 - \frac{2}{r}\right) dt^2 - \left(1 - \frac{2}{r}\right)^{-1} dr^2 + r^2 d\theta^2 + r^2 \sin^2\theta d\phi^2, \tag{1.31}$$

where Schwarzschild radius is defined as $r_g = \frac{2GM_{\rm BH}}{c^2}$. When a test particle moves freely in Schwarzschild geometry, the Lagrangian can be obtained from the metric coefficient using $L = \frac{1}{2} g_{\mu\nu} u^\mu u^\nu$ as [138, 139]

$$2L = -\left(1 - \frac{2}{r}\right) \dot{t}^2 - \left(1 - \frac{2}{r}\right)^{-1} \dot{r}^2 + r^2 \dot{\theta}^2 + r^2 \sin^2\theta \dot{\phi}^2. \tag{1.32}$$

So, the Euler-Lagrange's equations are

$$\frac{d}{d\xi}\left(\frac{\partial L}{\partial \dot{x}^i}\right) - \frac{\partial L}{\partial x^i} = 0; \qquad x^i \equiv (t, r, \theta, \phi), \tag{1.33}$$

where ξ is any parameter along worldline. Now, the equation of motions for t, θ and ϕ are given by,

t equation:

$$\frac{d}{d\xi}\left[-2\left(1 - \frac{2}{r}\right)\dot{t}\right] = 0$$

$$\text{or,} \quad \left(1 - \frac{2}{r}\right)\frac{dt}{d\tau} = \text{constant} = E. \tag{1.34}$$

θ equation:

$$\frac{d}{d\xi}\left[2\left(r\dot{\theta}\right)\right] - 2r^2 \sin\theta\cos\theta\dot{\phi}^2 = 0$$

$$\text{or,} \quad \frac{d}{d\xi}\left(r\frac{d\theta}{d\tau}\right) = r^2 \sin\theta\cos\theta\dot{\phi}^2. \tag{1.35}$$

ϕ equation:

$$\frac{d}{d\xi}\left[2r^2\sin^2\theta\dot{\phi}\right] = 0$$
$$\text{or,} \quad r^2\sin^2\theta\frac{d\phi}{d\tau} = \text{constant} = l. \tag{1.36}$$

Let us consider that the particle is moving on the equatorial plane i.e., $\theta = \frac{\pi}{2}$ and $\dot{\theta} = 0$. Using the velocity constraint equation $g_{\mu\nu}u^\mu u^\nu = -1$, we get from Eq. 1.32 using Eq. 1.34, Eq. 1.35 and Eq. 1.36

$$\left(\frac{dr}{d\tau}\right)^2 - E^2 + \frac{l^2}{r^2}\left(1-\frac{2}{r}\right) = -\left(1-\frac{2}{r}\right),$$
$$\text{or,} \quad \left(\frac{dr}{d\tau}\right)^2 = E^2 - V_{\rm S}^2, \tag{1.37}$$

where $V_{\rm S}$ is the effective potential around Schwarzschild black holes and is given by,

$$V_{\rm S} = \left[\left(1-\frac{2}{r}\right)\left(\frac{l^2}{r^2}+1\right)\right]^{1/2}. \tag{1.38}$$

The conserved angular momentum $l = u_\phi$ represents for the particle dynamics. But, angular momentum $\lambda = -\frac{u_\phi}{u_t}$ is conserved for fluid dynamics as well as for the particle dynamics. Also, the Keplerian angular momentum can be obtained from the locus of the extrema of $V_{\rm S}(r)$ from Eq. 1.38. Therefore,

$$l_{\rm kep}^2 = \left(-\frac{u_\phi}{u_t}\right)^2 = \frac{r^3}{(r-2)^2}. \tag{1.39}$$

On the other hand, the gravitational potential of a test particle around a Newtonian star is $\Phi_{\rm N} = -\frac{1}{r}$. So, the effective potential around Newtonian star is obtained by summation of the gravitational potential and the centrifugal potential as

$$V_{\rm N} = 1 + \Phi_{\rm N} + \frac{1}{2}\frac{l^2}{r^2}, \tag{1.40}$$

where "1" represents the rest mass energy to compare with GR results. For small r, the effective Newtonian potential diverges to positive infinity at the origin $r = 0$. This implies that infalling matters or particles will bounce back from the Newtonian star surface. For accretion to occur in a finite size r, the centrifugal force must be weaker compared to the gravitational force i.e., $\frac{dV_{\rm N}(r)}{dr} = \frac{l^2}{r^3} - \frac{1}{r^2} < 0$ or $l < r^{1/2}$. In other words, the matter with angular momentum less than the Keplerian angular

momentum can accrete on to the surface of the Newtonian star. But, in the case of black hole accretion, the situation is quite different. For small r, $V_{\rm S}(r)$ dives down with decreasing r and $V_{\rm S}(r) = 0$ at $r = r_g = \frac{2GM_{\rm BH}}{c^2}$. Also, the circular orbits are defined as (a) $\frac{dV_{\rm S}(r)}{dr} = 0$ and (b) $\frac{dr}{d\tau} = 0$. Using condition (a) in Eq. 1.38, we get,

$$r^2 - l^2 r + 3l^2 = 0. \tag{1.41}$$

Here, the roots are real for $l \geq 2\sqrt{3}$ and $V_{\rm S}(r)$ has an extremum value at $l \geq 2\sqrt{3}$. Moreover, the circular orbit is known as the position of the marginally stable orbit or the innermost stable circular orbit (ISCO) for $l \geq 2\sqrt{3}$. Putting $l = 2\sqrt{3}$ in Eq. 1.41, we get $r_{\rm ISCO} = 6$. Now, imposing condition (b) in Eq. 1.38 and using Eq. 1.37, we get,

$$E^2 = \frac{(r-2)^2}{r(r-3)} \quad \text{and} \quad l^2 = \frac{r^2}{(r-3)}. \tag{1.42}$$

Putting $r_{\rm ISCO} = 6$ and $l = 2\sqrt{3}$ in Eq. 1.38, we get $V_{\rm S}(r_{\rm ISCO}) = \sqrt{\frac{8}{9}}$. Therefore, the binding energy per unit mass at $r_{\rm ISCO}$ is obtained as,

$$\eta = 1 - V_{\rm S}(r_{\rm ISCO}) = 1 - \sqrt{\frac{8}{9}} = 5.72\%. \tag{1.43}$$

Here, η denotes the efficiency factor which implies that this fractional amount of rest-mass energy is released when a particle falls towards black hole from infinity to the ISCO.

1.6.2 Kerr Solution

Kerr (1963) [140] first derived the solution for the spinning black holes from Einstein's equations and these solutions are more realizable in the Boyer & Lindquist (1967) [141] coordinates given by,

$$\begin{aligned} ds^2 = &-\left(1 - \frac{2r}{\Sigma}\right) dt^2 - \frac{4a_k r \sin^2\theta}{\Sigma} dt d\phi + \frac{\Sigma}{\Delta} dr^2 + \Sigma d\theta^2 \\ &+ \left(r^2 + a_k^2 + \frac{2r a_k^2 \sin^2\theta}{\Sigma}\right) \sin^2\theta d\phi^2. \end{aligned} \tag{1.44}$$

Here, a_k $(= \frac{J}{M_{\rm BH}})$ is the spin of the black hole and J is the total orbital angular momentum. The black hole is rotating in the $\phi-$direction and also, $\Delta = r^2 - 2r + a_k^2$ and $\Sigma = r^2 + a_k^2 \cos^2\theta$. It is evident that Kerr solution reduces to Schwarzschild

solution for $a_k = 0$ (see Eq. 1.31). The event horizon occurs where the metric function Δ vanishes i.e., $r = 1 \pm \sqrt{1 - a_k^2}$ and the larger root is called the event horizon $r_{\rm H} = 1 + \sqrt{1 - a_k^2}$. In the equatorial plane, the Lagrangian can be written as before (see Eq. 1.32)

$$2L = -\left(1 - \frac{2r}{\Sigma}\right)\dot{t}^2 - \frac{4a_k r \sin^2\theta}{\Sigma}\dot{t}\dot{\phi} + \frac{\Sigma}{\Delta}\dot{r}^2 + \left(r^2 + a_k^2 + \frac{2ra_k^2\sin^2\theta}{\Sigma}\right)\sin^2\theta\dot{\phi}^2. \tag{1.45}$$

Similarly, the t and ϕ equations are calculated as,

t equation:

$$\left(1 - \frac{2}{r}\right)\dot{t} + \frac{2a_k}{r}\dot{\phi} = E. \tag{1.46}$$

ϕ equation:

$$-\frac{2a_k}{r}\dot{t} + \left(r^2 + a_k^2 + \frac{2a_k^2}{r}\right)\dot{\phi} = l. \tag{1.47}$$

Solving $\dot{t}$ and $\dot{\phi}$ equation, we get,

$$\dot{t} = \frac{(r^3 + a_k^2 r + 2a_k^2)E - 2a_k l}{r\Delta} \quad \text{and} \quad \dot{\phi} = \frac{(r-2)l + 2a_k E}{r\Delta}. \tag{1.48}$$

Substituting $\dot{t}$ and $\dot{\phi}$ in Eq. 1.45, we obtain

$$r^3\left(\frac{dr}{d\xi}\right)^2 = \Psi(E, l, r), \tag{1.49}$$

where

$$\Psi = E^2(r^3 + a_k^2 r + 2a_k^2) - 4a_k El - (r-2)l^2 - r\Delta. \tag{1.50}$$

Here, Ψ is known as an effective potential for radial motion in the equatorial plane. Also, for circular orbits, $\frac{dr}{d\xi} = 0$ and this requires

$$\Psi = 0 \quad \text{and} \quad \frac{\partial\Psi}{\partial r} = 0. \tag{1.51}$$

Using the conditions of Eq. 1.51 and solving for E and l, we get [142],

$$E = \frac{r^2 - 2r \pm a_k r^{1/2}}{r(r^2 - 3r \pm 2a_k r^{1/2})^{1/2}} \tag{1.52}$$

and

$$l = \pm \frac{r^{1/2}(r^2 \mp 2a_k r^{1/2} + a_k^2)}{r(r^2 - 3r \pm 2a_k r^{1/2})^{1/2}}, \tag{1.53}$$

where upper sign implies corotating and lower sign refers counterrotating orbits. For non rotating black hole ($a_k = 0$), the above constants reduce to Schwarzschild solutions (see Eq. 1.42). Following Bardeen et al. (1972) [142], we obtain the expression for innermost stable circular orbit as,

$$r_{\rm ISCO} = 3 + Z_2 \mp [(3 - Z_1)(3 + Z_1 + 2Z_2)]^{1/2}, \tag{1.54}$$

where, $Z_1 = 1+(1-a_k^2)^{1/3}[(1+a_k)^{1/3}+(1-a_k)^{1/3}]$, and $Z_2 = (3a_k^2+Z_1^2)^{1/2}$. Here, '$\mp$' sign stands for prograde and retrograde flow. For $a_k = 0$, $r_{\rm ISCO} = 6$ (Schwarzschild), for $a_k = 1$, $r_{\rm ISCO} = 1$ (maximally prograde) and for $a_k = -1$, $r_{\rm ISCO} = 9$ (maximally retrograde). Now, the stability of the orbits require $\frac{\partial^2 \Psi}{\partial r^2} \leq 0$. Applying the stability condition in Eq. 1.50, we get,

$$1 - E^2 \geq \frac{2}{3r}. \tag{1.55}$$

Therefore, eliminating r from Eq. 1.52 and using Eq. 1.55, we obtain,

$$a_k = \mp \frac{4\sqrt{2}(1 - E^2)^{1/2} - 2E}{3\sqrt{3}(1 - E^2)}. \tag{1.56}$$

For maximally rotating case ($a_k = 1$), we obtain $E = \frac{1}{\sqrt{3}}$. So, the efficiency factor for maximally prograde flow is given by,

$$\eta = 1 - E(r_{\rm ISCO}) = 1 - \sqrt{\frac{1}{3}} = 42.26\%. \tag{1.57}$$

Therefore, the maximum available energy is 42% for accretion onto an extreme Kerr black hole.

1.6.3 Pseudo potentials for black hole

Because of the compactness, the space-time geometry around black hole differs from the ordinary star and it can be successfully described by the general theory of relativity. However, in most of the astrophysical systems where a neutron star or a black hole is involved, it is possible to avoid the complex and rigorous full general relativistic treatment particularly when the interesting astrophysical processes are not occurring extremely close (within $r \lesssim 2r_g$, r_g being the Schwarzschild radius) to the black hole horizon. In a way, the solutions of the accretion flow can be studied using Newtonian concept (i.e., flat geometry) by adopting the pseudo-Newtonian potential that retains all the salient features of black hole geometry well outside the black hole horizon. There are several attempts to formulate pseudo-Newtonian potentials to mimic black hole space-time geometry around a non-rotating black hole. Among all, Paczyński & Witta (1980) [3] (hereafter PW80) pseudo-potentials is the most efficient and widely used.

1.6.3.1 Pseudo potentials for non-rotating black hole

Paczyński & Witta (1980) [3] first introduced a pseudo-Newtonian potential to describe the behaviour of test particles moving in the vicinity of a black hole and is given as,

$$\Phi_{\rm PW} = \frac{1}{(r-2)}. \tag{1.58}$$

The effective potential can be obtained as,

$$V_{\rm PW} = 1 + \frac{\lambda^2}{2r^2} + \Phi_{\rm PW}. \tag{1.59}$$

The Keplerian angular momentum distribution ($\lambda_{\rm kep}$) is obtained by equating the gravitational and centrifugal force (i.e., $\frac{dV_{\rm PW}}{dr} = 0$) as,

$$\lambda^2_{\rm kep} = \frac{r^3}{(r-2)^2}. \tag{1.60}$$

Eq. 1.60 clearly indicates that pseudo-Newtonian potential exactly reproduces the Keplerian distribution of angular momentum same as Schwarzschild spacetime (see Eq. 1.42). Also, $r_{\rm ISCO} = 6$ is obtained by minimizing the Keplerian angular momentum from Eq. 1.60. Thus, PW80 pseudo-Newtonian potential reproduces the

position of $r_{\rm ISCO}$ exactly same as Schwarzschild spacetime. Further, the efficiency factor for this potential is

$$\eta = 1 - V_{\rm PW}(r_{\rm ISCO}) = 6.25\%, \tag{1.61}$$

which is also in good agreement with the Schwarzschild solution (see Eq. 1.43). It is noteworthy to mention that this potential is very much appreciated by the astrophysical community and a large number of articles have been published, especially dealing with the accretion disc around black holes.

1.6.3.2 Pseudo potentials for rotating black hole

Following the same spirit of PW80, several attempts were made to construct pseudo-Kerr potential for rotating black hole as well. Initially, Chakrabarti & Khanna (1992) [143] proposed a pseudo-Kerr potential which is able to replicate the Kerr-geometry in the equatorial plane with reasonable accuracy. Later, Artemova et al. (1996) [144] (hereafter ABN96) introduced a prescription for free-fall acceleration around Kerr black hole. The derivation of pseudo-Kerr potential from this free-fall acceleration is simple and this potential reproduces the features of Kerr geometry quite well. After that, Mukhopadhyay (2002) [145] (hereafter MU02) formulated another pseudo-Kerr potential which is derived in the realm of Kerr space-time geometry. Later on, Chakrabarti & Mondal (2006) [146] (hereafter CM06) prescribed the modified version of the Chakrabarti & Khanna (1992) [143] potential which satisfactorily mimics the space-time geometry around rotating black hole for black hole spin $a_k \leq 0.8$. There are several other attempts have been made to formulate pseudo-Kerr potential to describe Kerr black hole [147–150]. Here, we briefly describe three widely used pseudo-Kerr potentials, namely ABN96 [144], MU02 [145] and CM06 [146] as follows.

(I) **ABN96** [144]: In order to study the properties of accretion flow around rotating black hole, Artemova et al. (1996) [144] proposed the expression of pseudo-Kerr force which is given by,

$$F_1(r) = \frac{1}{r^{2-\beta}(r - r_{\rm H})^{\beta}}, \tag{1.62}$$

where $r_{\rm H}$ is the position of the event horizon and r denotes the radial coordinate. The exponent β is expressed as $\beta = \frac{r_{\rm ISCO}}{r_{\rm H}} - 1$, where $r_{\rm ISCO}$ is the inner most stable

circular orbit (ISCO) (see Eq. 1.54). In order to obtain the pseudo-Kerr potential $\Phi_1(r)$, we integrate Eq. 1.62 analytically by imposing the condition $\Phi(r) \to 0$ for $r \to \infty$ [151] and is given by,

$$\Phi_1(r) = \begin{cases} \frac{1}{(\beta-1)r_{\rm H}} \left[1 - \left(\frac{r}{r-r_{\rm H}}\right)^{\beta-1}\right], & \text{if } \beta \neq 1 \\ \frac{1}{r_{\rm H}} ln\left(1 - \frac{r_{\rm H}}{r}\right), & \text{if} \beta = 1 \end{cases}$$

for $r > r_{\rm H}$. The above pseudo-Kerr potential reduces exactly to PW80 (see Eq. 1.58) potential for $a_k = 0$ and $\beta = 2$. In general, this pseudo-Kerr potential shows good agreement with the result obtained from Kerr geometry. However, for highly spinning black hole, the accretion solutions deviate from the general relativistic results within the limit of 10% - 20% error. The general form of the effective pseudo potential ($\Phi_1^{\rm eff}$) is given by,

$$\Phi_1^{\rm eff} = \frac{\lambda^2}{2r^2} + \Phi_1(r), \tag{1.63}$$

where the first term in the right hand side denotes the centrifugal potential corresponding to the specific angular momentum of the flow (λ).

(II) **MU02** [145]: Mukhopadhyay (2002) [145] formulated the expression of gravitational force $F(r)$ corresponding to the pseudo potential in the accretion disc around rotating black hole using Eq. 1.52 and Eq. 1.53 and which is given by,

$$F_2(r) = \frac{(r^2 - 2a_k\sqrt{r} + a_k^2)^2}{r^3[\sqrt{r}(r-2) + a_k]^2}. \tag{1.64}$$

The above pseudo-Kerr force successfully reproduces the inner disc properties which are in close agreement with the Kerr geometry for moderately spinning black holes. For the higher spinning black holes, the accretion solution deviates from the general relativistic results although the error remains restricted within the acceptable limit of 10%. The corresponding expression of the pseudo potential ($\Phi(r)$) is obtained as,

$$\Phi_2(r) = \int_\infty^r F_2(r) dr. \tag{1.65}$$

It is also to be noted that $\Phi_2(r)$ reduces to the PW80 potential for $a_k = 0$. Similar to Eq. 1.63, we obtain the effective pseudo-Kerr potential as

$$\Phi_2^{\rm eff} = \frac{\lambda^2}{2r^2} + \Phi_2(r). \tag{1.66}$$

(III) **CM06** [146]: Chakrabarti & Mondal (2006) [146] supplemented an alternative pseudo-Kerr effective potential that satisfactorily captures the general relativistic features around black hole for $a_k < 0.8$. The expression of the effective pseudo-Kerr potential ($\Phi_3^{\rm eff}$) is given by,

$$\Phi_3^{\rm eff} = -\frac{B + \sqrt{B^2 - 4AC}}{2A}, \tag{1.67}$$

where

$$A = \frac{\epsilon^2 \lambda^2}{2x^2},$$

$$B = -1 + \frac{\epsilon^2 \omega \lambda r^2}{x^2} + \frac{2a_k \lambda}{r^2 x},$$

$$C = 1 - \frac{1}{r - x_0} + \frac{2a_k \omega}{x} + \frac{\epsilon^2 \omega^2 r^4}{2x^2}.$$

Here, x and r represent the cylindrical and spherical radial distance. Here, $x_0 = 0.04 + 0.97a_k + 0.085a_k^2$, $\omega = 2a_k/(x^3 + a_k^2 x + 2a_k^2)$ and $\alpha^2 = (x^2 - 2x + a_k^2)/(x^2 + a_k^2 + 2a_k^2/x)$, ϵ is the redshift factor. The above pseudo-Kerr potential is not exactly reduced to PW80 potential form for $a_k = 0$ [152]. The corresponding pseudo-Kerr force is obtained as $F_3(r) \equiv \Phi_r' = \left(\frac{\partial \Phi_3^{\rm eff}}{\partial r}\right)_{z<<x}$, where, z is the vertical height in the cylindrical coordinate system and $r = \sqrt{x^2 + z^2}$.

The above mentioned pseudo-Kerr potentials are quite effective and useful for studying the accretion flow properties around rotating black holes. In this thesis, we shall use these potentials in the subsequent chapters to mimic the general relativistic effects around rotating black holes.

1.7 Shock waves in Accretion Flow

In the present section, we discuss the shock waves in the context of accretion flow around black holes. In reality, shock wave is defined as a layer of rapid change propagating through the fluid. In its rest frame, the shock is approximately invariable in time and is marked by a rapid transition of parameters from the medium ahead (upstream) to the medium behind (downstream) from the shock. The existence of shock waves is frequently encountered in the astrophysical system, in particularly

when the bulk velocity of the inflowing gas makes a discontinuous transition from supersonic to subsonic values. In the fluid medium, disturbances always propagate at a sound speed (a) relative to the speed of fluid (v). The ratio of the speed of fluid to the speed of sound is called Mach no ($M = v/a$). Mach number less than unity ($M < 1$) and greater than unity ($M > 1$) imply subsonic and supersonic flow, respectively. When the flow makes transition from subsonic to supersonic or vice versa either continuously or discontinuously, it is called as transonic flow. The point of continuous transition is known as sonic point and on the other hand, the location of discontinuous transition is called shock.

1.7.1 Shock conditions

For an obstacle in a supersonic flow, the disturbances cannot propagate upstream through the obstacle, i.e., the flow cannot adjust to the presence of the obstacle because there is no way of propagating a signal in that direction. Therefore, the flow changes its properties discontinuously in the form of shock. Usually, shock thickness is considered to be very small and thus, it can be regarded as local plane. Also, the gas passes through the shock so quickly that the changes in the gas conditions cannot affect the details of the shock transition. Therefore, flow continue to remain steady when it cross the shock front. Adopting all these considerations, we present the steady shock conditions following the prescription of Frank et al. (2002) [5] and Clarke & Carswell (2007) [153]. If x is the measure of distance from shock front, we integrate the conservation equations with respect to x from $-dx$ to dx, where $dx \to 0$.

• **Mass conservation across shock**

Considering the x-direction, Eq. 1.21 takes the following form as,

$$\frac{\partial \rho}{\partial t} + \frac{\partial}{\partial x}(\rho v_x) = 0. \tag{1.68}$$

Upon integrating Eq. 1.68 over a layer of thickness dx, we get,

$$\frac{\partial}{\partial t}\int \rho dx + \rho v_x|_{\frac{dx}{2}} - \rho v_x|_{-\frac{dx}{2}} = 0. \tag{1.69}$$

If mass does not accumulate in that layer, for the infinitesimal length dx, the 'mass flux in' is equal to 'mass flux out' as $\frac{\partial}{\partial t}\int \rho dx = 0$. Hence, the mass flux $J = \rho v_x$

remains same across the shock as,

$$\rho v_x|_{\frac{dx}{2}} - \rho v_x|_{-\frac{dx}{2}} = 0. \tag{1.70}$$

This allows us to write the conservation of mass across the shock as,

$$\rho_+ v_+ = \rho_- v_-. \tag{1.71}$$

where '+' and '−' sign implies the quantities after and before shock transition, respectively. This relation is only valid if there is no mass loss from the disc.

• Momentum conservation across shock

Here, we start with the momentum conservation (Eq. 1.24). The x-component of the momentum conservation equation can be written as,

$$\frac{\partial}{\partial t}(\rho v_x) = -\frac{\partial}{\partial x}(\rho v_x^2 + p) - \rho \frac{\partial}{\partial x} f_{\rm ext}. \tag{1.72}$$

Integrating over the small region dx, we get,

$$\frac{\partial}{\partial t}\int (\rho v_x) dx = -(\rho v_x^2 + p)|_{\frac{dx}{2}} + (\rho v_x^2 + p)|_{-\frac{dx}{2}}, \tag{1.73}$$

where the contribution from the gravitational term is ignored as $f_{\rm ext}$ is continuous at the shock. With this, the momentum conservation across the shock is obtained as,

$$\rho_+ v_+^2 + p_+ = \rho_- v_-^2 + p_-. \tag{1.74}$$

This indicates that the sum of the thermal and ram pressures across the shock is a constant quantity.

• Energy conservation across shock

In the similar way, we integrate energy equation (Eq. 1.30) to obtain,

$$\left(\frac{1}{2}v_x^2 + \epsilon + \frac{p}{\rho}\right)|_{\frac{dx}{2}} - \left(\frac{1}{2}v_x^2 + \epsilon + \frac{p}{\rho}\right)|_{-\frac{dx}{2}} = 0, \tag{1.75}$$

where other energy components are assumed continuous across the shock. Using Eq. 1.75, it is straight forward to get energy conservation across the shock and is

given by,

$$\left(\frac{1}{2}v_+^2 + \epsilon_+ + \frac{p_+}{\rho_+}\right) = \left(\frac{1}{2}v_-^2 + \epsilon_- + \frac{p_-}{\rho_-}\right). \tag{1.76}$$

The conservation Eqs. 1.71, 1.74 and 1.76 are collectively known as the Rankine-Hugoniot relations [5, 40, 153]. In this thesis, we shall use the Rankine-Hugoniot shock conditions to identify the shock locations.

1.8 Overview of the thesis

In this thesis, we extensively investigate advective accretion flow properties and associated mass loss from the disc around rotating black holes. By numerical simulation, Molteni et al. (1996) [154] first showed that a part of the inflowing matter emerges out from the disc between the two well-defined surfaces, namely centrifugal barrier (CB) and funnel wall (FW). The centrifugal barrier (CB) and funnel wall (FW) are defined as the pressure maximum and pressure minimum surfaces, respectively. In the thesis work, we assume that the accretion disc lies along the equatorial plane and jet geometry is considered in the off-equatorial plane along the axis of rotation of the black hole. We also adopt pseudo-Kerr potentials to mimic the general relativistic space-time around rotating black holes. The inflowing matter experiences a virtual barrier due to the repulsive centrifugal force near to the black hole against gravity force. Such virtual barrier triggers the discontinuous transition of the flow variables in the form of shock waves. Solution involving shock waves is thermodynamically preferred as it contains higher entropy content. Due to shock compression, the post-shock flow becomes very hot and dense which behaves like a post-shock-corona (PSC). Eventually, PSC acts as the effective boundary layer of the black holes. During accretion, a part of the inflowing matter is deflected by PSC and driven out in the vertical direction by the excess thermal gradient force across the shock as bipolar outflows. For finding shock solutions, we apply the Rankine-Hugoniot (RH) shock conditions [5, 40, 153]. With this, we self-consistently calculate mass outflow rates and apply our accretion-ejection model to estimate the kinetic jet power for various black hole sources. In the following, we briefly describe the plan of the thesis. There are a total of six chapters. In the following, we proceed with a brief description of each Chapter.

• In **Chapter 1**, we present the various accretion disc models around black holes and discuss the utilities and limitations of these models. We also discuss the con-

servation laws of fluid dynamics which are used in the subsequent chapter to study the accretion flow dynamics. In addition, we highlight the various characteristics of Quasi-periodic Oscillations frequently seen in black hole systems and also discuss the various pseudo potentials commonly used to mimic the space-time geometry around black holes.

• In **Chapter 2**, we study the steady, geometrically thin, advective, inviscid, axisymmetric accretion flows and associated outflow/jet emerging out from the disc around rotating black holes. When the viscous time-scale of the inflowing matter is much larger than the infall time-scale, one can safely ignore the viscous dissipation in the disc. Following this, we neglect the effect of viscous dissipation in the accretion flow. We mimic the space-time geometry around black holes by considering the pseudo-Kerr potential proposed by Chakrabarti & Mondal (2006) [146]. As the accretion flow proceeds towards the black hole, a part of the inflowing matter comes out between the centrifugal barrier (CB) and funnel wall (FW) as outflows [43, 122]. Considering all these, in this chapter, we self-consistently investigate the accretion-ejection mechanism around rotating black holes. We primarily focus on the effect of black hole spin on the generation of mass outflow. To start with, we examine the effect of spin on the outflow/jet geometry and we find that the outflow/jet geometry remains indistinguishable outside few tens of Schwarzschild radius for both non-rotating and rotating black holes. To present the complete picture of the accretion-ejection mechanism, we examine the shock-induced global inflow-outflow solutions for various spin a_k. Due to the mass loss from the inner part of the disc (PSC), the post-shock pressure is decreased that causes the shock front to move towards the horizon in order to maintain the pressure balance across the shock. We observe that the shock-induced accretion-ejection solutions exist for a wide range of input parameters, namely flow energy ($\mathcal{E}$), flow angular momentum (λ) and spin (a_k) of the black holes. Further, we observe that mass outflow rates increase with the increase of spin for fixed inflow parameters ($\mathcal{E}, \lambda$). Then, we calculate the maximum outflow rates ($R_{\dot{m}}^{\rm max}$) as a function of black hole spin (a_k) by freely varying all inflow parameters ($\mathcal{E}, \lambda$). We observe that there is no significant positive correlation exist between the spin and maximum outflow rates calculated using our accretion-ejection model. Finally, we employ our accretion-ejection model to estimate the kinetic jet power ($L_{\rm jet}^{\rm est}$) for various black hole sources (GBHs and AGNs) based on their accretion sates as well as from their mass accretion rates and good agreement is seen.

• In **Chapter 3**, we put forward our investigation of accretion-ejection mecha-

nism in a steady, geometrically thin, viscous, dissipative, axisymmetric accretion disc around rotating black holes. In a more general sense, in a deferentially rotating flow, the presence of viscous dissipation is inevitable. Thus, in this chapter, we study the dissipative accretion flow in presence of both viscous heating and parametric cooling [20]. On the other hand, since the jets are usually tenuous in nature, we ignore any differential rotation in the outflowing matter and therefore, the outflowing matter is treated to be inviscid. Here, we model the viscosity prescription for the accretion flow considering the mixed shear stress prescription of Chakrabarti (1996) [139] and examine the effect of viscosity on the mass-loss from the disc around rotating black holes. We find that a wide range of viscosity parameters allows shock solutions in absence as well as in presence of mass-loss from the disc. In fact, viscosity plays the dual role within the disc: firstly, viscosity transports angular momentum outward reducing its value at the inner edge and secondly, viscous dissipation causes the heating of the flow as it accretes. As a result, we find that the shock parameter space spanned by flow energy ($\mathcal{E}_{in}$) and flow angular momentum (λ_{in}) is shifted towards higher energy and lower angular momentum side with the increase of viscosity. Ultimately, the allowed shock parameter space shrinks gradually with the increase of viscosity and eventually disappears when viscosity exceeds its critical limit. Further, we investigate the maximum viscosity parameter ($\alpha^{\rm max}$) as a function of spin a_k in absence as well as in presence of mass-loss. We also examine the effect of cooling on the mass-loss by considering parametric form of cooling in the flow [20]. Finally, we calculate the maximum quasi-periodic oscillation frequency ($\nu_{\rm QPO}^{\rm max}$) by estimating the infall time-scale as a function of black hole spin (a_k) [154]. We observe that $\nu_{\rm QPO}^{\rm max}$ is well correlated with the spin of the black hole. We also apply our model to constrain the spin of the source GRO J1655-40 considering the observed high-frequency QPOs (HFQPOs), namely $\sim$ 450 Hz and $\sim$ 300 Hz in this source. We argue that the spin of the source GRO J1655-40 is $a_k \geq 0.57$.

• In **Chapter 4**, we study the global accretion-ejection solutions around the rotating black holes by adopting three widely used pseudo-Kerr potentials proposed by Artemova et al. (1996) [144], Mukhopadhyay (2002) [145] and Chakrabarti & Mondal (2006) [146]. For this purpose, we consider a steady, geometrically thin, advective, viscous, axisymmetric accretion flows around rotating black holes similar to Chapter 3. Here, we assume that the radiative cooling mechanisms are inefficient in the disc. With this, we obtain the shock induced global shocked accretion solutions using various pseudo potentials. We compare the effective region of the parameter space spanned by the energy ($\mathcal{E}_{in}$) and the angular momentum (λ_{in}) of the flow mea-

sured at the inner critical points ($x_{\rm in}$) that allows standing shock solutions. Further, we compare the shock parameter space in terms of the adiabatic index (γ) of the flow. We also compare shock parameter space in terms of various viscosity parameter (α) as well. Then, we calculate critical viscosity ($\alpha^{\rm max}$) limit for all the potentials in terms of black hole spin that admits shock solutions. We observe that all the pseudo potentials under consideration are qualitatively similar as far as the standing shocks are concerned, however, they differ both qualitatively and quantitatively from each other for rapidly rotating black holes. We also compare the maximum outflow rates ($R_{\rm in}^{\rm max}$) in terms of black hole spin for all the potentials. Finally, we apply our accretion-ejection formalism to estimate the maximum kinetic jet power and compare it with radio jet power of low-hard state of the BH-XRBs. Based on the comparative study, we indicate that black hole XRBs along the 'outliers' track are mostly rapidly rotating.

• In **Chapter 5**, we consider a non-steady, two-dimensional, axisymmetric, inviscid accretion flow around a rotating black hole. In general, there are six sets of partial differential equations for the density, momentum, thermal and radiation energy for the accretion flow hydrodynamics. In this work, we assume that the accretion disc is fully optically thin and neglect the radiative cooling processes in our model [155]. Also, the space-time geometry around the black hole is modeled using the pseudo-Kerr potential proposed by Artemova-etal (1996) [144]. The time dependent differential equations are numerically solved by explicit-implicit finite difference method scheme under the initial and boundary conditions [156–158]. In general, the post-shock flow (PSC) is very hot and compressed acting as a source of high energy radiations [35]. With the suitable choice of flow parameters, we find that shock starts to oscillate and as a result, PSC modulates in the radial direction. Hence, the photon flux coming out from the disc is also modulated and produced quasi-periodic oscillations (QPOs). When the PSC rapidly modulates, it generates High frequency Quasi-periodic Oscillations (HFQPOs). In this work, we carry out the numerical simulation to study the HFQPOs from the radial shock oscillation. We observe that several sets of model parameters yield HFQPOs ($\geq$ 40 Hz). We present five such numerical models that exhibit HFQPOs consistent with the observed HFQPOs in *LAXPC/AstroSat* and *RXTE* for the black hole source GRS 1915+105.

• In **Chapter 6**, we present conclusion along with the summary of the important outcomes from the thesis. We also describe the possible extensions of our work.

Chapter 2

Mass-loss from advective accretion disc around rotating black holes

.

Powerful jets and outflows are ubiquitous in accreting black hole systems (AGNs and XRBs) [52–58, 60, 159]. In spite of the rigorous investigations in both theoretical as well as observation fronts, the underline physical mechanisms of jet generation and its powering processes are still remain unclear. Earlier theoretical works demonstrated that infalling particles on to a rotating black hole have the potential to extract some of the rotational energy of the black holes [71, 72]. In terms of observation, several attempts have been made to investigate the correlation between the jet power and the spin of the black hole based on radio observations considering stellar mass black holes. In this regard, Steiner et al. (2013) [101] and McClintock et al. (2014) [102] observed significant positive correlation between the transient jet power and the spin of the black hole. However, Russell et al. (2013) [103] and Fender & Gallo (2014) [66] ruled out the direct evidence of any such correlation between the transient jet power and the black hole spin. In a numerical endeavor, De Villiers et al. (2005) [80] claimed that the jet efficiency increases by two orders of magnitude for rapidly rotating black hole compared to the non-spinning black hole. In the similar context, Fernandez et al. (2015) [151] showed that more mass is evacuated from the disc as the black hole spin is increased. In an early effort, Donea & Biermann (1996) [160] also found that the jet power is strongly dependent on the spin of the black hole without considering the jet geometry. Overall, all the above findings are in contrast and therefore, inconclusive.

The contents of this chapter is published in Aktar R., Das S., Nandi A., MNRAS **453**, 3414 (2015)

In a realistic scenario, advective accretion flow around the black holes must be transonic in nature just to satisfy the inner boundary conditions. Such Inflowing matter experiences discontinuous transition in flow variables as a result of triggering the shock wave [37–39, 161, 162]. Due to compression, the shock induced accretion flow produces hot and dense post-shock corona (PSC) surrounding the black holes which essentially acts as the effective boundary layer of the black holes. During accretion, a part of the inflowing matter is deflected by PSC which is further driven out in the vertical direction by the excess thermal gradient force across the shock, producing bipolar outflows. Such an appealing mechanism to launch outflow from the vicinity of the black hole has been confirmed through numerical simulations [80, 122, 125, 163–166]. In addition, numerous attempts have been made theoretically to calculate the mass outflow rate around black holes. Chakrabarti (1999) [41] calculated the mass outflow rate considering isothermal flow. Using both Keplerian and sub-Keplerian components, Das et al. (2001) [167] self-consistently estimated mass loss from the disc and found that outflow rate strongly depends on both components. Singh & Chakrabarti (2011) [168] implemented the energy dissipation across the shock while obtaining the outflow rate and found that possibility of mass loss anti-correlates with the dissipation rate. Following the work of Molteni et al. (1996) [154], several authors [43–45, 125, 169] studied the properties of mass outflow rate in terms of inflow parameters considering dissipative accretion flow. However, all these works were carried out with limitation as spin of the black hole was not considered. Motivating with this, in the following Sections, we study the disc-jet solution around a rotating black hole and explore its implication in the context of observation.

2.1 Model Equations and Assumptions

We consider an axisymmetric disc-jet system around a rotating black hole in the steady state. Here, the accretion disc lies along the black hole equatorial plane while the jet geometry is described about the black hole rotation axis. In this work, we mainly focus on the inner region of the accretion disc, where the viscous time scale is larger than the in-fall time scale and therefore, the angular momentum transport due to the differential motion is weakly significant leaving the flow to be inviscid there [38]. Further, in our model, jets are originated from the inner part of the accretion disc (PSC) with the same angular momentum of the disc as we neglect the effect of resulting torque in the disc-jet system. Next, we present the governing equations that describe the fluid properties of the accretion disc and the

jets. In this Thesis, all the equations are written in a unit system considered as $G = M_{\rm BH} = c = 1$, where G is the Gravitational constant, $M_{\rm BH}$ is the black hole mass and c is the speed of light, respectively. In this unit system, the unit of length, mass and time are expressed as $GM_{\rm BH}/c^2$, $M_{\rm BH}$ and $GM_{\rm BH}/c^3$.

2.1.1 Governing equations for Accretion

We consider a geometrically thin, axisymmetric, low angular momentum, advective accretion flow around a rotating black hole. For simplicity, we adopt the pseudo-Kerr effective potential introduced by Chakrabarti & Mondal (2006) [146] to represent the space-time geometry around the black hole instead of using full general relativistic prescription. This enables us to solve the problem following the Newtonian approach and keeping all the salient features of space-time geometry around it. The equation of motion describing the accreting matter is given by (see §1.5),

(i) the energy conservation equation:

$$\mathcal{E} = \frac{v^2}{2} + \frac{a^2}{\gamma - 1} + \Phi^{\rm eff}, \tag{2.1}$$

where, $\mathcal{E}$ represent the specific energy of the flow, v is the radial velocity and a is the adiabatic sound speed defined as $a = \sqrt{\gamma P/\rho}$. Here, P is the isotropic pressure, ρ is the gas density, γ is the adiabatic index, respectively. The accreting gas is described by the adiabatic equation of state as $P = K\rho^{\gamma}$, where K is the measure of specific entropy, which is constant except at the shock transition. The effective potential $\Phi^{\rm eff}$ is given by [146],

$$\Phi^{\rm eff} = -\frac{B + \sqrt{B^2 - 4AC}}{2A}, \tag{2.2}$$

where,

$$A = \frac{\alpha^2\lambda^2}{2x^2},$$

$$B = -1 + \frac{\alpha^2\omega\lambda r^2}{x^2} + \frac{2a_k\lambda}{r^2 x},$$

$$C = 1 - \frac{1}{r - x_0} + \frac{2a_k\omega}{x} + \frac{\alpha^2\omega^2 r^4}{2x^2}.$$

Here, x and r represent the cylindrical and spherical radial distance considering the

black hole is located at the origin of the coordinate system and λ is the specific angular momentum of the flow. Here, $x_0 = 0.04 + 0.97a_k + 0.085a_k^2$, $\omega = 2a_k/(x^3 + a_k^2x + 2a_k^2)$ and $\alpha^2 = (x^2 - 2x + a_k^2)/(x^2 + a_k^2 + 2a_k^2/x)$, α is the redshift factor and a_k represents the black hole rotation parameter defined as the specific spin angular momentum of the black hole. According to Chakrabarti & Mondal (2006) [146], the above potential mimic the Kerr geometry quite satisfactorily for a wide range of $a_k \lesssim 0.8$.

(ii) the mass conservation equation:

$$\dot{M} = 4\pi\rho v x h, \tag{2.3}$$

where, $\dot{M}$ denotes the mass accretion rate which is constant everywhere except the region of mass loss and h is the half-thickness of the disk obtained from thin disk approximation [38] as,

$$h(x) = a\sqrt{\frac{x}{\gamma\Phi_r'}}, \tag{2.4}$$

where, $\Phi_r' = (\partial\Phi^{\rm eff}/\partial r)_{z<<x}$, z is the vertical height in the cylindrical coordinate system and $r = \sqrt{x^2 + z^2}$.

Combining the expression of sound speed and the adiabatic equation of the state of the gas, we calculate the entropy accretion rate as [36],

$$\dot{\mathcal{M}} = va^{\nu}\sqrt{\frac{x^3}{\gamma\Phi_r'}}, \tag{2.5}$$

where, $\nu = (\gamma+1)/(\gamma-1)$. In an accretion disk, $\dot{\mathcal{M}}$ remain constant all throughout except at the shock transition where local turbulence generates entropy. Therefore, the entropy accretion rate in the post-shock region is higher than that in the pre-shock region.

By definition, the accretion flow around the black holes must be transonic in nature. This is due to the fact that the velocity of the accreting matter at large distances from the black hole is negligibly small and therefore, the flow is subsonic. However, flow crosses the event horizon with velocity equivalent to the speed of light implying that the flow is supersonic close to the black hole. This clearly indicates that the accretion flow necessarily changes its sonic state during its journey from the outer edge of the disc to the horizon. In order to calculate the location where the state of this sonic transition occurs, we derive the sonic point conditions using

Eqs. (2.1 - 2.5) and obtain as,

$$\frac{dv}{dx} = \frac{N}{D}, \tag{2.6}$$

where,

$$N = \frac{a^2}{\gamma+1}\left[\frac{3}{x} - \frac{d\ln\Phi_r^{'}}{dx}\right] - \frac{d\Phi_e^{\rm eff}}{dx}, \tag{2.7}$$

and

$$D = v - \frac{2a^2}{(\gamma+1)v}, \tag{2.8}$$

where, the subscript 'e' signifies the quantity measured at the disc equatorial plane. Since the accretion flow is smooth everywhere, the radial velocity gradient must be finite everywhere too. According to Eq. 2.6, if the denominator D vanishes at any radial distance, the numerator N also vanishes there. Such a location, where $D = N = 0$, is called as sonic point. Setting $D = 0$ and $N = 0$ independently, we find the sonic point conditions as,

$$D = 0 \Rightarrow M_c = \frac{v_c}{a_c} = \sqrt{\frac{2}{\gamma+1}}, \tag{2.9}$$

and

$$N = 0 \Rightarrow a_c^2 = (\gamma+1)\left(\frac{d\Phi_e^{\rm eff}}{dx}\right)_c \left[\frac{3}{x} - \frac{d\ln\Phi_r^{'}}{dx}\right]_c^{-1}. \tag{2.10}$$

Here, the subscript 'c' denotes the quantities evaluated at the sonic points. We use sonic point conditions, namely, Eqs. (2.9 - 2.10), in Eq. 2.1 to obtain the location of sonic point for a given set of ($\mathcal{E}$, λ) of the flow. For a physically acceptable transonic solution, flow must contain at least one saddle type sonic point (Das et al. (2007) [170] and references therein). Depending on the values of $\mathcal{E}$ and λ, flow may possess multiple sonic points as well which is one of the necessary condition to form a shock wave [36]. At the sonic point, Eq. 2.6 takes the form as $dv/dr = 0/0$ and therefore, we use l'Hospital rule to calculate the radial velocity gradient there. Once the flow variables at the sonic point are known, we integrate Eq. 2.6 starting from the sonic point inward up to the black hole horizon and outward to a large distance to obtain the full set of global accretion solution which may own standing shock waves.

2.1.2 Governing equations for Outflow

In this work, we consider the outflow to be emerged out from the accretion disc along the rotation axis of the black hole with the same energy and angular momentum as the accretion flow since we neglect the dissipative processes (i.e., viscosity, cooling etc.). Similar to accretion flow, we consider the outflow to obey the polytropic equation of state as $P_j = K_j \rho_j^{\gamma}$, where, the suffix '$j$' denotes the outflow variables. The equations of motion that describe the outflow dynamics are given by,

(i) *the energy conservation equation of outflow*:

$$\mathcal{E}_j = \frac{1}{2} v_j^2 + \frac{a_j^2}{\gamma - 1} + \Phi^{\rm eff}, \tag{2.11}$$

where $\mathcal{E}_j$ ($\equiv \mathcal{E}$) represent the specific energy of the outflow, v_j is the outflow velocity and a_j is the sound speed of the outflow, respectively.

(ii) *Mass conservation equation of outflow*:

$$\dot{M}_{\rm out} = \rho_j v_j \mathcal{A}, \tag{2.12}$$

where, $\mathcal{A}$ is a geometrical quantity representing the total area function of the outflow. To obtain $\mathcal{A}$, we consider the outflow geometry as described in Molteni et al. (1996) [154] where the outflowing matter tends to come out through the two surfaces, namely the centrifugal barrier (CB) and the funnel wall (FW). We calculate the centrifugal barrier by identifying the pressure maxima surface as $(d\Phi^{\rm eff}/dx)_{r_{\rm CB}} = 0$ and the funnel wall by defining the null effective potential as $\Phi^{\rm eff}|_{r_{\rm FW}} = 0$ [154]. As the effective potential of our interest is complex in nature, it is unattainable to prevail an analytical expression of the CB surface and the FW and therefore, we compute them numerically. In Figure 2.1, we illustrate the outflow geometry around the rotating black holes for a wide range of a_k marked in the figure and compare them with the same obtained using the pseudo-Newtonian potential introduced by Paczyński & Witta (1980) [3] appropriate for a stationary black hole. The regions bounded by the dashed and dotted curves are for $a_k = -0.998$ and $a_k = 0.8$, respectively and the solid curves depict the result of stationary black hole. Note that the outflow geometry for stationary as well as for rotating black holes is indistinguishable outside the range of few tens of Schwarzschild radius. This is possibly due to the fact that the effect of black hole spin on the space-time geometry cursorily diminishes with the increasing distances. Keeping this in mind, we therefore adopt the outflow geometry of the stationary black hole for our present study in order to avoid the

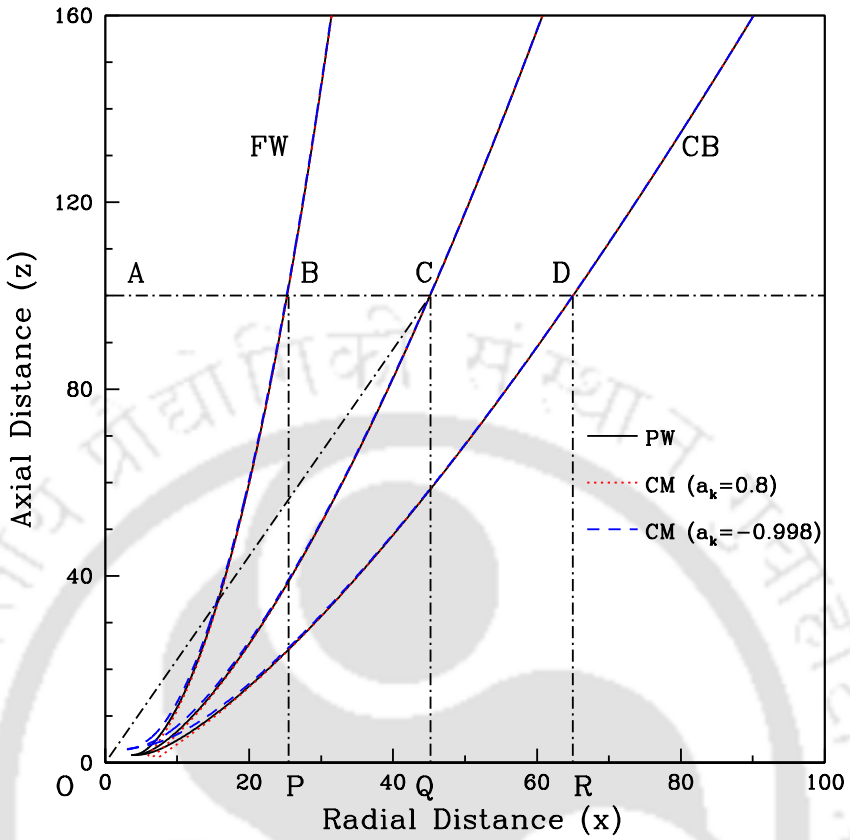

Figure 2.1: Comparison of jet geometry for angular momentum $\lambda = 3.3$. Funnel wall (FW) and centrifugal barrier (CB) are marked in the figure. Here, OC $= r_j$ is the spherical radius representing the streamline of the outflow. Dashed and dotted are obtained for $a_k = -0.998$ and 0.8 while solid curve denotes the result obtained using pseudo-Newtonian potential [3]. Jet geometries for stationary as well as rotating black holes are indistinguishable beyond few tens of Schwarzschild radius. See text for details.

rigorous numerical calculations. This enables us to obtain an analytical expression of area function $\mathcal{A}$ and its higher order derivatives, which is required in the sonic point analysis of outflowing matter [44]. A comprehensive study of sonic point analysis for outflows including the area function $\mathcal{A}$ and its derivatives have already been presented in Das & Chattopadhyay (2008) [44] and therefore, we avoid repetition here.

2.2 Solution Methodology

In this study, we consider the post-shock matter (PSC) as the precursor of the jet base and thus, we focus only to those accretion solutions that possess standing shock

waves. For shock, the accretion flow variables experience discontinuous transition characterized by the Rankine-Hugoniot (hereafter R-H) shock conditions [40]. These conditions include the conservations of mass flux, energy flux and momentum flux across the shock, respectively. In presence of mass loss, a part of the inflowing matter is effectively emerged out as outflow from the post-shock region (PSC), while the remaining matter is advected in to the black hole straight away. Therefore, in the present scenario, the shock conditions are given by,

(i) *Conservation of mass flux*:

$$\dot{M}_+ = \dot{M}_- - \dot{M}_{\rm out} = \dot{M}_-(1 - R_{\dot{m}}). \tag{2.13}$$

The quantities having subscripts '-' and '+' are referred to the values before and after the shock which we follow throughout the chapter unless otherwise stated. The pre-shock and post-shock accretion rates are denoted by $\dot{M}_-$ and $\dot{M}_+$, respectively and $\dot{M}_{\rm out}$ is the mass flux for the outflowing matter. Following this, the mass outflow rate is computed as $R_{\dot{m}} = \dot{M}_{\rm out}/\dot{M}_-$. The next condition is

(ii) *Conservation of energy flux*:

$$\mathcal{E}_+ = \mathcal{E}_-, \tag{2.14}$$

and finally, we have

(iii) *Conservation of momentum flux*:

$$W_+ + \Sigma_+ v_+^2 = W_- + \Sigma_- v_-^2, \tag{2.15}$$

where, W and Σ represent the vertically integrated pressure and density [167].

We rewrite Eq. 2.14 and Eq. 2.15 in terms of Mach number ($M = v/a$) and are given by,

$$\frac{1}{2}M_+^2 a_+^2 + \frac{a_+^2}{\gamma - 1} = \frac{1}{2}M_-^2 a_-^2 + \frac{a_-^2}{\gamma - 1} \tag{2.16}$$

and

$$\left[\frac{2a_+}{(3\gamma - 1)M_+} + M_+ a_+\right] = \frac{1}{1 - R_{\dot{m}}}\left[\frac{2a_-}{(3\gamma - 1)M_-} + M_- a_-\right], \tag{2.17}$$

where we utilize Eq. 2.14 and $a = \sqrt{(3\gamma - 1)W/(2\Sigma)}$ [167].

Using Eqs. (2.14 - 2.17), we obtain a shock invariant quantity (C_s) in terms of

Mach number M as,

$$C_s = \frac{\left[\frac{2}{M_+} + (3\gamma - 1)M_+\right]^2 (1 - R_{\dot{m}})^2}{[2 + (\gamma - 1)M_+^2]} = \frac{\left[\frac{2}{M_-} + (3\gamma - 1)M_-\right]^2}{[2 + (\gamma - 1)M_-^2]}, \tag{2.18}$$

where, M_- and M_+ stand for Mach number just before and after the shock in the pre-shock and post-shock flow, respectively.

Since the shock conditions are coupled with inflow and outflow variables, the accretion and jet equations are solved simultaneously. We obtain the jet velocity gradient from its governing equations and calculate the sonic point properties following the 'critical point' analysis [38]. While doing this, we use the inflow parameters, namely, energy $\mathcal{E}$ and angular momentum λ of the inflow. This is because the outflow is considered to be originated from the the post-shock region (PSC). This also ensures that the jets are launched with the same density as the post-shock flow, namely $\rho_j = \rho_+$. Further, we integrate the jet equations to calculate the outflow variables at the jet base starting from the jet sonic point and using Eqs. 2.3, 2.4 and 2.12, we compute the mass outflow rate in terms of the inflow-outflow properties at the shock and is given by,

$$R_{\dot{m}} = \frac{\dot{M}_{\rm out}}{\dot{M}_-} = \frac{\rho_j v_j(x_s)\mathcal{A}(x_s)}{4\pi\rho_- v_- x_s h_-} = \frac{R v_j(x_s)\mathcal{A}(x_s)}{4\pi\sqrt{\frac{1}{\gamma}} x_s^{3/2} {\Phi'_r}^{-1/2} a_+ v_-}, \tag{2.19}$$

where, $R = \Sigma_+/\Sigma_-(\equiv \rho_+ h_+/\rho_- h_- = \rho_j a_+/\rho_- a_-)$, is the compression ratio and $v_j(x_s)$ and $\mathcal{A}(x_s)$ are the jet velocity and the jet area function at the shock, respectively. We utilize an iterative method to calculate $R_{\dot{m}}$ self-consistently which is given as follows:

We begin with $R_{\dot{m}} = 0$. Using the shock invariant quantity, we calculate the virtual shock location $x_s^{\rm v}$ for a given set of ($\mathcal{E}$, λ) with the consideration that the entropy of the inflowing post-shock matter ($\dot{\mathcal{M}}_+$) and outflowing matter ($\dot{\mathcal{M}}_{\rm out}$) are larger than the entropy of the pre-shock matter ($\dot{\mathcal{M}}_-$). This eventually reflects the fact of second law of thermodynamics as the shocked solutions ascertain the preferred mode of accretion. We use the same set of inflow parameters for jet equations and calculate $R_{\dot{m}}$ which we employ further in the shock invariant equation to obtain a new shock location. We continue this iteration process until the solution converges to the actual shock location and accordingly we compute the corresponding $R_{\dot{m}}$. In the following Sections, we investigate the properties of x_s and $R_{\dot{m}}$ in terms of the inflow parameters ($\mathcal{E}$, λ) for various values of black hole spin (a_k) and present the

results which are followed by the discussion on astrophysical applications.

2.3 Results and Discussions

In an advective accretion process around black holes, the accreting matter suffers discontinuous shock transitions due to the centrifugal barrier. This causes the post-shock flow to become hot and puffed up which eventually behaves like a effective boundary layer around the black hole (i.e., PSC). During accretion, a part of the inflowing matter is deflected vertically by this boundary layer to produce thermally driven outflows. To illustrate the complete picture of the accretion and ejection mechanism, we present the global inflow-outflow solutions for various a_k in Fig. 2.2. In panel (a), (b) and (c), we show the variation of Mach number ($M = v/a$) of the inflow with the radial distance (x) for a_k = 0.8, 0.0, and -0.998, respectively. Subsonic matter at large distance gradually gains its radial velocity as it proceeds towards the black hole due to the fatal attraction of gravity and crosses the outer sonic point ($x_{\rm out}$) to become supersonic as shown by the arrows. As the flow continues its journey further towards the black hole, it experiences discontinuous transition in flow variables when the R-H conditions are favorable which is indicated by the dashed vertical arrow. After this transition, flow momentarily slows down and gradually picks up its velocity. Eventually, flow becomes supersonic again after crossing the inner sonic point ($x_{\rm in}$) and finally enters in to the black hole. As the outflow is emerged out from the effective boundary layer of the black hole, the density of the post-shock flow is decreased causing the reduction of pressure at PSC as well. In order to maintain the pressure balance across the standing shock in presence of mass loss, shock itself has to move inward which is indicated by the solid vertical arrow. In the panel (d), we plot the Mach number (M_j) variation of the outflowing matter with its radial coordinate (x_j) corresponding to panel (a), (b) and (c). The black solid circles represent the sonic locations and the arrows show the direction of motion of the outflowing matter. The inflow parameters for panel (a) is ($\mathcal{E}$, λ) =(0.007, 2.65), for (b) is (0.0025, 3.45) and for (c) is (0.0015, 4.0), respectively.

In Fig. 2.3, we compare the location of the shock transitions as function of energy $\mathcal{E}$ for a set of angular momentum λ. In the upper panel, we choose $a_k = 0.6$ and find that the inflow-outflow solution possesses shock wave for a wide range of $\mathcal{E}$ and λ. As anticipated in Fig. 2.2, the shock location moves towards to the black hole horizon when $R_{\dot{\rm m}} \neq 0$ just to maintain the pressure balance across the shock. We again observe that the shock location reaches to its lowest value around $x_s^{\rm min} \sim 8r_g$

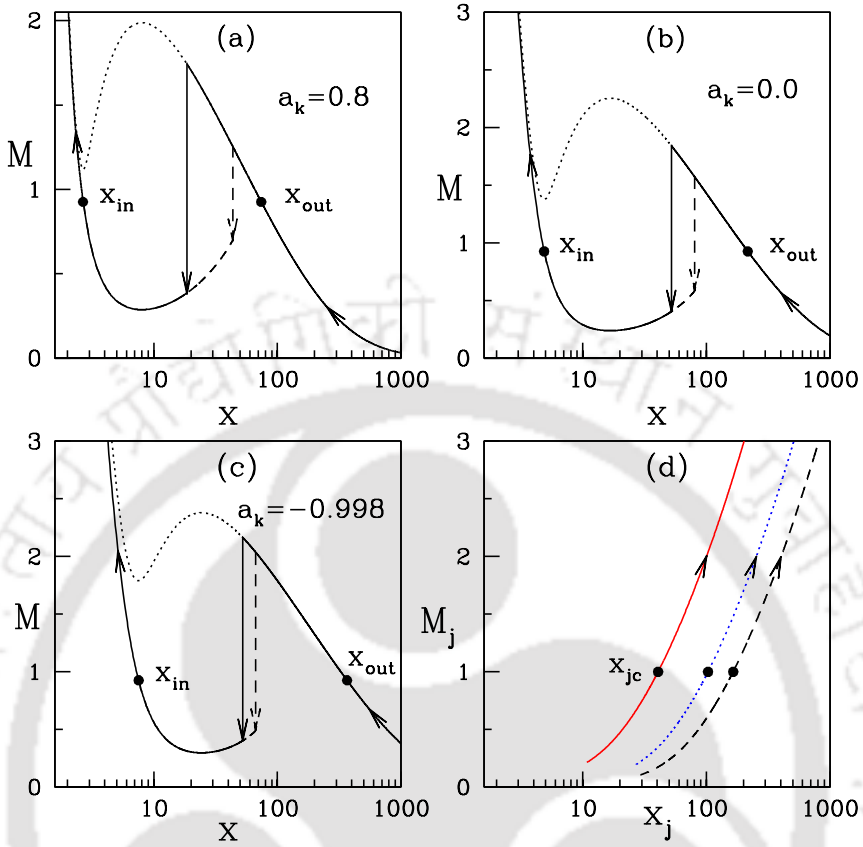

Figure 2.2: Variation of the inflowing Mach number $M(= v/a)$ with radial distances (x) for (a) a_k = 0.8, (b) a_k = 0 and (c) a_k = -0.998, respectively. The corresponding outflow Mach number $M_j(= v_j/a_j)$ variation is shown in panel (d). See the text for details.

at energies higher compared to the case of $R_{\dot{m}} = 0$ and the limiting value of this energy increases with the decrease of angular momentum of the flow. However, the maximum value of energy that allows shock transition in presence of mass loss is identical with no mass loss case. This provides a clear hint that the range of inflow parameters for outflows, namely energy $\mathcal{E}$ and angular momentum λ are reduced from their lower ends. In the lower panel, we consider $a_k = -0.6$ and obtained the similar results which differ only quantitatively. Overall, it is clear that the possibility of shock formation is affected substantially due to the presence of outflow.

Before we proceed further, we now investigate the effect of the black hole rotation on the generation of mass outflow rate. In Fig. 2.4, we present the variation of shock location (x_s) and outflow rate $(R_{\dot{m}})$ as function of a_k. Here, we fix $\mathcal{E} = 0.002$ and vary λ from 2.8 to 3.92 from the right most curve to the left most with an interval $\Delta\lambda = 0.16$. In the upper panel, the solid curves represent the shock locations in

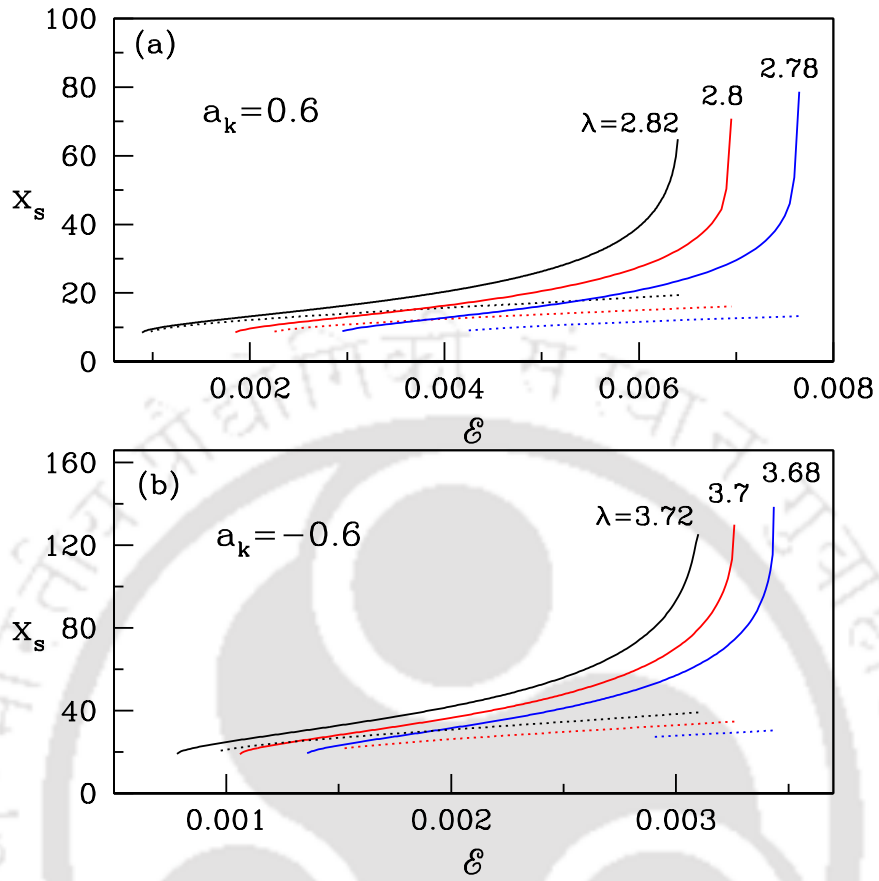

Figure 2.3: Variation of shock location as function of energy $\mathcal{E}$. The solid curves represent results without mass loss and the dotted curves are with mass loss. In the upper panel, we choose $a_k = 0.6$ and curves are for $\lambda = 2.78$ (right), 2.80 (middle) and 2.82 (left), respectively. In the lower panel, we consider $a_k = -0.6$ and curves are for $\lambda = 3.68$ (right), 3.70 (middle) and 3.72 (left), respectively.

absence of mass loss. However, in presence of mass loss, accretion flow adjusts the location of the shock transition closer to the black hole horizon in a way that the pressure balance condition across the shock is maintained which is depicted by the dashed curves. On the contrary, as a_k is increased for a set of $\mathcal{E}$ and λ, the shock locations recede away from the black hole horizon. This indicates that the size of the post-shock region (PSC) is enhanced with the increase of a_k and the inflowing matter is eventually intercepted by the large effective area of the post-shock flow that produces more outflow rate. In the lower panel, we present the feature of outflow rate variation with a_k. For a set of $\mathcal{E}$ and λ, the outflow rate $R_{\dot{m}}$ shows non-linear correlation for prograde as well as retrograde flows. In addition, we observe that for a given a_k, $R_{\dot{m}}$ is higher for increasing λ and with this, we infer that large outflow rate is associated with the higher λ and lower a_k when $\mathcal{E}$ is fixed. Overall, we find

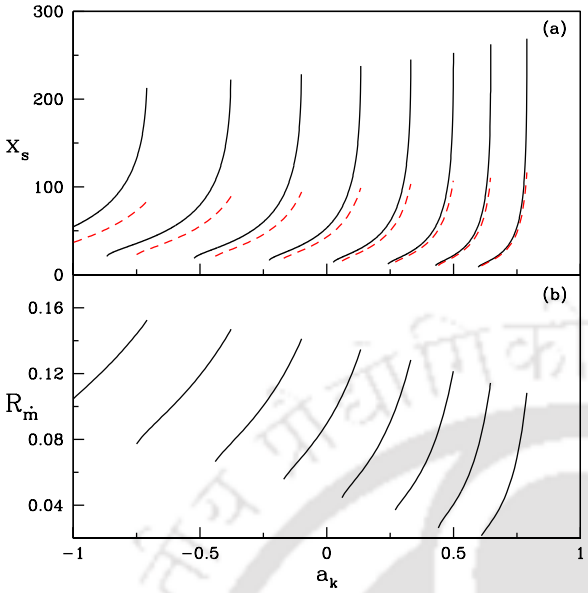

Figure 2.4: Variation of (a) shock location (x_s) and (b) outflow rates ($R_{\dot{m}}$) with the variation of spin (a_k) for different angular momentum. Here, $\lambda = 2.8$ to 3.92 (left to right) with $\Delta\lambda = 0.16$ and inflow energy $\mathcal{E} = 0.002$.

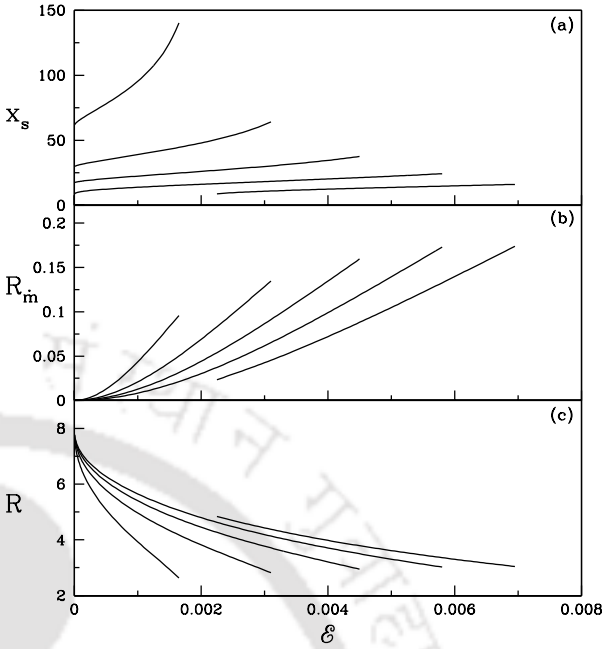

Figure 2.5: Variation of (a) shock location (x_s), (b) outflow rates ($R_{\dot{m}}$) and (c) compression ratio (R) with the variation of flow energy ($\mathcal{E}$) for different spin values. Here, $a_k = 0.8$ to 0.6 (left to right) with $\Delta a_k = 0.05$ and inflow angular momentum $\lambda = 2.8$.

that outflow rate reaches close to 16% for these parameters as depicted in the figure.

Next, we study the characteristics of the post-shock quantities in terms of the inflow variables and present them in Fig. 2.5. Here, we choose the angular momentum as $\lambda = 2.8$ and vary energy $\mathcal{E}$ and black hole rotation parameter a_k. In the upper panel, we plot the variation of shock location (x_s) with $\mathcal{E}$ for a_k varied from 0.6 (right) to 0.8 (left) with $\Delta a_k = 0.05$. The corresponding variation of outflow rate $R_{\dot{m}}$ is shown in the middle panel. Due to shock transition, the post-shock flow is compressed. The measure of this compression is quantified as the ratio of the post-shock density to the pre-shock density and it is termed as shock compression ratio R. In the lower panel, we present the variation of R with $\mathcal{E}$. When shock forms closer to the black hole horizon, the amount of gravitational potential energy release is higher ensuing the formation of strong shock. As the energy is increased, the shock location moves outward that increases the outflow rate and weakens the shock compression ratio. We observe similar behaviour for all a_k. However, for a

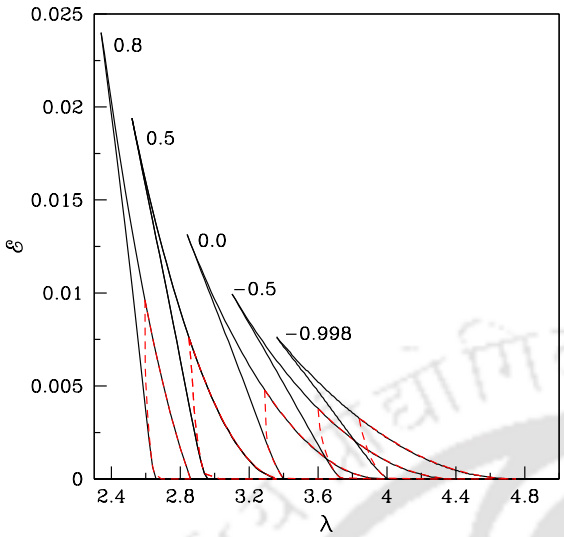

Figure 2.6: Energy angular momentum parameter space. Solid curve (black): shock parameter space without outflow. Dashed curve (red): shock parameter space with outflow. Various values of a_k are marked in the figure.

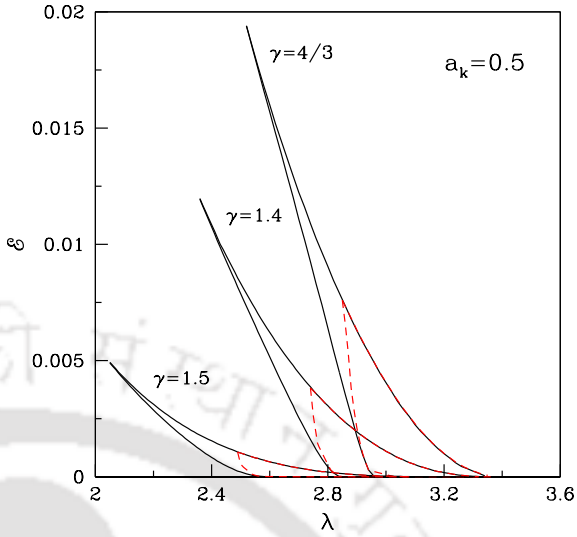

Figure 2.7: Effective regions of parameter space separated in terms of shock waves transition for various values of γ marked in the figure. Here, we choose $a_k = 0.5$. The solid boundary denotes the presence of shock waves in absence of mass loss and the dashed boundary represents the results including mass loss.

given λ and a_k, there is a range of energy beyond which mass outflow ceases to exist. This provides an indication of finding a parameter space for shock in the fundamental plane of energy and angular momentum of the inflow.

As we pointed out earlier that the transonic accretion solutions including R-H shock waves are not isolated solutions. In fact, these solutions do exist for a wide range of parameters, namely, energy ($\mathcal{E}$), angular momentum (λ), and black hole rotation parameter (a_k). Towards this, we identify the shock induced global accretion solutions using the parameter space spanned by the energy ($\mathcal{E}$) and angular momentum (λ) of the flow and classify them in terms of a_k. In Fig. 2.6, we separate the parameter spaces with the solid boundaries that indicate the regions for global shock accretion solutions in absence of mass loss. The corresponding values of a_k are marked in the figure. We further investigate the parameter spaces that cater mass loss and indicate it with the dashed boundaries. Due to mass loss, the post-shock region (PSC) shrinks as seen in Fig. 2.2, and therefore, the associated parameter space is reduced compared to the results having no outflows, particularly towards the lower energy and lower angular momentum sides (see Fig. 2.3). For flows with

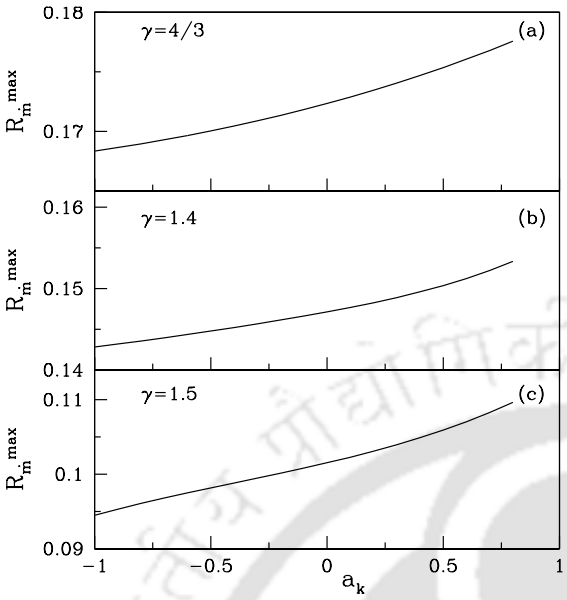

Figure 2.8: Variation of maximum outflow rates $R_{\dot{m}}^{\max}$ with the BH rotation parameter a_k. Upper panel is for $\gamma = 4/3$ (a), middle panel is for $\gamma = 1.4$ (b) and bottom panel is for $\gamma = 1.5$ (c), respectively. See the text for details.

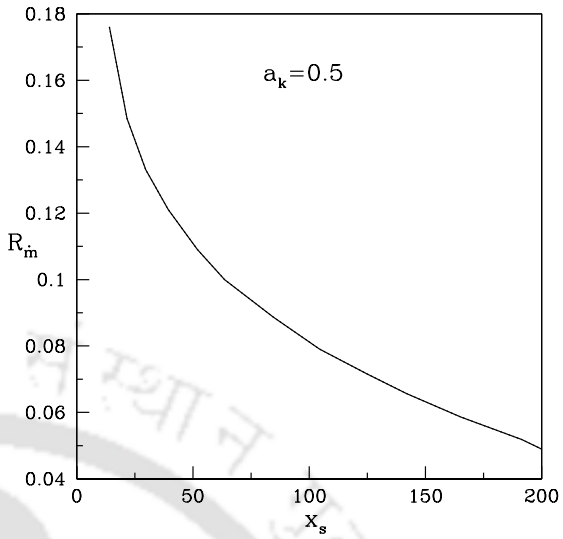

Figure 2.9: Variation of outflow rate ($R_{\dot{m}}$) with shock location (x_s) obtained for different sets of energy ($\mathcal{E}$) and angular momentum (λ). Here, $a_k = 0.5$ is used for representation. See the text for details.

input parameters chosen from these part of the parameter space, shock forms very close to the black hole horizon when outflow is ignored [167] and they cease to exist when the outflow is allowed to emerge out from the post-shock disc. ater

So far, we have presented the shock induced complete global inflow-outflow solutions and its properties for a given value of $\gamma = 4/3$. In reality, however, the theoretical limit of γ lies in the range between 4/3 to 5/3 depending on the ratio between the thermal energy and the rest energy of the flow [5]. To infer this, we consider rotating flows that are characterized as thermally ultra-relativistic ($\gamma \sim 4/3$), thermally trans-relativistic ($\gamma \sim 1.4$) and thermally semi-non-relativistic ($\gamma \sim 1.5$), respectively [169] and obtain the parameter spaces for $a_k = 0.5$ similar to Fig. 2.6. This is shown in Fig. 2.7. Here, we observe that in all three cases shocks exist for significant range of inflow parameters. However, the range of parameters for shock reduces considerably as the flow changes its ultra-relativistic character towards the non-relativistic limit. In addition, we find that all the parameter spaces further

shrink as in Fig. 2.6, when a part of the inflowing matter is deflected in the form of mass loss from the inner part of the disc (PSC).

According to the formalism adopted in this work, the mass outflow rate $R_{\dot{m}}$ is computed self-consistently in terms of the inflow parameters around a black hole of rotation parameter a_k. This allows us to estimate the maximum $R_{\dot{m}}^{\rm max}$ for a given value of γ. While doing this, we identify a particular set of energy ($\mathcal{E}$) and angular momentum (λ) from their full range that provides the highest value of $R_{\dot{m}}$. The importance of this investigation is associated with the study of the maximum jet kinetic power corresponding to $R_{\dot{m}}^{\rm max}$, which we discuss in the next section. Following Fig. 2.7, we calculate the variation of $R_{\dot{m}}^{\rm max}$ as function of a_k for various values of γ which is presented in Fig. 2.8. The results displayed in upper, middle and bottom panels are for $\gamma = 4/3$, 1.4 and 1.5, respectively. We find that $R_{\dot{m}}^{\rm max}$ gradually increase with the increase of a_k for all cases. We also observe that the accretion flows having $\gamma = 4/3$ have the potential to produce more outflows compared to the flows with higher values of γ. This is perhaps inevitable due to the fact that the outflows under consideration are thermally driven and therefore, thermally ultra-relativistic flows exhibit maximum outflows. Following this, in the next Section, we consider $\gamma = 4/3$ while computing the jet kinetic power for GBHs and AGNs, until otherwise stated.

Until now, we discussed the various properties of the accretion-ejection solutions in terms of the inflow parameters. However, all these studies are based on the assumption of stationary state that does not represent the dynamical behaviour of accretion flows around the outbursting BH sources. Usually, these sources change their accretion states with time and the characteristic features of the emergent radiations and the jet properties are also varied accordingly. During these dynamical change of states, it is unlikely that the dissipative properties (i.e., viscosity, cooling processes etc.) of the accretion flow will remain constant all throughout, instead, they seem to adjust in a such way that suitably represents the dynamical variation of PSC. In *LHS* of GBHs, the typical geometry of PSC is quite large which reduces considerably in *HIMS* as the dynamical shock moves towards the black hole during the rising phase of the outburst. Such a trend has been reported while modeling the evolution of QPO frequencies for several black hole sources [49–51, 171–173]. Interestingly, it is also observed that most of the GBH sources show persistent/steady radio emission during these accretion states [59, 65]. Now, we attempt to address the evolution of accretion states from *LHS* to *HIMS* and its association with mass loss using our present formalism as case by case which possibly acts as a local model

at individual time frame. Toward this, a set of energy and angular momentum $(\mathcal{E}, \lambda)$ of the inflowing matter is identified which would represent their local values for a dissipative accretion flow and obtain the shock location x_s and outflow rate $R_{\dot{m}}$ for a given a_k. Since the post-shock geometry (PSC) is associated with x_s, as anticipated earlier, we chose various such sets of $(\mathcal{E}, \lambda)$ in a way that x_s moves towards the black hole and show the variation of $R_{\dot{m}}$ with x_s in Fig. 2.9 for a typical value of $a_k = 0.5$. Note that $R_{\dot{m}}$ is increased with the decrease of x_s resulting more jet kinetic power that represents the common characteristic of radio emissions observed in outbursting sources.

2.4 Astrophysical Application

Here, we attempt to estimate the mass outflow rate and its associated jet kinetic power for various astrophysical black hole sources (GBHs and AGNs) using our present formalism. Since our work deals with the steady outflows, we focus only to those sources particularly to their accretion states where persistent/steady jets are observed. These jets are essentially compact (i.e., optically thick) in nature and are not isolated completely from the core of the central engine [53, 159, 174–176].

2.4.1 Jet kinetic power predicted from Accretion States

We consider five black hole sources namely, XTE J1859+226, GRO J1655-40, GX 339-4, H 1743-322 and GRS 1915+105, respectively. For these sources, mass $(M_{\rm BH})$, distance (d) and spin (a_k) are constrained within the accuracy limit and are given in Table 1. In order to estimate the jet kinetic power, we calculate the X-ray flux for these sources in the *low-hard state* (*LHS*) and *hard-intermediate state* (*HIMS*) using $RXTE$[1] satellite data.

In general, GBH sources undergo outbursts [49–51, 105, 173, 203, 204] and show activity of radio emissions coupled with the accretion states of their evolution during the outburst phases [50, 59, 65, 69, 205, 206]. It has also been observed that most of the outbursting sources show persistent/steady jet activity during *LHS* and *HIMS* while transient 'relativistic' ejections are observed during the transition from hard-intermediate to soft-intermediate state [50, 59, 65, 205].

In order to estimate the 'model predicted' jet power based on accretion states, we estimated X-ray flux from a single observation of each states (i.e., *LHS* and *HIMS*) for all the sources from different outburst phases (as mentioned in the Table-1). We

Table 2.1: Accretion state dependent jet kinetic power.

Objects	$M_{\rm BH}$	d	a_k	Observation $(3-30$ keV)		$\dot{M}_{\rm acc}$	$R_{\rm in}$	$L_{\rm jet}$	$L_{\rm jet}^{\rm Obs}$ #
	$(M_\odot)$	(kpc)		States	F_x (ergs cm^{-2} s^{-1})	$(\dot{M}_{\rm Edd})^*$	(%)	(ergs s^{-1})	(ergs s^{-1})
XTE J1859+226	7	11	0.4	*LHS*	5.71×10^{-9}	0.304	9.83	2.52×10^{37}	
(2009 Outburst)				*HIMS*	12.79×10^{-9}	0.680	17.5	1.08×10^{38}	
									1.82×10^{38} (1)
GRO J1655-40	6.3	3.2	0.7	*LHS*	3.19×10^{-9}	0.016	9.98	1.18×10^{36}	
(2005 Outburst)				*HIMS*	8.02×10^{-9}	0.040	17.68	5.79×10^{36}	
									3.01×10^{36} (2)
GX 339-4	7.5	15	0.4	*LHS*	15.71×10^{-9}	1.450	9.98	1.29×10^{38}	
(2002 Outburst)				*HIMS***	12.12×10^{-9}	1.118	17.5	1.90×10^{38}	
									2.92×10^{38} (1)
H 1743-322	8	8.5	0.2	*HIMS*	4.03×10^{-9}	0.112	17.35	2.01×10^{37}	
(2009 Outburst)									1.08×10^{38} (3)
GRS 1915+105	12.4	8.6	$>0.98^\dagger$	*LHS*	20.33×10^{-9}	0.373	9.98	5.99×10^{37}	
(1997 Observation)									8.06×10^{37} (1)

* $\dot{M}_{\rm Edd} = 1.44\times10^{17}\left(\frac{M_{\rm BH}}{M_\odot}\right)$ gm s^{-1}

** Total flux in *HIMS* $(3-30$ keV) is smaller than *LHS* as the contribution of the hard X-ray flux (>10 keV) in *HIMS* is less.

$L_{\rm jet}^{\rm Obs} = \eta\dot{M}_{\rm out}c^2$ is used for the source H $1743-322$, where $\dot{M}_{\rm out}$ is the outflow rate (see reference). For other sources, $L_{\rm jet}^{\rm Obs} = L_r \times L_{\rm Edd}$ is used, where L_r is the observed jet power (in Edd) (see references) and $L_{\rm Edd} = 1.3\times10^{38}\left(\frac{M_{\rm BH}}{M_\odot}\right)$ ergs s^{-1}.

References: (1) [65] (2) [177] (3) [60]

use archival data obtained from the HEASARC database of the *RXTE* satellite for the estimation of X-ray flux for all the five sources. We extracted and analyzed background-subtracted PCA (3 - 30 keV) spectral data using PCU2 detector (i.e., well calibrated detector) for our specific purpose. The standard FTOOLS package of HEASOFT v6.15.1 was used for spectral data reduction (see [49, 50] for details). For spectral analysis and modeling, we used the packages of XSPEC v12.8.1.

We have done spectral modeling for each observations from each spectral states (i.e., *LHS* and *HIMS*) for all the five sources using PCA spectral data in the energy range of 3 - 30 keV. We model the energy spectrum using the phenomenological accretion disk model i.e., consisting of a *diskbb* and a *power-law* component. In this modeling, the *diskbb* and *power-law* components provide the contribution from the accretion disk and 'hot' Compton corona (i.e., PSC) and thereby one can estimate the total *unabsorbed* X-ray flux (F_x, in units of ergs cm^{-2} s^{-1}) emitted from the

Table 2.2: Estimated jet kinetic power from accretion rate.

Objects	$M_{\rm BH}$ ($M_\odot$)	$\dot{M}_{\rm acc}$ ($\dot{M}_{\rm Edd}$)	a_k	$\mathcal{E}$ (c^2)	λ (cr_g)	x_s (r_g)	$R_{\dot{m}}^{\rm max}$ (%)	$L_{\rm jet}^{\rm max}$ (ergs s^{-1})	$L_{\rm jet}^{\rm Obs}$ # (ergs s^{-1})
A0620-00	6.60 (a)	1.684 (b)	0.12 (b)	0.00444	3.25	26.84	17.25	2.48×10^{38}	...
LMC X-3	6.98 (c)	2.487 (d)	0.25 (e)	0.00476	3.15	25.72	17.35	3.90×10^{38}	...
XTE J1550-564	9.10 (f)	0.511 (g)	0.34 (g)	0.00530	3.06	22.07	17.43	1.05×10^{38}	3.55×10^{38} (y)
M33 X-7	15.66 (h)	0.718 (i)	0.84† (j)	0.00807	2.61	15.60	17.79	2.59×10^{38}	...
4U 1543-47	9.40 (k)	1.315 (l)	0.43 (l)	0.00565	2.98	21.07	17.48	2.80×10^{37}	...
LMC X-1	10.90 (m)	0.853 (n)	0.92† (n)	0.00830	2.58	15.42	17.93	2.16×10^{37}	...
Cyg X-1	14.80 (o)	0.061 (p)	$\geq 0.95^\dagger$ (p)	0.00835	2.58	15.38	17.98	2.10×10^{37}	3.85×10^{37} (y)
Mrk 79	5.24×10^7 (q)	9.82×10^{-2} (r)	0.70 (s)	0.00730	2.72	16.73	17.68	1.18×10^{44}	...
M87	3.50×10^9 (t)	1.16×10^{-4} (u)	≥ 0.65 (v)	0.00705	2.76	16.94	17.62	9.25×10^{42}	1.00×10^{45} (z)
Sgr A*	4.90×10^6 (w)	7.89×10^{-5} (x)	0.99† (w)	0.00859	2.57	14.71	18.09	9.07×10^{39}	1.00×10^{39} (zz)

$L_{\rm jet}^{\rm Obs} = L_r \times L_{\rm Edd}$, where L_r is the observed jet power (in Edd) (see references). References: (a) [178] (b) [179] (c) [180] (d) [181] (e) [182] (f) [183] (g) [97] (h) [184] (i) [185] (j) [186] (k) [187] (l) [188] (m) [189] (n) [190] (o) [191] (p) [192] (q) [193] (r) [194] (s) [195] (t) [196] (u) [197] (v) [198] (w) [199] (x) [200] (y) [65] (z) [201] (zz) [202]

accretion disk around the GBH sources.

Once we obtain the *unabsorbed* X-ray flux (F_x) of a source, we calculate the X-ray luminosity (L_x) of the source employing the relation $L_x = 4\pi d^2 F_x$, where d is the distance of the source. Assuming the maximum radiative efficiency of the infalling matter around rotating black hole is $\eta \sim 0.3$, we calculate the accretion rate of the black hole as,

$$\dot{M}_{\rm acc} = 2.99 \times 10^{-16} \left(\frac{F_x\ d^2}{c^2}\right) \left(\frac{M_{\rm BH}}{M_\odot}\right)^{-1} \dot{M}_{\rm Edd}. \tag{2.20}$$

Here, $M_{\rm BH}$ denotes the mass of the black hole and $\dot{M}_{\rm Edd}$ represents the Eddington accretion rate. Next, we calculate the mass outflow rate using our theoretical estimate (Eq. 2.19) which has its maximum limit ($R_{\dot{m}}^{\rm max}$) for a particular set of $(a_k, \mathcal{E}, \lambda)$ (see Fig. 2.8). With this, we find the *maximum mass outflow rate* as $\dot{M}_{\rm out} = R_{\dot{m}}^{\rm max} \dot{M}_{\rm acc}$ which successively allows us to compute the *maximum jet kinetic power* as,

$$L_{\rm jet}^{\rm max} = R_{\dot{m}}^{\rm max} \times \dot{M}_{\rm acc} \times c^2 \text{ ergs s}^{-1}. \tag{2.21}$$

As pointed out earlier that steady and persistent radio emissions are observed during *LHS* and *HIMS* [59, 65]. In addition, there are indications that the radio emission increases while the state transition from *LHS* to *HIMS* takes place. Moreover, the radio emission becomes non-steady during the *HIMS* itself just prior to the ejection and it is quite known that the relativistic ejections take place during the transition from *HIMS* to *SIMS* [59, 65]. All these observations perhaps indicate that the persistent jet activity would be maximum during *HIMS*. Therefore, in order to study the outflow properties in the *HIMS*, we consider the maximum outflow rate obtained from our model calculation (see Fig. 2.8) and use it to estimate the jet kinetic power. On the other hand, jet kinetic power in the *LHS* is expected to be lower than the *HIMS* although its quantitative estimate is unclear. Therefore, we use outflow rate to be around $\sim 10\%$ as a representative value while calculating the jet kinetic power for *LHS*. Below, we mention the fundamental properties of each sources and present the details for the estimation of jet kinetic power corresponding to individual states of a particular observation.

XTE J1859 + 226:

Filippenko & Chornock (2001) [207] first presented the dynamical estimate of mass of the source to be around $7.4\pm1.1M_{\odot}$. Recently, Radhika & Nandi (2014) [50] claimed that the mass of XTE J1859 + 226 is perhaps in between $6.58M_{\odot}-8.84M_{\odot}$ which is similar to the prediction of Shaposhnikov & Titarchuk (2009) [208] although the lower mass limit is estimated as $5.4M_{\odot}$ by Corral-Santana et al. (2011) [209]. However, we consider the typical mass of the source as $7M_{\odot}$. The distance of this source is around $d \sim 11$kpc [207]. Steiner et al. (2013) [101] measured the spin as $a_k \sim 0.4$, however, Motta et al. (2014) [210] recently reported the spin of the source is $a_k \sim 0.34$. Since the spin predictions are quite close, we use $a_k \sim 0.4$ for this analysis. We estimate the fluxes F_x (see Table 1) of *LHS* and *HIMS* of the 2009 outburst of the source [50]. The corresponding disc luminosities are calculated as $L_{\rm disc}^{LHS} = 8.26\times10^{37}$ ergs s^{-1} and $L_{\rm disc}^{HIMS} = 1.85\times10^{38}$ ergs s^{-1}, respectively. Now, it is reasonable to assume the accretion efficiency for rotating black hole as $\eta = 0.3$ which corresponds to the accretion rate of the inflowing matter as $\dot{M}_{\rm acc}^{LHS} = 0.304\dot{M}_{\rm Edd}$ in *LHS* and $\dot{M}_{\rm acc}^{HIMS} = 0.680\dot{M}_{\rm Edd}$ in *HIMS*. For *LHS*, we use $R_{\dot{\rm m}} = 9.83\%$ following our theoretical estimate where $x_s = 64.6r_g$ for $a_k = 0.4$, $\mathcal{E} = 0.00198$ and $\lambda = 3.18$. Incorporating these inputs in Eq. 2.21, we obtain the jet kinetic power as $L_{\rm jet}^{LHS} = 2.52 \times 10^{37}$ ergs s^{-1}. The maximum mass outflow rate for *HIMS* corresponding to

$a_k = 0.4$ is obtain from Fig. 2.8 as $R_{\dot{m}}^{\max} = 17.5\%$ for $\mathcal{E} = 0.00547$, and $\lambda = 3.1$, where the shock transition occur at $21.9r_g$. Using these values in Eq. 2.21, we obtain the maximum jet kinetic power as $L_{\rm jet}^{HIMS} = 1.08 \times 10^{38}$ ergs s^{-1} which we regard to be associated with the *Hard-Intermediate* state of this source.

GRO J1655-40:

The mass of the source GRO J1655-40 is reported by Greene et al. (2001) [211] and is given by $6.3M_\odot$. Recently, Motta et al. (2014) [210] estimated the object mass as 5.31 ± 0.07 M$_\odot$. This source is located at around $d \sim 3.2$ kpc and the spin of this source is estimated by Shafee et al. (2006) [212] using *RXTE*[1] and *ASCA* data through the modeling of the thermal spectral continuum and obtained in the range $a_k \sim 0.65 - 0.75$ (and reference therein). Fitting the strong reflection features of iron line in *XMM-Newton* data, Reis et al. (2009) [213] determines the lower limit of the spin of this object $a_k = 0.9$. Motta et al. (2014) [210] calculated the spin of the object using X-ray timing method and found as $a_k = 0.290 \pm 0.003$ which is an inconsistent estimate compared to iron line or continuum methods. In our present analysis, however, we consider $a_k = 0.7$. As before, we analyzed the 2005 outburst of GRO J1655-40 to calculate the X-ray fluxes (F_x) for *LHS* and *HIMS* (see Table 2.1) in the energy range $3 - 30$ keV and obtain the corresponding accretion rates $\dot{M}_{\rm acc}^{LHS} = 0.016\dot{M}_{\rm Edd}$ in *LHS* and $\dot{M}_{\rm acc}^{HIMS} = 0.040\dot{M}_{\rm Edd}$ in *HIMS*. We use $R_{\dot{m}} = 9.98\%$ in case of LHS which is obtained for $a_k = 0.7$, $\mathcal{E} = 0.00258$ and $\lambda = 2.845$ where $x_s = 49.98r_g$. From these values, we estimate jet kinetic power in LHS as $L_{\rm jet}^{LHS} = 1.18 \times 10^{36}$ ergs s^{-1}. For $HIMS$, we estimate of the maximum mass outflow rate for $a_k = 0.7$ (see Fig. 2.8) as $R_{\dot{m}}^{\max} = 17.68\%$ where $\mathcal{E} = 0.0073$ and $\lambda = 2.715$ with $x_s = 16.73r_g$. These inputs provide the maximum jet kinetic power as $L_{\rm jet}^{HIMS} = 5.79 \times 10^{36}$ ergs s^{-1}.

GX 339-4:

The mass of the object is estimated as 7.5 ± 0.8 M$_\odot$ Chen (2011) [214] and distance $d \sim 15$ kpc by Hynes et al. (2004) [215]. The issue of spin measurement of this objects is not settled yet as there are conflicting measurements. Analyzing the *XMM-Newton* data set for broad iron line detection, Reis et al. (2008) [216] and Miller et al. (2008) [217] claimed $a_k = 0.935$ while the disc continuum fitting prefers the lower spin having upper limit of $a_k < 0.9$ [218]. However, analyzing the wide-band *Suzaku* speatra, Yamada et al. (2009) [219] pointed out $a_k < 0.4$. Being aware of these, we consider a conservative estimate of spin as $a_k = 0.4$ in our calculation.

This source has undergone outburst phases several times during RXTE era. For this analysis, we consider the 2002 outburst spectral data (in the energy band of $3-30$ keV) for *LHS* and *HIMS*. During May 2 of 2002 outburst, the object was in *LHS* emitting X-ray flux of $F_x^{LHS} = 15.71\times10^{-9}$ ergs cm^{-2} s^{-1} (see Table 2.1) and the disc luminosity of $L_{\rm disc}^{LHS} = 4.22\times10^{38}$ ergs s^{-1}. Using $\eta = 0.3$, the disc rate is calculated as $\dot{M}_{\rm acc}^{LHS} = 1.450\dot{M}_{\rm Edd}$. Estimating $R_{\dot{m}} = 9.98\%$ from our model using $\mathcal{E} = 0.00198$ and $\lambda = 3.18$ with $x_s = 64.63r_g$, we calculate the jet kinetic power $L_{\rm jet}^{LHS} = 1.29\times10^{38}$ ergs s^{-1}. On May 12 of the 2002 outburst, the source was in *HIMS* and the radiated X-ray flux was calculated as $F_x^{HIMS} = 12.12\times10^{-9}$ ergs cm^{-2} s^{-1} (see Table 2.1) and the disc luminosity of $L_{\rm disc}^{HIMS} = 3.26\times10^{38}$ ergs s^{-1}. Using $\eta = 0.3$, the disc rate is calculated as $\dot{M}_{\rm acc}^{HIMS} = 1.118\dot{M}_{\rm Edd}$. Estimating $R_{\dot{m}}^{\rm max} = 17.5\%$ from our model using $\mathcal{E} = 0.00547$ and $\lambda = 3.1$ with $x_s = 21.9r_g$, we calculate the maximum jet kinetic power $L_{\rm jet}^{HIMS} = 1.90\times10^{38}$ ergs s^{-1}.

H 1743-322:

Miller et al. (2012) [60] and Steiner et al. (2012) [220] reported the mass, distance and spin of H 1743-322 as $\sim 8M_\odot$, $d\sim 8.5$ kpc and $a_k = 0.2$, respectively. Using the RXTE observation of the 2009 outburst of the source, the disc luminosity for this source is computed for the energy range of $3-30$ keV corresponding to the measured X-ray flux of $F_x^{HIMS} = 4.03\times10^{-9}$ ergs cm^{-2} s^{-1} in *HIMS* (see Table 2.1) [69] as 4.63×10^{37} ergs s^{-1}. Assuming $\eta = 0.3$, we obtain the accretion rate as $\dot{M}_{\rm acc}^{HIMS} = 0.112\dot{M}_{\rm Edd}$. Accretion rate in *LHS* is not known due to lack of observation during the 2009 outburst [69]. For $a_k = 0.2$, $\mathcal{E} = 0.00485$ and $\lambda = 3.176$, we obtain the maximum mass outflow rate for *HIMS* as $R_{\dot{m}}^{\rm max} = 17.35\%$ with $x_s = 23.66r_g$. Employing these values, we find the maximum jet kinetic power as $L_{\rm jet}^{HIMS} = 2.01\times10^{37}$ ergs s^{-1}.

GRS 1915+105:

Earlier, Greiner et al. (2001) [221] estimated the mass of GRS 1915+105 as $(14\pm4)\ M_\odot$. Recently, Hurley et al. (2013) [222] reported the new mass estimate as $(12.9\pm2.4)\ M_\odot$ which is further revised as $(12.4\pm2)\ M_\odot$ by Reid et al. (2014) [223]. The distance of the source is reported as $d\sim(9.4\pm0.2)$ kpc by Hurley et al. (2013) [222] and Reid et al. (2014) [223] claimed the distance to be $d\sim(8.6\pm2)$ kpc. However, in this calculation we use the mass and distance of the source as $12.4M_\odot$ and 8.6 kpc, respectively in order to compute the disc luminosity. The source is extremely rotating as McClintock et al. (2006) [224] estimated the spin

parameter $a_k > 0.98$ which is similar to the estimate of Blum et al. (2009) [225]. As the source is highly variable in X-rays, we choose one observation when the source was in the *hard state* that is similar to *LHS* of other GBH sources. *RXTE* observed the source in the energy range of $3 - 30$ keV on 22^{th} October, 1997 and object was in so-called χ-class [226, 227]. For this observation, the disc luminosity corresponding to the X-ray flux of $F_x^{LHS} = 20.33 \times 10^{-9}$ ergs cm^{-2} s^{-1} (see Table 1) is obtained as 1.79×10^{38} ergs s^{-1} which provides the disc accretion rate as $\dot{M}_{\rm in}^{LHS} = 0.373\dot{M}_{\rm Edd}$. According to our model, the mass outflow rate for *LHS* (or simply hard state for this source) is calculated as $R_{\dot{m}} = 9.98\%$ where, $x_s = 50.47r_g$ with $a_k = 0.98$, $\mathcal{E} = 0.00276$ and $\lambda = 2.679$. Here, we cross the upper limit of a_k (indicated by dagger (†) in column 4 of Table 2.1) as the adopted black hole potential satisfactorily describes the space-time geometry for $a_k \lesssim 0.8$. However, we anticipate that the obtained $R_{\dot{m}}$ provides qualitative estimate that would not differ significantly from its exact value. Using these values, the jet kinetic power is found to be $L_{\rm jet}^{LHS} = 5.99 \times 10^{37}$ ergs s^{-1}.

In this Section, we calculated the jet kinetic power mostly for outbursting GBH sources (except GRS 1915+105) for different accretion states (i.e., *LHS* and *HIMS*). Our findings clearly show that as the sources transit from *LHS* to *HIMS*, there is significant increase in the jet kinetic power. The predicted jet kinetic powers are in close agreement with the observed values for XTE J1859+226, GRO J1655-40, GX 339-4, GRS 1915+105 and H 1743-322 [60, 65, 177].

2.4.2 Jet kinetic power estimated from Accretion Rates

We further extend our study to estimate the jet kinetic power for other GBH and AGN sources where we do not observe fast ($\sim$ day scale) state transitions similar to outbursting GBH sources (except XTE J1550-564). In order to calculate the jet kinetic power for these sources, we find their mass ($M_{\rm BH}$), accretion rate ($\dot{M}_{\rm acc}$) and spin (a_k) from the existing literature. Meanwhile, we compute $R_{\dot{m}}^{\rm max}$ corresponding to black hole spin a_k using our theoretical approach. We then use the values of $\dot{M}_{\rm acc}$ and $R_{\dot{m}}^{\rm max}$ in Eq. 2.21 to estimate the jet kinetic power.

In Table 2.2, we display the physical parameters of the sources (GBHs and AGNs) under consideration along with the computed jet kinetic power obtained from our analysis. In column 1-4, we present the list of sources, their mass ($M_{\rm BH}$), accretion rate ($\dot{M}_{\rm in}$) and spin (a_k). In column 5-6, we mention the representative values of energy $\mathcal{E}$, angular momentum λ of the inflow that provide the shock location x_s (in

column 7) and the corresponding *maximum mass outflow rate* $R_{\dot{m}}^{\rm max}$ (in column 8). Finally, in column 9, we present the maximum jet kinetic power $L_{\rm jet}^{\rm max}$. The first seven sources are GBHs whereas the last three sources are AGNs. Here, we give emphasis on the maximum $R_{\dot{m}}$ in order to speculate the upper limit of jet kinetic power. We find that the estimated jet kinetic powers are in close agreement with the observed values at least for few sources, namely Cyg X-1, XTE J1550-564 and Sgr A* [65, 201, 202]. For remaining sources, we argue that the present method illustrates the typical estimates of jet kinetic power that possibly lie within the acceptable range. Further, in our analysis, we choose four sources having black hole spin $a_k > 0.8$ which are indicated by dagger (†) in column 4. As before, we anticipate that the obtained $L_{\rm jet}^{\rm max}$ for these sources provide qualitative estimates that would not differ significantly from their observed values.

2.5 Chapter Conclusion

In this chapter, we self-consistently examine the accretion-ejection mechanism around the rotating black holes. We find that mass loss can occur for prograde as well as retrograde flows. When the outflow emerges out from the inner part of the disk (PSC), post-shock pressure is decreased that essentially compels the shock front to move forward towards the horizon in order to maintain the pressure balance across the shock. Therefore, a flow originally containing shock wave close to its minimum location ($x_s^{\rm min}$) for $R_{\dot{m}} = 0$, will not provide any outflow as R-H shock conditions are not favorable there (see Fig. 2.3). This certainly tells us that the outflow solutions would be restricted compared to the global shocked accretion solutions in absence of mass loss. However, we show that the shock induced global inflow-outflow solutions are not isolated solutions, but exist for a wide range of inflow parameters, namely, $\mathcal{E}$ and λ, respectively. Interestingly, numerical simulations also indicate the similar findings as reported by Das et al. (2014) [125]. We examine the existence of such solutions with and without outflow and obtain the parameter space spanned by the $\mathcal{E}$ and λ as function of black hole rotation parameter a_k. As anticipated above, the parameter space that provides mass outflow is shrunk compared to the case of no outflow (see Fig. 2.6). In other words, a significant region of the parameter space that exhibits stationary shock for $R_{\dot{m}} = 0$ does not provide steady shock solutions in presence of outflow. This possibly infer that the accreting matter having $\mathcal{E}$ and λ from this region of the parameter space may demonstrate the non-steady behavior [167, 170] which is triggered simply due to the presence of mass loss. Investigation

of such scenario requires time-dependent calculations which is beyond the scope of the present work and we wish to report this elsewhere.

In this work, we mainly focused on thermally ultra-relativistic flows with adiabatic index $\gamma = 4/3$. However, when the cooling effects are negligible, the purely non-relativistic flow behaves like gas-pressure dominated with $\gamma \sim 5/3$. In reality, the value of γ would be an intermediate value depending on the dissipation processes active in the flow. Keeping this in mind, we calculate the parameter space for different values of γ and find that shock forms in all the cases even in presence of outflow. Interestingly, we observe that the effective region of the parameter space is reduced with the increase of γ indicating the limited possibility of shock transition when the flow changes its character towards the non-relativistic regime.

We have estimated the mass outflow rate using the inflow parameters, such as, $\mathcal{E}$ and λ. We show that $R_{\dot{m}}$ increases with a_k for a fixed $\mathcal{E}$ and λ (see Fig. 2.4). This is possibly due to the fact that as a_k is increased shock forms away from the black hole. Therefore, the effective area of the post-shock flow (PSC), where the inflowing matter deflects to generate outflow, becomes large and results enhanced outflow rate. Further, we attempt to find the maximum mass loss ($R_{\dot{m}}^{\rm max}$) from the disc and quantify it in terms of the inflow parameters. For this, we fix the value of γ and explore all possible combinations of energy and angular momentum to obtain $R_{\dot{m}}^{\rm max}$. In Fig. 2.8, we show the variation of $R_{\dot{m}}^{\rm max}$ with a_k and observe that flow with $\gamma = 4/3$ exhibits the highest outflow rate $R_{\dot{m}}^{\rm max}$ that lies in the range around $\sim 17\% - 18\%$. Also, very weak correlation is seen between $R_{\dot{m}}^{\rm max}$ and a_k in all the cases. Moreover, we have shown in Fig. 2.9 that for various sets of $(\mathcal{E}, \lambda)$, $R_{\dot{m}}$ increases with the decrease of x_s (equivalently jet power increases as the size of the PSC is reduced) based on the realistic scenario (i.e., spectral states transit from *LHS* to *HIMS*) which seems to be a common characteristic observed in GBH sources.

We employ our formalism in order to estimate the jet kinetic power ($L_{\rm jet}$) of several black hole sources (GBHs and AGNs). To begin with, we consider outbursting sources to calculate $L_{\rm jet}$ based on the accretion states. For these sources, we compute their *unabsorbed* X-ray fluxes in *LHS* and *HIMS* using the data of *RXTE* observation and obtain their disc rate considering the accretion efficiency $\eta = 0.3$ which seems to be relevant for rotating black holes. Then, we calculate the outflow rate using our formalism and employ it in Eq. 2.21 along with the disc rate to obtain $L_{\rm jet}$. While estimating the jet kinetic power, we consider maximum outflow rate $R_{\dot{m}}^{\rm max}$ for *HIMS* (see Fig. 2.8) and $R_{\dot{m}} \sim 10\%$ for *LHS*, as discussed in Section 5. In Table 2.1, we summarize the physical parameters of five black hole sources

along with the computed jet kinetic power. In the process of estimating $L_{\rm jet}^{\rm max}$, two quantities play a major role. First one is the unabsorbed X-ray flux computed from *RXTE* archival data and the other is the maximum outflow rate obtained from our model calculation. We find that the estimated $L_{\rm jet}^{\rm max}$ for various sources are in close agreement with the observed values [60, 65]. We further extend our study for other black hole sources where the fast accretion state transitions ($\sim$ day scale) are not seen (except XTE J1550-564). For these sources, the disc rate is obtained from the existing literature (see Table 2.2) and $R_{\rm in}^{\rm max}$ is computed from our theoretical calculation which finally provides the $L_{\rm jet}^{\rm max}$. We present these results in Table 2.2. We notice that estimated $L_{\rm jet}^{\rm max}$ for Cyg X-1, XTE J1550-564, M87 and Sgr A* are also in close agreement with the observed values [65, 201, 202]. Following this findings, we argue that $L_{\rm jet}^{\rm max}$ for rest of the sources would also in turn render the representative values which are expected to be consistent with their actual estimates.

Chapter 3

Mass-loss from dissipative accretion disc around rotating black holes

In the previous chapter (Chapter 2), we self-consistently calculated mass outflow rates for a inviscid accretion flow around rotating black hole. The assumption of inviscid accretion flow is only valid when the infall time scale is much larger than the viscous time scale. However, in reality, for a differentially rotating matter, it is not always appropriate to ignore the viscous dissipation straightaway in the accretion flow. Moreover, accretion flow is expected to suffer radiative cooling as it accretes towards the black hole. Thus, in this chapter, we consider a dissipative accretion flows including viscosity and parametric cooling and investigate how the properties of the accretion as well as the outflow solutions depend on the black hole spin and the dissipation parameters which is the main purpose of this chapter.

3.1 Model Equations and Assumptions

In this chapter, we consider a disc-jet system around a rotating black hole where accretion disc lies along the black hole equatorial plane and the jet geometry is considered in the off-equatorial plane about the black hole rotation axis [154, 228, see Fig. 3.1]. Further, in the steady state, the disc is assumed to be thin, low angular momentum, axisymmetric and viscous. To avoid the complexity of full

The contents of this chapter is published in Aktar R., Das S., Nandi A., H Sreehari., MNRAS **471**, 4806 (2017)

and in Aktar R., Das S., Nandi A., H Sreehari., Journal of Astrophysics and Astronomy **39**, 17 (2018)

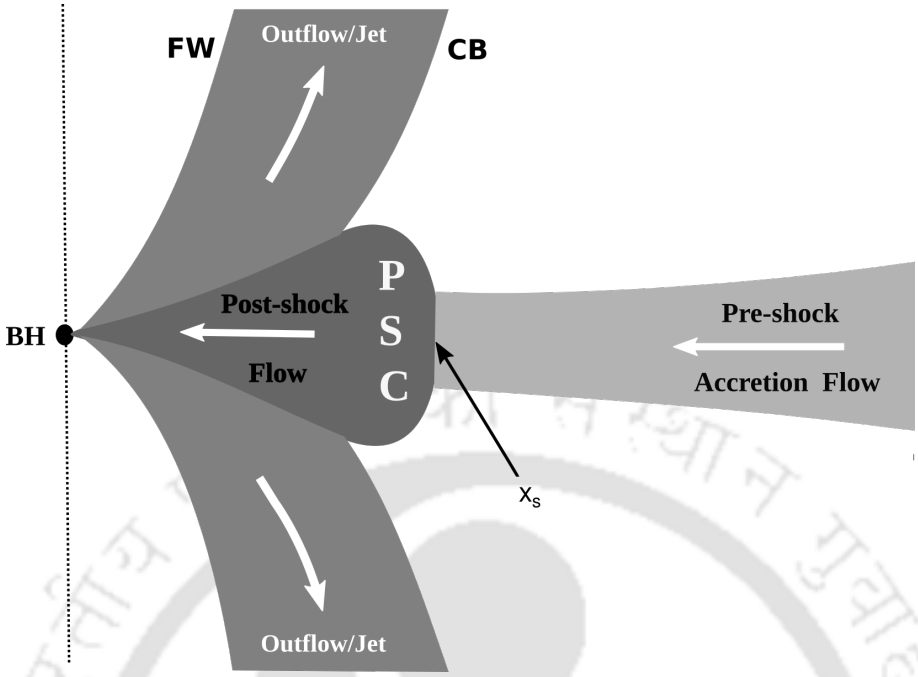

Figure 3.1: Schematic diagram of disc-jet geometry is shown. Accretion flow, post-shock corona (PSC) and outflow are depicted in the figure. Also, we show the shock location (x_s), centrifugal barrier (CB) and funnel wall (FW). Here, the central black hole is indicated as BH. See text for details.

general relativistic calculation, we adopt the pseudo-Kerr potential [146] approach to mimic the space-time geometry around a rotating black hole.

3.1.1 Governing Equations for Accretion

The governing equations that describe the motion for accreting matter are given by,

(i) The radial momentum equation:

$$v\frac{dv}{dx} + \frac{1}{\rho}\frac{dP}{dx} + \frac{d\Phi_{\rm eff}}{dx} = 0, \tag{3.1}$$

where v, P and ρ represent the radial velocity, gas pressure and density of the accretion flow, respectively. Here, $\Phi_{\rm eff}$ denotes the pseudo-Kerr effective potential proposed by Chakrabarti & Mondal (2006) [146]. The explicit expression of $\Phi_{\rm eff}$ is given in Chapter 1 (see Eq. 2.2) that satisfactorily describes the Kerr geometry for $a_k \leq 0.8$.

(ii) The mass conservation equation:

$$\dot{M} = 4\pi\rho v x h, \tag{3.2}$$

where $\dot{M}$ denotes the mass accretion rate which is constant everywhere except the region of mass loss and 4π is the geometric constant. Considering the hydrostatic equilibrium in the vertical direction, the half-thickness of the disc $h(x)$ is obtained as,

$$h(x) = a\sqrt{\frac{x}{\gamma\Phi'_r}}, \tag{3.3}$$

where a is the adiabatic sound speed defined as $a = \sqrt{\frac{\gamma P}{\rho}}$ and γ is the adiabatic index. Here, $\Phi'_r = \left(\frac{\partial\Phi_{\rm eff}}{\partial r}\right)_{z<<x}$, and z is the vertical height in the cylindrical coordinate system where $r = \sqrt{x^2+z^2}$ [229].

(iii) The angular momentum distribution equation:

$$v\frac{d\lambda}{dx} + \frac{1}{\Sigma x}\frac{d}{dx}(x^2 W_{x\phi}) = 0. \tag{3.4}$$

Here, we assume that the viscous stress is dominated by the $x\phi$ component of the stress tensor and is denoted by $W_{x\phi}$. In this work, we consider the viscous stress given by [230],

$$W^{(1)}_{x\phi} = -\alpha(W + \Sigma v^2), \tag{3.5}$$

where $W = 2I_{n+1}Ph(x)$ and $\Sigma = 2I_n\rho h(x)$ are the vertically integrated pressure and density, respectively [231] and α refers the viscosity parameter. When radial velocity of the inflowing matter is insignificant as in the case of Keplerian disc, Eq. 3.5 reduces to the seminal viscosity prescription of Shakura & Sunyaev (1973) [10]. It is noteworthy that an alternative expression of the viscous shear stress is also often considered while modeling the accretion flow around black hole [230, and reference therein] and it is given by,

$$W^{(2)}_{x\phi} = \eta x\frac{d\Omega}{dx}, \tag{3.6}$$

where $\Omega(x)$ is the angular velocity of the accreting matter.

And finally,

(iv) The entropy generation equation:

$$\Sigma v T \frac{ds}{dx} = Q^+ - Q^- = f Q^+; \quad f = 1 - \frac{Q^-}{Q^+}, \tag{3.7}$$

where T and s are the temperature and entropy density of the accretion flow, respectively. Here, Q^+ and Q^- denote the heat gain and lost by the flow. For simplicity, in this work, we introduce a parametric cooling factor f following the work of Narayan & Yi (1994) [20], where the value of f lies in the range $0 \leq f \leq 1$. When $f = 1$, accretion flow behaves like advection dominated whereas for $f = 0$, flow becomes cooling dominated.

After some simple algebra, Eq. 3.7 yields as,

$$\frac{v}{\gamma - 1}\left[\frac{1}{\rho}\frac{dP}{dx} - \frac{\gamma P}{\rho^2}\frac{d\rho}{dx}\right] = -\frac{f Q^+}{\rho h} = -H. \tag{3.8}$$

where we define $H = \frac{fQ^+}{\rho h}$. Due to viscous shear, accreting matter is heated up and we compute the heating of the flow as $Q^+ = W_{x\phi}^2/\eta$, where η represents the dynamical viscosity coefficient. While calculating Q^+, when $W_{x\phi}^{(1)}$ is used, the contribution of viscous shear is being sacrificed. On the other hand, when $W_{x\phi}^{(2)}$ is used, second order derivative of Ω appears in the sonic point analysis and equations become difficult to solve. To avoid such limitations, however, retaining the memory of $d\Omega/dx$ intact, we adopt the mixed shear stress prescription [230] where the combination of both shear stresses are considered. Following this, the heating term Q^+ is yielded as,

$$Q^+ = \frac{W_{x\phi}^{(1)} W_{x\phi}^{(2)}}{\eta} = -\alpha(W + \Sigma v^2)\left(x\frac{d\Omega}{dx}\right). \tag{3.9}$$

Using Eq. 3.9, we obtain the simplified expression of H as,

$$H = \frac{fQ^+}{\rho h} = fA(ga^2 + \gamma v^2)\left(x\frac{d\Omega}{dx}\right), \tag{3.10}$$

where $A = -2\alpha I_n/\gamma$ and $g = I_{n+1}/I_n$. Here, $n = (\gamma - 1)^{-1}$ is the polytropic index. I_n and I_{n+1} are the constant factors arising while carrying out the vertical integration of density and pressure at a given radial coordinate x (see [231]).

3.1.2 Sonic point conditions

In the accretion process around black hole, radial velocity of the inflowing matter at the outer edge remains negligibly small although matter enters into the black hole with radial velocity equal to the speed of light. Therefore, the velocity of the inflowing matter is likely to match with the sound speed at some point where flow changes its sonic character from subsonic to supersonic state. Such a point is called as sonic point. Depending on the initial parameters, flow may contain more than one sonic points. Flow containing multiple sonic points is of our interest as it may possess stationary shock when the shock conditions are satisfied. In order to investigate the properties of the shock wave and its implication for black hole accretion, study of sonic point properties is therefore essential. Accordingly, we carry out sonic point analysis following Chakrabarti (1989) [38] and obtain the first order linear differential equation using Eqs. 3.1, 3.2, 3.4 and 3.8 as,

$$\frac{dv}{dx} = \frac{N}{D}, \tag{3.11}$$

where

$$\begin{aligned} N = &-\frac{fA\alpha(ga^2+\gamma v^2)^2}{\gamma v x} - \frac{3a^2 v}{(\gamma-1)x} + \frac{a^2 v}{(\gamma-1)}\left(\frac{d\ln\Phi'_r}{dx}\right) \\ &+ \left[\frac{2fA\alpha g(ga^2+\gamma v^2)}{v} + \frac{(\gamma+1)v}{(\gamma-1)}\right]\left(\frac{d\Phi_{\rm eff}}{dx}\right) - \frac{3fA\alpha g a^2(ga^2+\gamma v^2)}{\gamma v x} \\ &+ \frac{fA\alpha g a^2(ga^2+\gamma v^2)}{\gamma v}\left(\frac{d\ln\Phi'_r}{dx}\right) + \frac{2fA\lambda(ga^2+\gamma v^2)}{x^2}, \end{aligned} \tag{3.12}$$

and

$$D = \frac{2a^2}{(\gamma-1)} - \frac{(\gamma+1)v^2}{(\gamma-1)} - fA\alpha(ga^2+\gamma v^2)\left[(2g-1) - \frac{ga^2}{\gamma v^2}\right]. \tag{3.13}$$

We calculate the differential form of angular momentum using the expression of Eq. 3.4 as,

$$\frac{d\lambda}{dx} = \frac{\alpha}{\gamma v}(ga^2+\gamma v^2) + \frac{2\alpha x g a}{\gamma v}\left(\frac{da}{dx}\right) + \alpha x\left(1-\frac{ga^2}{\gamma v^2}\right)\left(\frac{dv}{dx}\right). \tag{3.14}$$

We calculate the gradient of sound speed using Eqs. (3.1 - 3.3) as,

$$\frac{da}{dx} = \left(\frac{a}{v} - \frac{\gamma v}{a}\right)\frac{dv}{dx} + \frac{3a}{2x} - \frac{a}{2}\left(\frac{d\ln\Phi'_r}{dx}\right) - \frac{\gamma}{a}\left(\frac{d\Phi_{\rm eff}}{dx}\right). \tag{3.15}$$

The inner boundary condition of black hole demands that the flow should be smooth everywhere between the outer edge and the horizon. Therefore, the radial velocity gradient must be finite everywhere. To maintain this, at the sonic point, both numerator N and denominator D of Eq. 3.11 must vanish simultaneously [38]. Setting $D = 0$, we obtain the Mach number ($M = v/a$) expression at the sonic point as,

$$M_c^2 = \frac{-m_b - \sqrt{m_b^2 - 4m_a m_c}}{2m_a}, \tag{3.16}$$

where

$$\begin{aligned} m_a =& - fA\alpha\gamma^2(\gamma-1)(2g-1) - \gamma(\gamma+1), \\ m_b =& 2\gamma - 2fA\alpha g\gamma(\gamma-1)(g-1), \\ m_c =& fA\alpha g^2(\gamma-1). \end{aligned}$$

The sound speed at the sonic point is found out by setting numerator $N = 0$ and is given by,

$$a(x_c) = \frac{-a_2 - \sqrt{a_2^2 - 4a_1 a_3}}{2a_1}, \tag{3.17}$$

where

$$\begin{aligned} a_1 =& -\frac{fA\alpha(g+\gamma M_c^2)^2}{\gamma x} - \frac{3M_c^2}{(\gamma-1)x} + \frac{M_c^2}{(\gamma-1)}\left(\frac{d\ln\Phi_r'}{dx}\right) - \frac{3fA\alpha g(g+\gamma M_c^2)}{\gamma x} \\ &+ \frac{fA\alpha g(g+\gamma M_c^2)}{\gamma}\left(\frac{d\ln\Phi_r'}{dx}\right), \\ a_2 =& \frac{2fA\lambda M_c(g+\gamma M_c^2)}{x^2}, \\ a_3 =& \left[2fA\alpha g(g+\gamma M_c^2) + \frac{(\gamma+1)M_c^2}{(\gamma-1)}\right]\left(\frac{d\Phi_{\rm eff}}{dx}\right). \end{aligned}$$

Here, M_c represents the Mach number at the sonic point (x_c).

3.1.3 Equations for Outflow

In this work, we consider that the accretion flow geometry is resided around the equatorial plane and the jet or outflow geometry is described in the off-equatorial

plane about the axis of rotation of the black hole [43, 122]. As the jets are tenuous in nature, the differential rotation of the outflowing matter is expected to be negligibly small and thus, we ignore the viscosity while describing outflow. Further, the outflowing matter is considered to obey the polytropic equation of state as $P_j = K_j \rho_j^{\gamma}$, where, the suffix '$j$' denotes the outflow variables and K_j denotes the measure of specific entropy of the jet. Subsequently, the equations of motion of the outflowing matter are given by,

(i) The energy conservation equation of outflow:

$$\mathcal{E}_j = \frac{1}{2} v_j^2 + \frac{a_j^2}{\gamma - 1} + \Phi_{\rm eff}, \tag{3.18}$$

where $\mathcal{E}_j$ represents the specific energy of the outflow, v_j is the outflow velocity and a_j is the sound speed of the outflow, respectively.

(ii) the mass conservation equation of outflow:

$$\dot{M}_{\rm out} = \rho_j v_j \mathcal{A}_j, \tag{3.19}$$

where $\dot{M}_{\rm out}$ represents the outflowing mass rate and $\mathcal{A}_j$ refers to the area function of the jet. We estimate $\mathcal{A}_j$ by using the radius of two boundary surfaces, namely the centrifugal barrier (CB) and the funnel wall (FW) [122] (see Fig. 3.1). The centrifugal barrier (CB) is obtained by defining the pressure maxima surface as $(d\Phi_{\rm eff}/dx)_{r_{\rm CB}} = 0$ and the funnel wall (FW) stands for the pressure minimum surface which is defined by the null effective potential as $\Phi_{\rm eff}|_{r_{\rm FW}} = 0$ [122]. In general, the jet streamlines within the jet geometry are not exactly parallel to the jet area vector and therefore, in order to calculate the jet area function, we introduce a geometric factor corresponding to the projection of the jet streamlines on the jet cross-section. Accordingly, the jet area function is obtained as [45],

$$\mathcal{A}_j = \frac{2\pi(x_{\rm CB}^2 - x_{\rm FW}^2)}{\sqrt{1 + (dx_j/dy_j)^2}}, \tag{3.20}$$

where $\sqrt{1 + (dx_j/dy_j)^2}$ is projection factor of the jet area. Here, $x_{\rm CB}$ and $x_{\rm FW}$ refer to the radius of the centrifugal barrier and funnel wall in the cylindrical coordinate system, respectively. The corresponding spherical radius of the jet is given by $r_j = \sqrt{x_j^2 + y_j^2}$. With this consideration, we carry out the sonic point analysis for outflows following Das & Chattopadhyay (2008) [44]. Subsequently, we use the jet sonic point properties while obtaining the outflow solution.

3.2 Solution methodology

In the accretion process, rotating matter experiences centrifugal repulsion while falling inward that eventually causes a virtual barrier around the black hole. Depending on the initial parameters, such a centrifugal barrier can trigger discontinuous transition in the flow variables in the form of shock. Because of shock compression, since the post-shock flow (*i.e.*, PSC) becomes hot and dense, excess thermal gradient force at PSC is developed that deflects a part of the infalling matter along the black hole rotation axis in the form of outflows/jets. In the present analysis, we consider the outflowing matter to be emerged out between the centrifugal barrier (CB) and funnel wall (FW) surfaces. Following the above consideration, we move forward to obtain the self-consistent accretion-ejection solutions that are coupled via Rankine-Hugoniot shock conditions described in Chapter 2.

In our disc-jet model, outflow is considered to be originated from the post shock region and accordingly, we assume that the outflow is essentially launched with the same density as in the PSC *i.e.*, $\rho_j = \rho_+$. Using Eqs. 3.2, 3.19 and 2.13, the mass outflow rate is then computed as,

$$R_{\dot{m}} = \frac{\dot{M}_{\rm out}}{\dot{M}_-} = \frac{R v_j(x_s)\mathcal{A}_j(x_s)}{4\pi\sqrt{\frac{1}{\gamma}}x_s^{3/2}{\Phi'_r}^{-1/2}a_+ v_-}, \tag{3.21}$$

where R is the compression ratio defined as $R = \Sigma_+/\Sigma_-$. In addition, $v_j(x_s)$ and $\mathcal{A}_j(x_s)$ are the jet velocity and the jet area function calculated at the shock, respectively. Here, we employ the successive iteration method to calculate $R_{\dot{m}}$ self-consistently. In this method, initially we start with $R_{\dot{m}} = 0$. Using RH shock conditions, we calculate the virtual shock location x_s^v for a given set of inflow variables, namely $(\mathcal{E}_{\rm inj}, \lambda_{\rm inj}, a_k, \alpha, f)$. Subsequently, we use $\mathcal{E}_j = \mathcal{E}_+$ and $\lambda_j = \lambda_+$ to calculate the jet sonic point using Eqs. 3.18 and 3.19. Starting form the jet sonic point, we integrate the jet equations towards the black hole horizon in order to calculate the jet variables and continue to do so up to the jet base which is equivalently the shock location. Utilizing these jet variables, we compute the virtual $R_{\dot{m}}^v$ which we use further in the RH shock conditions to get a new shock location. We continue the iteration process until the shock location converges to the actual location at x_s and finally obtain $R_{\dot{m}}$ corresponding to x_s.

3.3 Results and Discussions

In this section, we present our model solutions for various sets of initial parameters of the accretion flow. In particular, here we depict the effect of dissipation processes, namely viscosity and cooling on the mass loss from the accretion disc around rotating black hole. In the first section, we investigate the effect of viscosity on the outflow rates in the advection-dominated regime (i.e., $f = 1$) and in the next section, we show the effect of cooling on outflow rates in the cooling-dominated regime (i.e., $f \to 0$). As mentioned in §3.1, the pseudo-Kerr potential [146] adopted in this work describes the general relativistic features of space-time geometry quite satisfactorily in the range $-1 \leq a_k \leq 0.8$. However, for the sake of completeness, here we present results beyond $a_k > 0.8$ to examine the overall characteristics of the accretion solution for the maximally rotating black hole. Though it introduces error $\sim 20\%$ as far as marginally stable orbit is concerned for the maximally rotating case [146], we argue that the overall findings of the accretion solutions would not deviate severely. In addition, it is known that the adiabatic index (γ) depends on the ratio of the thermal energy to the rest energy of the flow and the theoretical limit of γ lies in the range $4/3 \leq \gamma \leq 5/3$ [5]. In this chapter, for the purpose of representation, we consider $\gamma = 1.4$ all throughout unless otherwise stated.

3.3.1 Effect of viscosity on outflow rates

In Fig. 3.2, we present the global dissipative viscous accretion solutions around the rotating black holes for various sets of inflow parameters. All these solutions contain shock waves. Here, the flow parameters at the outer edge is chosen as $x_{\rm inj} = 500$, $\lambda_{\rm inj} = 2.656$ and $\mathcal{E}_{\rm inj} = 0.00135$, respectively and the black hole spin is considered as $a_k = 0.76$. In Fig. 3.2a, we show the Mach number ($M = v/a$) variation of the inflowing matter with the radial distance in absence of mass loss. The solid, dashed and dotted curves are for the viscosity parameter $\alpha = 0.0$ (black), $\alpha = 0.003$ (red) and $\alpha = 0.0046$ (blue), respectively. We find that the shock front moves inward towards the black hole horizon with the increase of α. This is simply because the increase of α enhances the angular momentum transport towards the outer edge of the disc that eventually instigates the debilitating of centrifugal barrier around the black hole. Effectively, this compels the shock front to move inward in order to preserve the pressure balance across it. In the figure, vertical arrows indicate the shock transition and the location of the shock are obtained as $x_s = 42.03$, 22.85 and 15.59 for inviscid case, $\alpha = 0.0$, 0.003 and 0.0046, respectively.

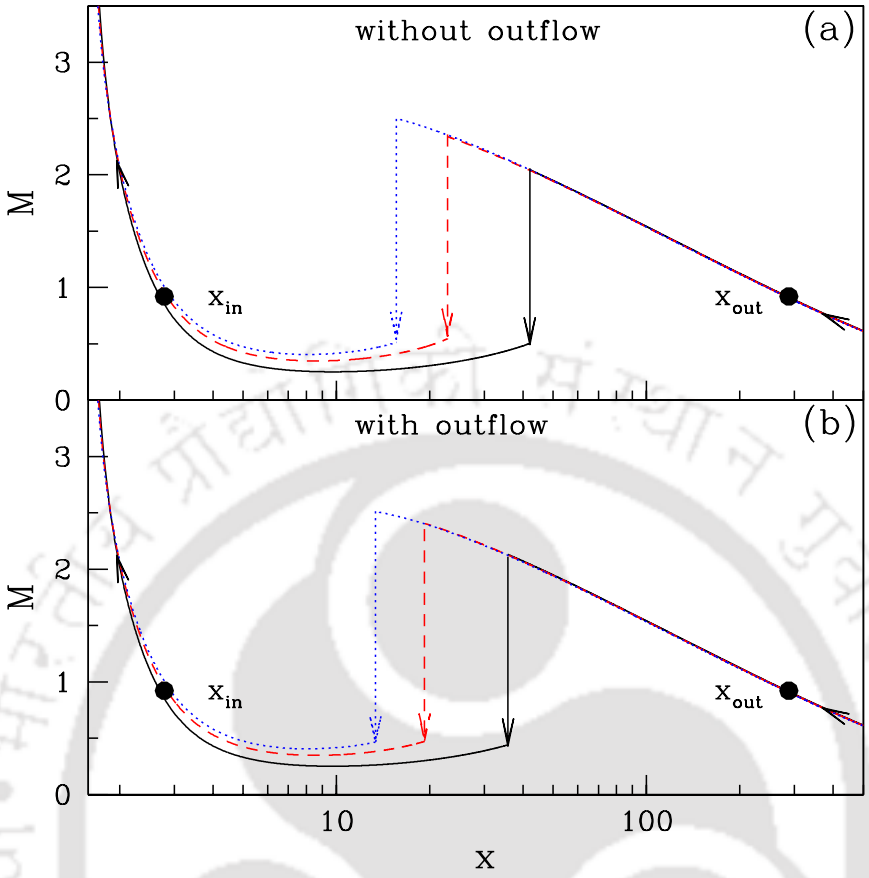

Figure 3.2: Variation of inflow Mach number $M = (v/a)$ with radial distance (x). Solid, dashed and dotted curves are for $\alpha = 0.0$ (black), 0.003 (red) and 0.0046 (blue), respectively. Upper panel is for without outflow and the lower panel is for with outflow. Here, we fix $a_k = 0.76$. See text for details.

In Fig. 3.2b, we display the accretion solution in presence of mass loss for the same set of inflow parameters as in Fig. 3.2a. In the present model, the outflow is launched from the post-shock region. Therefore, when a part of the inflowing matter is emerged out from the disc as outflow, the effective pressure at the inner part of the disc is reduced and eventually the shock front is propelled towards the black hole even further in order to maintain the pressure balance across the shock. The solid, dashed and dotted curves denote the results corresponding to the viscosity parameters, shock locations and outflow rates as, $(\alpha, x_s, R_{\dot{m}}) = (0.0, 35.76, 0.0346)$ (black), $(0.003, 19.24, 0.0220)$ (red) and $(0.0046, 13.36, 0.0182)$ (blue), respectively. In both the panels, filled circles indicate the inner $(x_{\rm in})$ and outer $(x_{\rm out})$ sonic points and arrows represent the flow direction.

In Fig. 3.3, we investigate the effect of viscosity parameter on the inflow-outflow

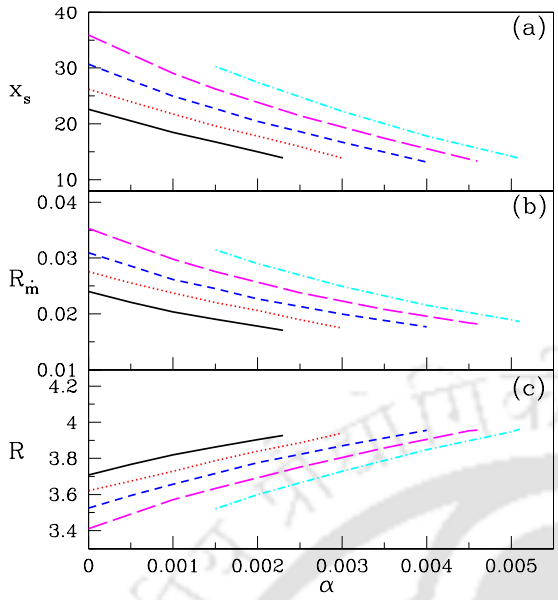

Figure 3.3: Variation of (a) shock location (x_s), (b) outflow rate ($R_{\dot{m}}$) and (c) compression ratio (R) as a function of viscosity parameter α for $a_k = 0.78$ to 0.70, where $\Delta a_k = 0.02$ (right to left). Here, we fix the outer boundary at $x_{\rm inj} = 500$. The angular momentum and energy of the flow at $x_{\rm inj}$ is chosen as $\lambda_{\rm inj} = 2.656$ and $\mathcal{E}_{\rm inj} = 0.00135$, respectively. See text for further details.

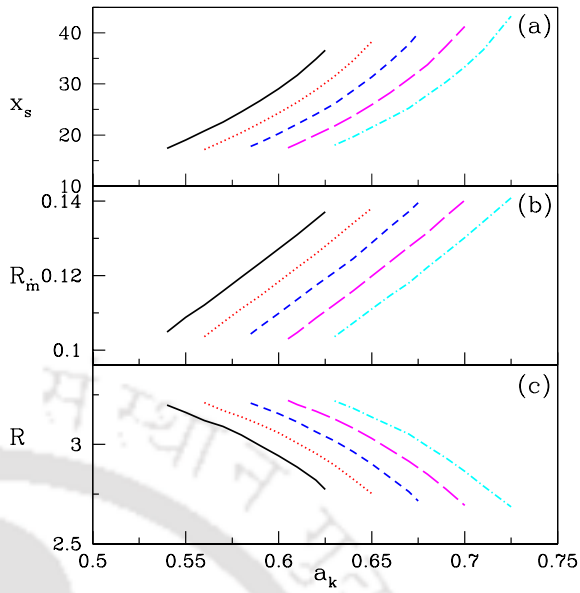

Figure 3.4: Plot of (a) shock location (x_s), (b) outflow rate ($R_{\dot{m}}$) and (c) compression ratio (R) variation as function of spin a_k for $\alpha = 0.003$ to 0.007, where $\Delta\alpha = 0.001$ (left to right). Here, we fix the outer boundary at $x_{\rm inj} = 300$ and choose $\lambda_{\rm inj} = 2.80$ and $\mathcal{E}_{\rm inj} = 0.0025$, respectively. See text for details.

solutions around the rotating black holes. Here, we fix the injection radius of the inflowing matter at $x_{\rm inj} = 500$ and the corresponding inflow energy ($\mathcal{E}_{\rm inj}$) and angular momentum ($\lambda_{\rm inj}$) at $x_{\rm inj}$ are $(\mathcal{E}_{\rm inj}, \lambda_{\rm inj}) = (0.00135, 2.656)$, respectively. We vary the spin of the black hole a_k from 0.78 to 0.7 from the right most (dot-big-dashed) to the left most curves (solid) with an interval $\Delta a_k = 0.02$. In the upper panel (Fig. 3.3a), we show the variation of shock location with the viscosity parameter α in presence of mass loss. As it is seen in Fig. 3.2, here also we find that shock (x_s) proceeds closer to the black hole with the increase of viscosity parameter (α). This clearly indicates that the effective size of the PSC decreases with the increase of α. As a consequence, the fraction of inflowing matter intercepted by the PSC is reduced that eventually produce feeble outflow rate when α is increased. In Fig. 3.3b, we plot the outflow rates ($R_{\dot{m}}$) corresponding to Fig. 3.3a. In Fig. 3.3c, we study the compression ratio (R) of shocked accretion flow in presence of mass loss as function of α. Compression ratio essentially measures the density compression across the shock and is defined as the ratio of post-shock density to the pre-shock density. As

the shock moves closer to the horizon, flow experiences enhanced compression and therefore, R increases with the increase of α.

In Fig. 3.4, we show the effect of black hole rotation on the shock properties and the mass outflow rate. For this analysis, we choose the outer boundary of the disc at $x_{\rm inj} = 300$ with specific energy and angular momentum as $\mathcal{E}_{\rm inj} = 0.0025$ and $\lambda_{\rm inj} = 2.80$, respectively. In the upper (a), middle (b) and bottom (c) panels of Fig. 3.4, we plot shock locations (x_s), outflow rates ($R_{\dot{m}}$) and compression ratio (R) as function of black hole spin (a_k), respectively. In all the panels, we vary the viscosity parameter from $\alpha = 0.003$ to 0.007 with an interval $\Delta\alpha = 0.001$ from left most to the right most curve. We observe that *for fixed outer boundary condition*, the shock location (x_s) moves away from the black hole horizon with the increase of black hole rotation a_k for flows with fixed α. As a result, the effective area of PSC intercepted by the inflowing matter is increased and consequently, the amount of the inflowing matter deflected by the PSC is also increased yielding enhanced mass outflow rates $R_{\dot{m}}$. In contrary, we find that $R_{\dot{m}}$ decreases with the increase of α for fixed a_k as seen in Fig. 3.3. In addition, as x_s recedes away from the black hole horizon with the increase of a_k for flows with constant α, the compression ratio (R) is also decreased as shown in Fig. 3.4c. On the other hand, for fixed a_k, as α increased, both x_s and $R_{\dot{m}}$ decreases whereas R increases. This findings are compatible with results of Aktar et al. (2015) [228].

We proceed further to examine the region of parameter space that permits stationary shock solutions. As it is already pointed out (see Fig. 3.3-3.4) that the shock induced global accretion solutions are not the isolated solutions, instead the solutions of this kind can be obtained for a wide range of inflow parameters. Moreover, in our model, since the outflow is originated from the PSC, it is worthy to identify the shock parameter space in terms of the viscosity parameter (α) and the spin of the black hole (a_k). In Fig. 3.5, we classify the region of the shock parameter space spanned by the angular momentum ($\lambda_{\rm in}$) and energy ($\mathcal{E}_{\rm in}$) of the flow measured at the inner sonic point ($x_{\rm in}$). The results displayed in Fig. 3.5(a-c) are obtained for $a_k = 0.0$ (a), 0.4 (b) and 0.8 (c), respectively. The corresponding viscosity parameters are marked in each panel. The solid curves separate the shock parameter space when mass loss from the disc is ignored whereas the dotted curves represent the shocked parameter space including mass loss. In presence of outflow, the effective area of the PSC becomes smaller (see Fig. 3.2) and therefore, the resulting parameter space is reduced in comparison to the no mass loss case, particularly in the lower angular momentum and higher energy side. When the input parameters are chosen

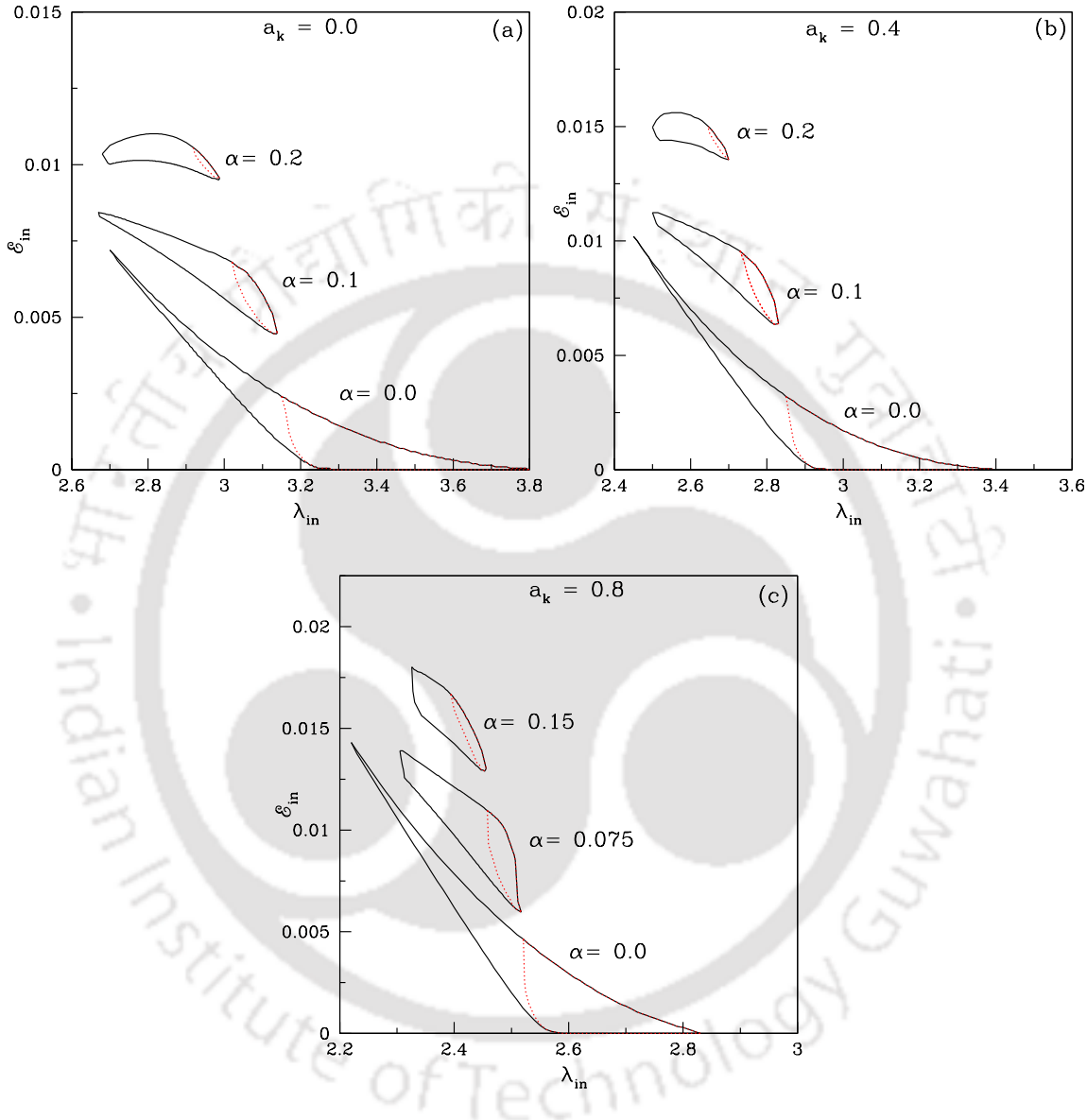

Figure 3.5: Identification of parameter space for shock in $\lambda_{\rm in} - \mathcal{E}_{\rm in}$ plane is shown as function of viscosity parameter (α) for various black hole spin parameter (a_k). Solid curves denote the shock parameter space in absence of mass loss whereas dotted curves separate the shock parameter space in presence of mass loss. Fig. 3.5a, 3.5b and 3.5c illustrate the results for $a_k = 0.0$, 0.4 and 0.8, respectively. See text for further details.

from these parts of the parameter space ignoring outflow, accretion flow encounters shock transition very close to the black hole [42]. After that when outflow is allowed to be launched from the PSC, shock ceases to exist. Subsequently, we study the role of viscosity in classifying the parameter space. In the accretion flow, the presence of viscosity manifests dual effects. Firstly, viscosity transports angular momentum outward reducing its value at the inner edge of the disc and secondly, flow is heated up due to the effect of viscous dissipation. Hence, as the viscosity is increased, the shock parameter space is shrunk from the both ends of the angular momentum range and also shifted towards the higher energy domain. Moreover, with the inclusion of viscosity, flow becomes dissipative and consequently, the possibility of standing shock formation is reduced [170, 232] and finally parameter space for standing shock disappears when the critical viscosity limit is reached. Interestingly, time varying shock solutions may still exist beyond the critical viscosity limit [125, 232]. Numerical simulations already explored these oscillatory behavior of shock solutions [125, 233–235] which successfully describe the Quasi-periodic Oscillations (QPOs) and periodic mass loss phenomena observed in several astrophysical black hole systems [49, 236, 237]. A comprehensive study of time dependent global accretion solution around rotating black hole is considered as a future work as it is beyond the scope of the present work and will be reported elsewhere.

We continue the study of shock properties in terms of the input flow parameters. Towards this, we investigate the maximum value of the viscosity parameters ($\alpha_{\rm no}^{\rm max}$ and $\alpha_{\rm o}^{\rm max}$) that allows steady shock solutions in absence ($R_{\dot{\rm m}} = 0$) as well as in presence ($R_{\dot{\rm m}} \neq 0$) of mass loss. While doing so, we first fix the black hole spin (a_k) and vary the remaining flow parameters freely. In Fig. 3.6, we depict the variation of $\alpha^{\rm max}$ as function of a_k where the upper panel is for without mass loss case and the lower panel is for with mass loss case. We already pointed out that the pseudo-Kerr potential adopted here describes the space time geometry around the black hole satisfactorily for $a_k \leq 0.8$. However, we present results for $a_k > 0.8$ which are depicted with shaded region. Here, we argue that the obtained results demonstrate the overall findings of the accretion solutions at least qualitatively [146]. We find that the upper limit of viscosity parameter $\alpha^{\rm max}$ for shock is anti-correlated with the spin a_k in both the panels. In general, for the lower viscosity parameter, the sub-Keplerian flow joins with the Keplerian disc far away from the black hole horizon. This eventually increases the possibility of possessing multiple sonic points including shock waves. On the other hand, at the high viscosity limit, ($i.e.$, $\alpha > \alpha^{\rm max}$), Keplerian disc comes very close to the black hole horizon allowing the flow to pass

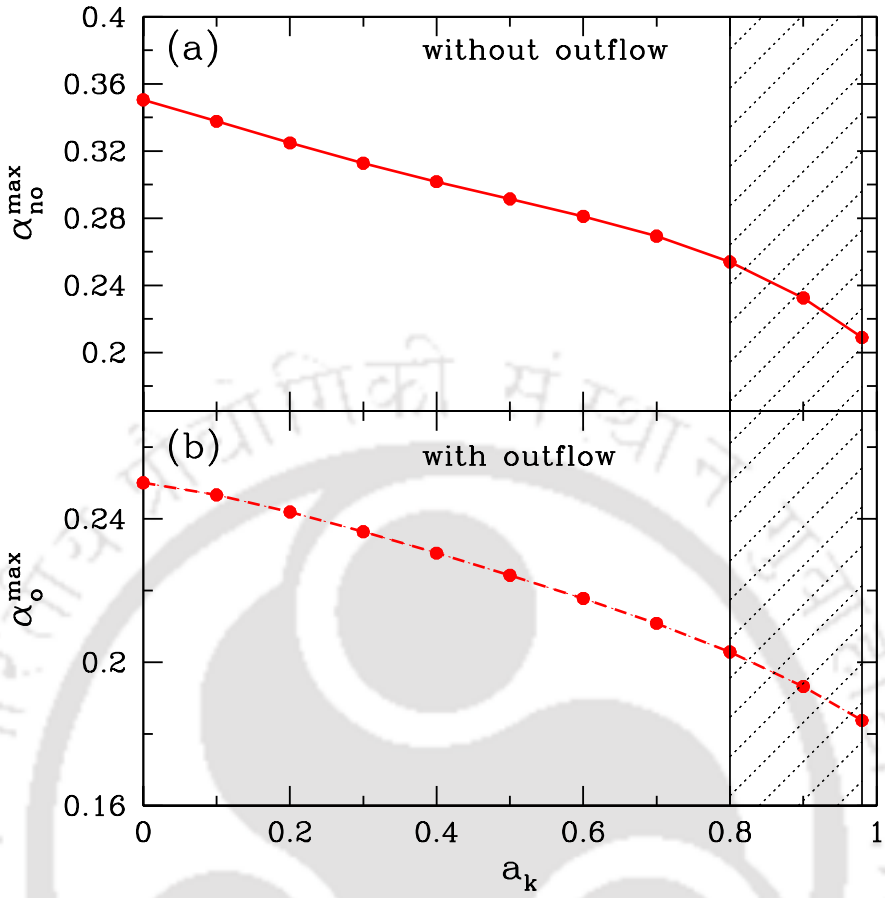

Figure 3.6: Variation of maximum viscosity parameter ($\alpha^{\rm max}$) with spin of the black hole a_k that allows standing shock. In the upper panel (a), filled circles connected with the solid curve denotes $\alpha_{\rm no}^{\rm max}$ in absence of outflow and in the lower panel (b), filled circles joined with the dashed curve represents $\alpha_{\rm o}^{\rm max}$ in presence of outflow. In both the panels, results within the shaded region are obtained for $a_k > 0.8$. See text for further details.

only through the single sonic point [139]. In addition, the rotation of the black hole drags the accreting matter towards the horizon by its strong gravitational pull. Therefore, the possibility of the formation of steady shock in the higher viscosity domain for increasing a_k becomes rarer. It is to be noted that the obtained $\alpha^{\rm max}$ for non-rotating black hole is consistent with the results of Chakrabarti & Das (2004) [232]. When outflow is considered, the possibility of shock formation is decreased (see Fig. 3.5) and therefore, the obtained $\alpha^{\rm max}$ for $R_{\dot{\rm m}} \neq 0$ becomes smaller compared to case with $R_{\dot{\rm m}} = 0$ [45].

In Fig. 3.7, we present the outflow parameter spaces for various α where each panel demonstrates the two dimensional surface projection of the three dimensional plot spanned with $\mathcal{E}_{\rm in}$, $\lambda_{\rm in}$ and $R_{\dot{\rm m}}$, respectively. Here, we choose $a_k = 0.5$ and vary the viscosity parameter as $\alpha = 0.0$ (top-left), 0.05 (top-right), 0.1 (bottom-left) and

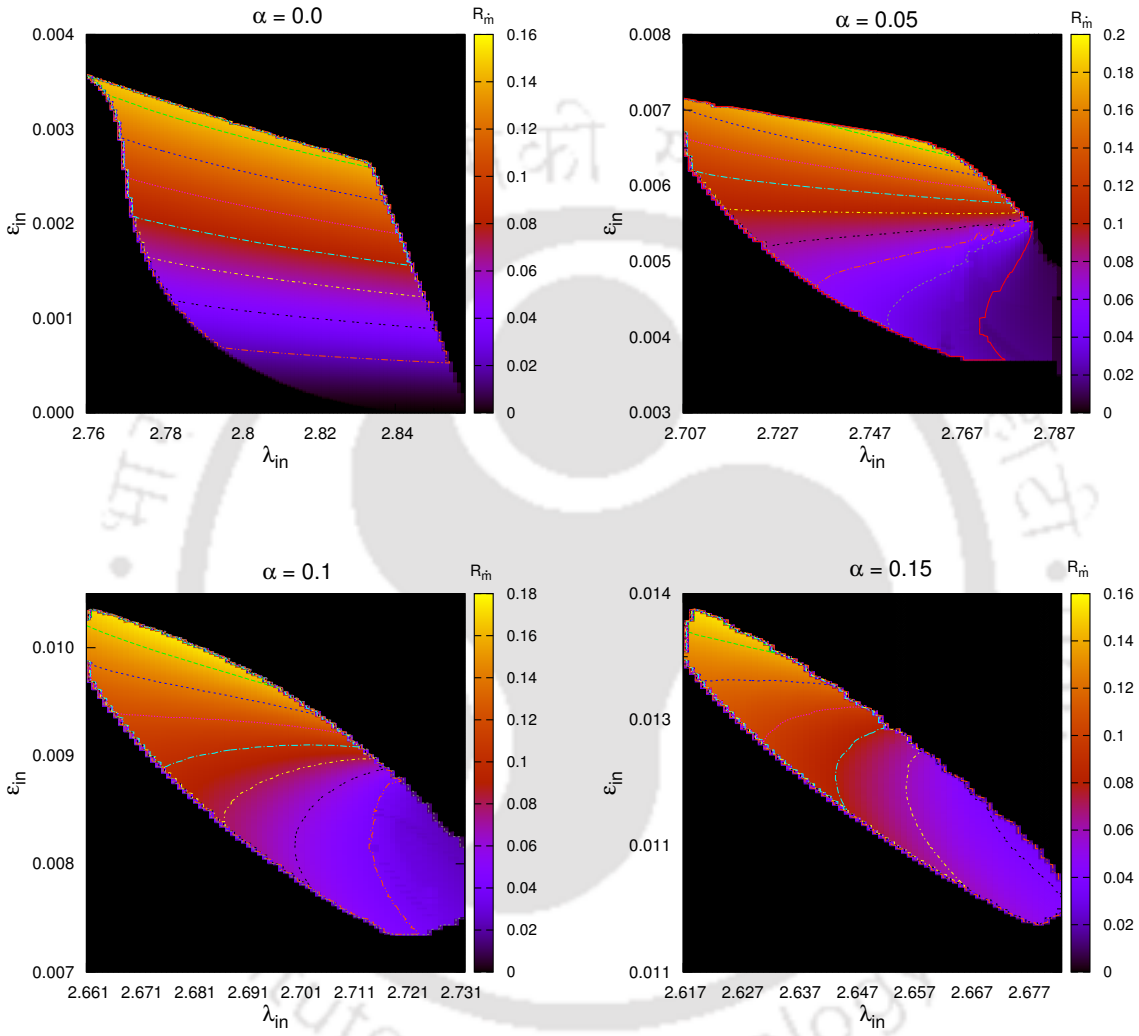

Figure 3.7: Two dimensional (2D) surface projection of three dimensional (3D) plot of flow energy ($\mathcal{E}_{\rm in}$), angular momentum ($\lambda_{\rm in}$) and outflow rates ($R_{\dot{m}}$). In each panel, vertical color coded bar represents the estimated range of outflow rates. Here, the viscosity parameters are chosen as $\alpha = 0.0$, 0.05, 0.1 and 0.15, respectively and we fix black hole spin as $a_k = 0.5$. See text for details.

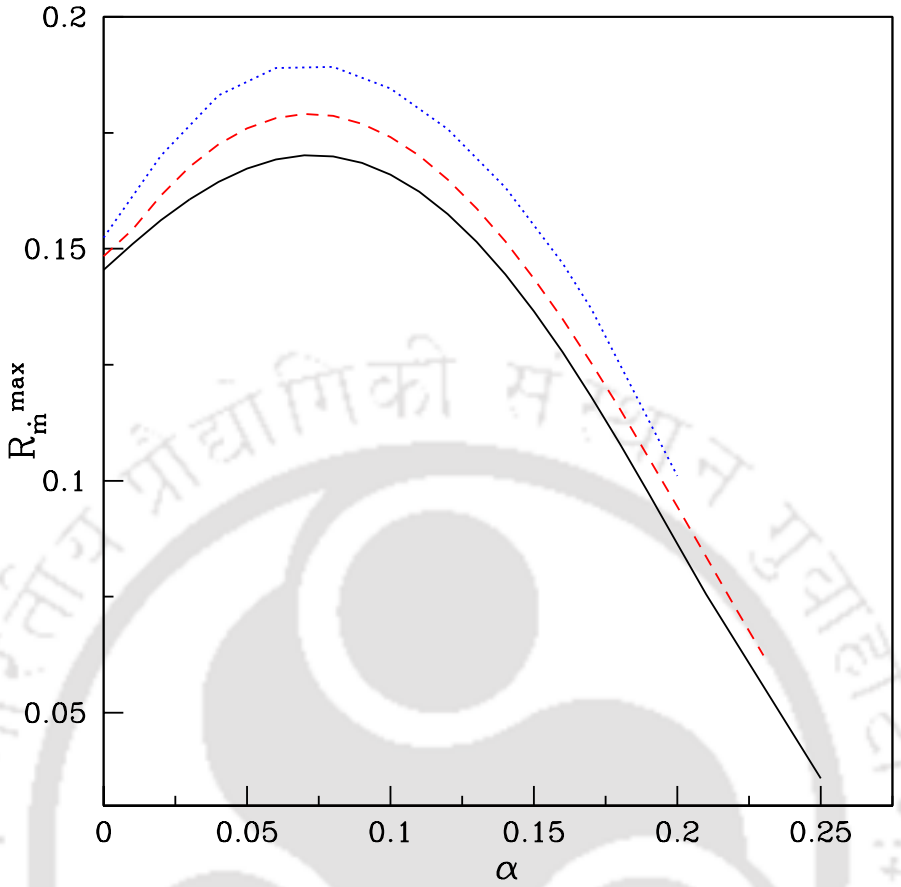

Figure 3.8: General behaviour of maximum outflow rates $R_{\dot{m}}^{\max}$ as function of viscosity parameter α. Solid, dashed and dotted curves are for $a_k = 0.0$ (black), 0.4 (red) and 0.8 (blue), respectively. See text for details.

0.15 (bottom-right). In each panel, the color-coded bar represents the range of $R_{\rm in}$ which is obtained from our model calculation. Moreover, the color coded contours are drawn with an interval of $\Delta R_{\rm in} = 0.02$ starting from $R_{\rm in}^{\max}$ up to its minimum value. In other words, the different colors embedded with color coded contours illustrate the overall span of 2% outflow rate altogether. In addition, we find that the effective bounded region of the outflow parameter space gradually shrinks with the increase of the viscosity parameter α as is seen in Fig. 3.5. It is to be noted that in order to obtain the maximum outflow rate ($R_{\rm in}^{\max}$), the inflow parameters must lie in the higher $\mathcal{E}_{\rm in}$ and lower $\lambda_{\rm in}$ domains irrespective to the value of the viscosity parameter α.

In the course of our study, we put an effort to compute the maximum outflow rate ($R_{\rm in}^{\max}$) that is being originated from the disc. While doing so, for a given a_k, we calculate $R_{\dot{m}}^{\max}$ in terms of viscosity parameter (α) by varying the remaining inflow

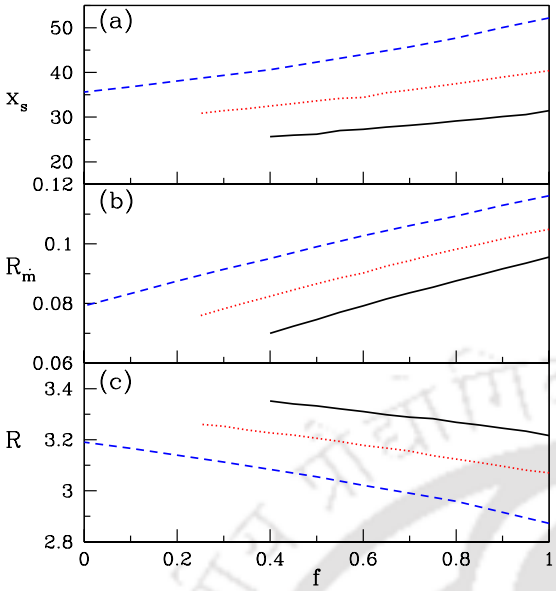

Figure 3.9: Plot of shock locations (x_s) (upper panel), outflow rates ($R_{\dot{m}}$) (middle panel) and compression ratio (R) (lower panel) as function of the cooling factor f. Solid, dotted and dashed curves denote the results for $\lambda_{\rm inj} = 3.975$ (black), 4.0 (red) and 4.025 (blue), respectively. Here, we fix the outer boundary at $x_{\rm inj} = 500$ and flow energy as $\mathcal{E}_{\rm inj} = 0.0015$. The viscosity parameter and spin values are chosen as $\alpha = 0.05$ and $a_k = 0.5$, respectively.

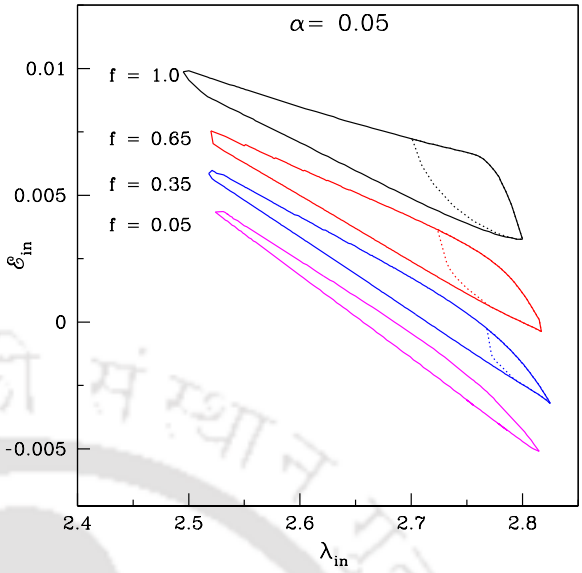

Figure 3.10: Comparision of shock parameter spaces obtained for various cooling parameters. Region bounded by the solid curve is for without mass loss case and the region bounded by the dotted curve represents results with mass loss case. Cooling parameters are marked in the figure. Here, we consider $\alpha = 0.05$ and $a_k = 0.5$. See text for details.

parameters independently. The obtained result is depicted in Fig. 3.8 where we show the variation of maximum outflow rates $R_{\dot{m}}^{\rm max}$ with α. In the figure, solid, dashed and dotted curves denote the results corresponding to $a_k = 0.0$ (black), 0.4 (red) and 0.8 (blue), respectively. We find that $R_{\dot{m}}^{\rm max}$ initially increases gradually with α and reaches to its maximum value and finally starts decreasing with the increasing α as shown in the figure. We observe that for a given α, $R_{\dot{m}}^{\rm max}$ weakly correlates with a_k which seems to be consistent with the results of inviscid flow as reported in Aktar et al. (2015) [228]. Overall, we find that the maximum outflow rate typically lies in the range $3\% \lesssim R_{\dot{m}}^{\rm max} \lesssim 19\%$ for wide range of viscosity parameter (α).

3.3.2 Effect of cooling on outflow rates

Until now, we present all the result in the advection dominated regime i.e., $f = 1$. In this section, we discuss the effect of cooling on outflow rates around rotating black

hole. Here, we consider the parametric cooling as prescribed by Narayan & Yi (1994) [20] for our analysis. In Fig. 3.9, we plot the variation of shock locations (x_s) (upper panel), outflow rates ($R_{\dot{m}}$) (middle panel) and compression ratio (R) (lower panel) with cooling factor f. To obtain the result, here we choose $x_{\rm inj} = 500$, $\mathcal{E}_{\rm inj} = 0.0015$, $\alpha = 0.05$ and $a_k = 0.5$, respectively. In the figure, solid, dotted and dashed curves represent the results corresponding to the angular momentum at $x_{\rm inj}$ as $\lambda_{\rm inj} = 3.975$, 4.0 and 4.025, respectively. In Fig. 3.9a, we find that the shock location proceeds towards the black hole horizon with the decrease of cooling parameter (f). Actually, in presence of cooling, flow loses its energy while accreting towards the black hole. In particular, cooling is more effective in the post-shock region compared to the pre-shock region due to the enhanced density and temperature distributions. This reduces the post-shock thermal pressure which eventually compels the shock front to move towards the black hole in order to maintain pressure balance across the shock. As a consequence, the size of the PSC is decreased with the increase of cooling causing the reduction of $R_{\dot{m}}$ as depicted in Fig. 3.9b. In addition, as the shock front moves closer to the black hole, the corresponding compression ratio (R) is enhanced with cooling as shown in Fig. 3.9c. We also observe that for a fixed cooling parameter, the shock location recedes away from black hole with the increase of angular momentum at the outer edge ($x_{\rm inj}$). This provides an indication that the shock transition seems to be centrifugally driven.

We continue our study of shock parameter space in the $\mathcal{E}_{\rm in} - \lambda_{\rm in}$ plane in presence of cooling. Towards this, we examine the modification of the parameter space with the increase of the cooling factor f and present it in Fig. 3.10. Here, we choose $a_k = 0.5$ and $\alpha = 0.05$, respectively. As before, the region bounded by the solid and dotted curves represent the shock parameter space in absence and in presence of mass loss. In this figure, chosen cooling factors (f) are marked. As the cooling is increased, the effective region of the shock parameter spaces both with and without mass loss is reduced and it is shifted towards the negative energy region. Needless to mention that beyond a critical cooling limit, namely $f \to 0.05$, parameter space for outflow disappears completely.

3.4 HFQPOs and Spin of BH sources - Application to GRO J1655-40

In this section, we attempt to constrain the rotation parameter i.e., spin of astrophysical black holes based on our accretion-ejection formalism. For the purpose of representation, we consider a Galactic black hole source GRO J1655-40 which is transient in nature and known to produce superluminal jets [54, 238, 239]. The source is considered to be one of the nearest Galactic black hole source with a distance of 3.2 kpc [177] and inclination angle 69 $\pm$ 2 [240]. So far, it has been observed that this source exhibits the maximum QPO frequency ($\sim$450 Hz) among all the known black hole candidates [131, 241]. The mass of the source is believed to be well constrained by dynamical method that estimates the range of mass to be $5.1M_{\odot}$ to $6.3M_{\odot}$ [211, 242]. However, the measurement of the spin of the black hole remains inconclusive yet. Numerous groups used various methods while predicting the spin of the black hole with large uncertainties, namely the *spectral continuum model* predicts the spin to be in the range of 0.65 to 0.75 [212], whereas Miller et al. (2009) [243] predicted the spin to be in the range of 0.94 to 0.98 using *relativistic reflection* and *disc continuum emission* models. However, recent measurement which is based on the relativistic precession model of low frequency QPOs obtains the spin to be $\sim$ 0.29 [118]. Meanwhile, in the theoretical front, efforts were made to model the origin of the high frequency QPOs considering the coupling between the angular momentum of the black hole (*i.e.*, spin) and orbital frequency at the innermost stable circular orbit (ISCO) and obtain the range of black hole spin as $0.2 < a_k < 0.67$ [134]. A very recent work carried out by Stuchlik & Kolos (2016) [244] predicted the lower limit of the spin to be > 0.3 based on the non-geodesic string loop oscillation model of twin high frequency QPOs. Since the discrepancy of the spin measurement is not settled yet, this motivates us to constrain the rotation parameter based on our formalism.

3.4.1 Observation and Data Reduction

The Galactic black hole source GRO J1655-40 has two characteristic HFQPOs observed at $\sim$ 300 Hz and $\sim$ 450 Hz in the power spectrum. There have been several detections of the 300 Hz HFQPOs during the 1996 outburst of the source. The detection of 300 Hz HFQPOs [131, 245] is not so significant, whereas the detection of 450 Hz HFQPO [131, 246] is prominent and significant. For our specific purpose,

we re-analysed the archival RXTE data for both HFQPOs ($\sim$ 300 Hz and $\sim$ 450 Hz). We use two RXTE observations which was carried out on 01 August, 1996 (ObsID: 10255-01-04-00) and on 09 September, 1996 (ObsID: 10255-01-10-00) for the detection of HFQPOs at $\sim$ 300 Hz and $\sim$ 450, Hz respectively. For both observations, light curves were generated with a time resolution of 0.00048828125 sec with Nyquist frequency of 1024 Hz in the energy band of 2-12 keV, 13-27 keV and 2-27 keV. We extract light curve from science array data (exposure of $\sim$ 9 ksec) for the observation on 01 August, 1996 and from science event data (exposure of $\sim$ 8 ksec) for the observation on 09 September, 1996 based on required time resolution and energy ranges. Further, we follow the standard procedures (see [49, 237] to extract the energy spectrum in the energy range of $3 - 150$ keV using both PCA ($3 - 30$ keV) and HEXTE ($25 - 150$ keV) data of RXTE observations.

3.4.2 Analysis and Modelling

We compute the power spectra for both observations in the range 20 Hz to 1024 Hz with 8192 newbins per frame and with a geometrical binning factor of -1.02. The 300 Hz QPO was detected only in the energy range 2-12 keV while the 450 Hz HFQPO was observed in the energy range 13-27 keV. The power spectra are modeled with a *lorentzian* and *powerlaw* components for QPO like feature and continuum in the lower frequency range respectively. Fig. 3.11 shows the simultaneous plot of both HFQPOs observed in GRO J1655-40 during 1996 outburst.

The $\sim$ 300 Hz HFQPO has centroid frequency at 275 ± 9 Hz (see Fig. 3.11) with an FWHM of 71.7 Hz. The detection of broad feature has a significance of $\sim$ 4.17 and a Q-factor of $\sim$ 3.84. Power spectrum also shows two more QPO like feature at around 57 Hz and 80 Hz. The highest observed HFQPO (see Fig. 3.11) was found at a central frequency of 444.8 Hz with an FWHM of 32.4 Hz, a significance of 2.79 and a Q-factor of 13.72. Both HFQPOs plotted in Fig. 3.11 is in *Leahy Power - Frequency* space [247].

Now, we calculate the QPO frequency ($\nu_{\rm QPO}$) based on our accretion-ejection model. Here, we compute the infall time from the post-shock velocity profile as $t_{\rm infall} = \int dt = \int_{x_s}^{x_{\rm in}} \frac{dx}{v(x)}$, where $v(x)$ is the post-shock velocity. The integration is carried out from the shock location to the inner sonic point as the distance between the inner sonic point and event horizon is negligibly small. We estimate the QPO frequency as $\nu_{QPO} = \frac{1}{t_{\rm QPO}} \sim \frac{1}{t_{\rm infall}}$ in units of $\frac{r_g}{c}$ [154]. Accordingly, QPO frequency is converted into the unit of Hertz when it is multiplied with $\frac{c}{r_g}$. Here, we consider the

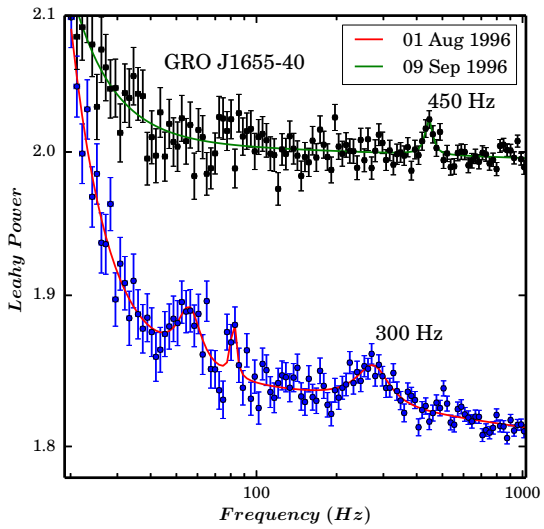

Figure 3.11: Power spectra corresponding to the $\sim$ 300 Hz and $\sim$ 450 Hz HFQPOs of GRO J1655-40 during its 1996 outburst are shown in *Lehay Power - Frequency* space. The QPO like features are modelled with *lorentzians*. Detection of HFQPOs at $\sim$ 300 Hz and $\sim$ 450 Hz are marked in the plot.

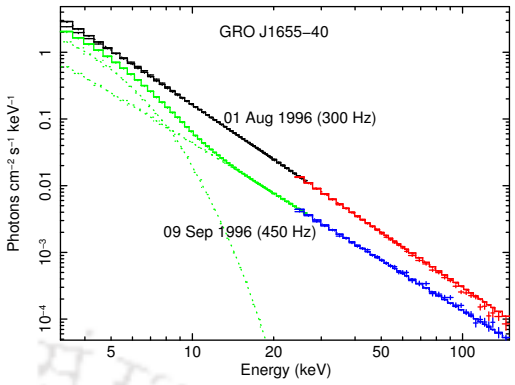

Figure 3.12: Broadband energy spectra (3-150 keV) using PCA and HEXTE data corresponding to the $\sim$ 300 Hz and $\sim$ 450 Hz HFQPOs are observed during 1996 outburst of GRO J1665-40. Both energy spectra show strong high energy emission with steep powerlaw component. Interestingly, the energy spectrum of 300 Hz observation shows very weak signature of thermal emission, whereas thermal emission is strong in the energy spectrum of 450 Hz observation. See text for details.

mass of the source GRO J1655-40 as $6M_{\odot}$. With this, we calculate the maximum QPO frequency ($\nu_{\rm QPO}^{\rm max}$) as function of a_k for various viscosity parameters as depicted in Fig. 3.13a. Here, we vary the remaining flow variables (*i.e.*, $\mathcal{E}_{\rm in}$ and $\lambda_{\rm in}$) freely to obtain $\nu_{\rm QPO}^{\rm max}$. Filled circles connected with the solid, dotted and dashed curves denote the results corresponding to $\alpha = 0.01$ (black), 0.05 (red) and 0.1 (blue), respectively. In the present analysis, when a_k is increased, shock usually forms closer to the black hole (see Fig. 3.4) which apparently yields the high frequency QPOs. Therefore, a positive correlation between $\nu_{\rm QPO}^{\rm max}$ and a_k is very much desirable and it is seen in Fig. 3.13a. Moreover, we find that the maximum QPO frequency generally lies in the range 150 Hz $\lesssim \nu_{\rm QPO}^{\rm max} \lesssim$ 780 Hz depending on the values of a_k and α for this source. The variation of the outflow rates ($R_{\dot{\rm m}}$) corresponding to the results displayed in the upper panel of Fig. 3.13 is shown in the middle panel (Fig. 3.13b). As $\nu_{\rm QPO}^{\rm max}$ corresponds to the minimum shock location ($x_s^{\rm min}$) and $\nu_{\rm QPO}^{\rm max}$ increases with the increase of a_k, the size of PSC (which is basically the area of the jet base) is consequently reduced resulting the lowering of outflow rate. For

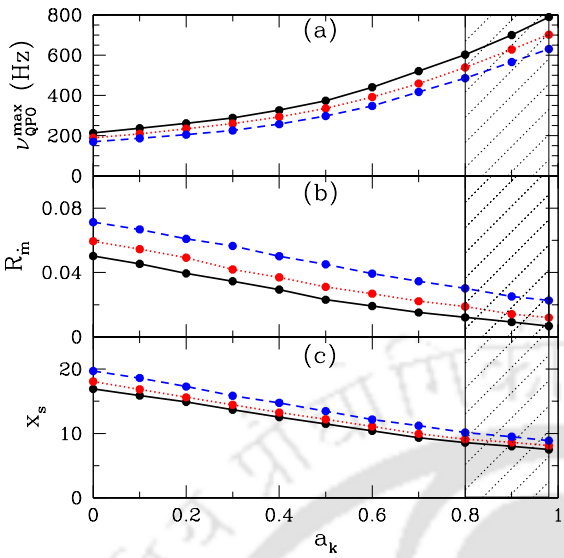

Figure 3.13: Variation of (a) maximum QPO frequency ($\nu_{\rm QPO}^{\rm max}$), (b) corresponding mass outflow rates ($R_{\dot{m}}$) and (c) shock location (x_s) with the spin (a_k) corresponding to the black hole mass ($M_{\rm BH} = 6M_\odot$) of GRO J1655-40. Solid, dotted and dashed curves represent $\alpha = 0.01$ (black), 0.05 (red) and 0.1 (blue), respectively. In each panel, shaded region denotes results for $a_k > 0.8$. See text for details.

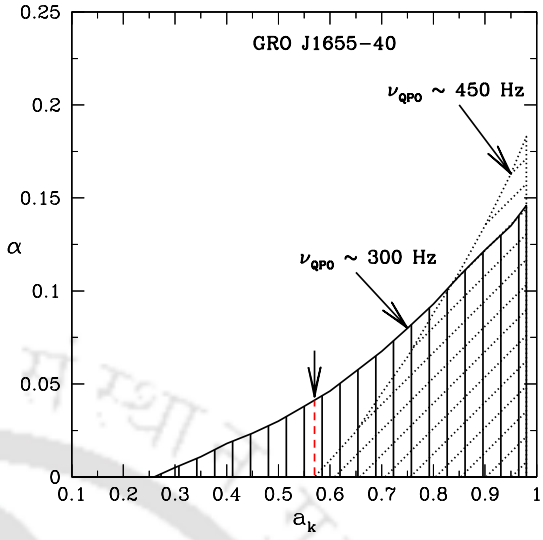

Figure 3.14: Ranges of viscosity parameter (α) and black hole spin (a_k) that provide HFQPOs $\nu_{\rm QPO} \sim 300$ Hz and ~ 450 Hz observed in GRO J1655-40.

completeness, we also show the variation of shock location associated to $\nu_{\rm QPO}^{\rm max}$ in the bottom panel (Fig. 3.13c). In each panel, the shaded region represents the results obtained for $a_k \geq 0.8$.

Following the prescription of Aktar et al. (2017) [248], we identify the parameter spaces spanned by the black hole spin (a_k) and viscosity (α) that successfully reproduce the HFQPOs (~ 300 Hz and ~ 450 Hz) observed for the black hole source GRO J1655-40. While doing so, we vary all the remaining flow variables freely and consider the mass of GRO J1655-40 as $6M_\odot$ [211, 242]. In Fig. 3.14, the region shaded with solid and dotted lines denote the parameter space corresponding to ~ 300 Hz and ~ 450 Hz. The latter result is recently reported by Aktar et al. (2017) [248], where authors constrained the spin of GRO J1655-40 and found the minimum value $a_k^{\rm min} \sim 0.57$ as indicated by the dashed vertical (red) line with downward arrow at the top. The viscosity associated with $a_k^{\rm min}$ is obtained as $\alpha \sim 0$. Since black hole spin is not expected to evolve noticeably within the couple of weeks or so, it

is reasonable to adhere the above spin range and calculate the range of viscosity as function of a_k that provides $\sim$ 300 Hz QPOs. We find that viscosity spreads over a wide range for all a_k and in particular, we obtain $0 \leq \alpha < 0.04$ for $a_k^{\rm min} \sim 0.57$. When the apriori restriction on a_k is removed, we find the spin ranges for $\sim$ 300 Hz QPO is $a_k \geq 0.26$ which is in agreement with the results reported in the literature [118, 134, 244]. Since there exists a common overlapping region in the $a_k - \alpha$ plane, we argue that the spin of the black hole source GRO J1655-40 seems to be $a_k \geq 0.57$. This result seems to be in well agreement with the observational results of Shafee et al. (2006) [212] and Miller et al. (2009) [243].

3.5 Chapter Conclusion

In this chapter, we describe a self-consistent formalism to calculate the mass outflow rates from the dissipative accretion flow around the rotating black holes in presence of viscosity and cooling processes. Effort of this kind was not considered before to investigate the outflow properties around rotating black holes. We present the governing equations for accretion and ejection mechanisms in details and demonstrate the methodology to obtain the inflow-outflow solutions. Since the black hole accretion solutions are transonic in nature, we present the sonic point analysis and demonstrate the sonic point properties. With this, we obtain the complete global accretion solutions that may contain shock wave. Because of shock compression, an excess thermal pressure is developed across the shock that causes the post-shock flow to become puffed up which equivalently behaves like Comptonized corona (*i.e.*, PSC). A part of the inflowing matter after being intercepted at PSC is diverted along the black hole rotation axis to form thermally driven bipolar outflow (Molteni et al. 1996). Considering this appealing mechanism, subsequently, we obtain the coupled inflow-outflow solutions. We show that for a wide range of inflow parameters, accretion flow can exhibit outflows even when the viscosity and cooling are very high. We observe that shocks in accretion flow form within the range of few to several tens of Schwarzschild radius depending on the inflow parameters. We also observe that as the effect of dissipation is increased, namely in the form of viscosity and cooling processes, shock moves closer to the horizon and the corresponding outflow rate ($R_{\dot{\rm m}}$) correlates with the shock location for flows with same outer boundary condition (Fig. 3.3).

We show that outflows from the dissipative accretion disc can occur around non-rotating as well as rotating black holes. When a part of the inflowing matter

is ejected out from the PSC as outflow, the post-shock pressure is decreased that eventually allows the shock front to proceed towards the horizon to maintain the pressure balance across the shock. Interestingly, in absence of mass loss ($R_{\dot{m}} = 0$), when the triggering of shock transition takes place at its minimum location from the horizon ($x_s^{\rm min}$), the coupled inflow-outflow solution ceases to exist as the stationary shock conditions are not satisfied there. This eventually indicates that when the effects of viscosity and cooling remain fixed, the range of the inflow parameters for outflow solutions is reduced compared to the global shocked accretion solution with $R_{\dot{m}} = 0$. Effectively, the domain of the shock parameter space spanned by $\lambda_{\rm in}$ and $\mathcal{E}_{\rm in}$ is shrunk with the increase of dissipation and it is reduced further when mass-loss is included (Fig. 3.5). In this study, we observe three distinct features of the modified shock parameter space. We find that when viscosity parameter (α) is increased keeping spin of the black hole (a_k) and cooling parameter (f) fixed, the effective area of the shock parameter space, both in absence and presence of mass loss, shifts to higher energy and lower angular momentum domain. This happens due to the fact that the accreting matter becomes relatively much hotter when it enters into the gravitational potential of rapidly spinning black hole compared to the non-rotating black hole [249]. We further compare the shock parameter spaces for flows with increasing viscosity parameter keeping cooling parameter (f) and a_k fixed. Due to increase of viscosity, accreting matter not only transports more and more angular momentum outward, but it also causes the flow to become hotter. This evidently renders the shock parameter space to shift to the higher energy and lower angular momentum domain (Fig. 3.5). For a cooling dominated flow, the shock parameter space is shrunk and shifted to negative energy region (Fig. 3.10).

We estimate the maximum viscosity parameter that provides global shocked accretion solution both by excluding mass loss ($\alpha_{\rm no}^{\rm max}$) and including mass loss ($\alpha_{\rm o}^{\rm max}$). Since the possibility of shock formation reduces in presence of mass loss, we obtain $\alpha_{\rm o}^{\rm max} < \alpha_{\rm no}^{\rm max}$ for a given a_k. We further find that the obtained values of $\alpha_{\rm no}^{\rm max} \sim 0.35$ and $\alpha_{\rm o}^{\rm max} \sim 0.25$ in the limit of $a_k \to 0$ are in agreement with the results reported by Chakrabarti & Das (2004) [232] and Kumar & Chattopadhyay (2013) [45]. Moreover, we calculate the maximum mass outflow rate ($R_{\dot{m}}^{\rm max}$) as function of viscosity parameter (α) by exploring all possible combination of inflow parameters and find that $R_{\dot{m}}^{\rm max}$ is largely obtained for higher $\mathcal{E}_{\rm in}$ and lower $\lambda_{\rm in}$ values irrespective to the values of a_k (Fig. 3.7). In Fig. 3.8, we depict the computed values of $R_{\dot{m}}^{\rm max}$ as function of α and find the range as $3\% \leq R_{\dot{m}}^{\rm max} \leq 19\%$.

It is worthy to address a very interesting finding that is emerged out from our

study here. We have pointed out that when the viscosity as well as cooling parameters are considered beyond their critical values, coupled inflow-outflow solution ceases to exist. However, non-steady shock still may present as shown by Ryu et al. (1997), Das et al. (2014) [125, 250]. Meanwhile, Molteni et al. (1996) and Chakrabarti & Manickam (2000) [154, 251] showed that QPO frequency of emergent hard radiation from the black holes is proportional to the infall time of the accreting matter. Adopting this prescription, we employ our formalism to calculate the maximum QPO frequency ($\nu_{\rm QPO}^{\rm max}$) as function of a_k for flows with various α. We then attempt to constrain the spin of the black hole source GRO J1655-40 considering the highest QPO frequency ~ 450 Hz observed in this source (Fig. 3.11). Based on our present analysis, we find that $a_k \geq 0.57$ for this source (Fig. 3.14).

An important point is to be noted that in late 90's, Blandford & Begelman (1999) [28] found the advection dominated inflow-outflow solutions (ADIOS) around a Newtonian central object. There are subtle differences between our study and ADIOS, one of which arises mainly due to the choice of the accretion rate equation. In ADIOS model, the accretion rate is assumed to satisfy the power low dependence on radial coordinate as $\dot{M} \propto x^s$ with $0 \leq s < 1$ whereas no such restriction is imposed in our study (see Eq. 3.2). In addition, in this work, we have considered dissipative accretion flow including viscosity and radiative cooling which were ignored in ADIOS model. Moreover, we obtain the self-consistent accretion-ejection solutions that are coupled via Rankine-Hugoniot shock and in ADIOS model, mass loss is allowed to take place from all radial coordinates.

Chapter 4

Accretion-ejection in rotating black holes: a model for 'outliers' track of radio-X-ray correlation in X-ray binaries

.

Complete understanding of accretion properties around black hole using full general relativistic calculation is rigorous and complex. The exercise becomes even more difficult in the case of dissipative flow. Fortunately, there is a remedy in terms of pseudo-potential that allows us to utilize the Newtonian concept while retaining the salient features of the black hole space-time geometry. It was Paczyński & Witta (1980) [3] who first introduced pseudo-Newtonian potential for Schwarzchild black hole and this potential receives tremendous success in both analytical as well as numerical studies [20, 38, 39, 125, 154, 163–166, 232, 252–255]. Following the same spirit, several attempts were made to construct pseudo-Kerr potential for rotating black hole as well. Initially, Chakrabarti & Khanna (1992) [143] proposed a pseudo-Kerr potential which is able to replicate the Kerr-geometry at the equatorial plane with reasonable accuracy. Later, Artemova et al. (1996) [144] (hereafter ABN96) introduced a prescription for free-fall acceleration around Kerr black hole. The derivation of pseudo-Kerr potential from this free-fall acceleration is simple and this potential reproduces the features of Kerr geometry quite well. After that, Mukhopadhyay (2002) [145] (hereafter MU02) formulated another pseudo-Kerr potential which is

The contents of this chapter is submitted to Astrophysics and Space Science; Aktar R., Nandi A., Das S., (2018)

derived in the realm of Kerr space-time geometry. Latter on, Chakrabarti & Mondal (2006) [146] (hereafter CM06) prescribed the modified version of the Chakrabarti & Khanna (1992) [143] potential which satisfactorily mimics the space time geometry around rotating black hole for black hole spin $a_k \leq 0.8$. All these pseudo-potentials are formulated and prescribed individually and they have their own limitations to approximate the Kerr space-time geometry. Since the ultimate motivation of these potentials is to describe the space-time geometry around the rotating black hole appropriately, it is essential as well as timely to carry out a comparative study involving all of them. In this context, we consider three different pseudo-Kerr potentials, namely ABN96 [144], MU02 [145] and CM06 [146] and study the global transonic accretion flow solutions that contain standing shocks. We compare the shock parameter space spanned by the energy ($\mathcal{E}_{\rm in}$) and angular momentum ($\lambda_{\rm in}$) measured at the inner critical point ($x_{\rm in}$) for inviscid as well as viscous flow. We also compare the critical viscosity parameter calculated using different pseudo potentials that admits standing shock ($\alpha^{\rm cri}_{\rm shock}$) and realize that all the pseudo-potentials behave similarly for weakly rotating black holes although they differ considerably when spin of the black hole is increased. Finally, we allow mass loss from the disc and obtain the accretion-ejection solutions. With this, we estimate the maximum outflow rates ($R^{\rm max}_{\dot{m}}$ in terms of spin (a_k) of the black hole employing the accretion-ejection formalism ([228] for all the pseudo-Kerr potentials. Thereafter, we estimate the maximum kinetic jet power and compare it with the radio-X-ray correlation in black hole X-ray binaries (XRBs) [4]. Based on this comparative study, we indicate that black hole XRBs along the 'outliers' track are mostly rapidly rotating.

4.1 Modeling of Accretion Disc

We consider a steady, advective, viscous, geometrically thin, axisymmetric, accretion flow around a rotating black hole. Here, we consider the disc is confined in the equatorial plane and the jet or outflow geometry is considered in the off-equatorial plane about the axis of rotation of the black hole [43, 154]. For simplicity, we adopt pseudo-Kerr approach to describe the space-time geometry around rotating black holes.

4.1.1 Governing Equations for accretion

Here, we present the hydrodynamical equations that govern the accretion flow around rotating black hole and are given by,
(i) The radial momentum conservation equation:

$$v\frac{dv}{dx}+\frac{1}{\rho}\frac{dP}{dx}+\frac{d\Phi_i^{\rm eff}}{dx}=0, \tag{4.1}$$

where v, P, ρ and x represent the radial velocity, isotropic gas pressure, density and radial distance of the flow, respectively. Here, $\Phi_i^{\rm eff}$ is the effective pseudo-Kerr potential around black hole and the subscript i can take any one value among 1 (ABN96 [144]), 2 (MU02 [145]), and 3 (CM06 [146]) depending on the choice of the pseudo-potential (see §1.6.3 for detail expression). We define the adiabatic sound speed as $a=\sqrt{\gamma P/\rho}$, where γ represents the adiabatic index.
(ii) The mass conservation equation:

$$\dot{M}=4\pi\rho v x h(x), \tag{4.2}$$

where $\dot{M}$ denotes the mass accretion rate which is a global constant throughout the flow except the region of mass loss and 4π is the geometric constant. Here, $h(x)$ refers to the half-thickness of the flow. Considering the hydrostatic equilibrium in the vertical direction for thin disc, we calculate the half-thickness of the disc as,

$$h(x)=a\sqrt{\frac{x}{\gamma F_i(x)}}, \tag{4.3}$$

where $F_i(x)$ represents the pseudo-Kerr force corresponding to the pseudo-Kerr potential described in §1.6.3.
(iii) The angular momentum distribution equation:

$$v\frac{d\lambda}{dx}+\frac{1}{\Sigma x}\frac{d}{dx}(x^2W_{x\phi})=0, \tag{4.4}$$

where $W_{x\phi}$ is the $x\phi$ component of the viscous stress tensor. Following Chakrabarti (1996) [230], we consider the expression of $W_{x\phi}$ as,

$$W_{x\phi}^{(1)}=-\alpha(W+\Sigma v^2). \tag{4.5}$$

where α denotes the viscosity parameter. Here, $W(=2I_{n+1}Ph)$ and $\Sigma(=2I_n\rho h)$ represent the vertically integrated pressure and density [231]. Here, I_n and I_{n+1} are

the constant factors of integration of vertically averaged density and pressure [231]. And, $I_n = (2^n n!)^2/(2n+1)!$ and $n = 1/(\gamma - 1)$ is the polytropic index.

Finally, (iv) The entropy generation equation:

$$\Sigma v T \frac{ds}{dx} = Q^+ - Q^-, \tag{4.6}$$

where T is the temperature and s is the entropy density of the accretion flow, respectively. In addition, Q^+ and Q^- represent the heat gain and heat lost by the flow. In this work, for the purpose of simplicity, we ignore cooling effect and consequently we choose $Q^- = 0$. After some simple algebra, Eq. 4.6 becomes,

$$\frac{v}{\gamma - 1}\left[\frac{1}{\rho}\frac{dP}{dx} - \frac{\gamma P}{\rho^2}\frac{d\rho}{dx}\right] = -\frac{Q^+}{\rho h} = -H. \tag{4.7}$$

Using the mixed shear stress prescription [230, 248], we calculate the heating of the flow by means of viscous dissipation as,

$$Q^+ = A\rho h(ga^2 + \gamma v^2)\left(x\frac{d\Omega}{dx}\right), \tag{4.8}$$

where $A = \frac{2\alpha I_n}{\gamma}$ and $g = \frac{I_{n+1}}{I_n}$.

4.1.2 Critical Point Conditions

In the process of accretion on to black hole, inflowing matter starts its journey subsonically from the outer edge of the disk and eventually enters into the black hole with supersonic speed. This scenario evidently demands that accretion flow must change its sonic state from subsonic to supersonic at some point between the outer edge of the disc and the black hole horizon. Such a special point is called as critical point where accretion flow maintains certain conditions. In order to calculate these critical point conditions, we make use of equations (4.1 - 4.8) to obtain the velocity gradient which is given by,

$$\frac{dv}{dx} = \frac{N}{D}, \tag{4.9}$$

where

$$N = -\frac{A\alpha(ga^2+\gamma v^2)^2}{\gamma v x} - \frac{3a^2 v}{(\gamma-1)x} + \frac{a^2 v}{(\gamma-1)}\left(\frac{d\ln F_i(x)}{dx}\right) - \frac{3A\alpha g a^2(ga^2+\gamma v^2)}{\gamma v x} + \left[\frac{2A\alpha g(ga^2+\delta\gamma v^2)}{v} + \frac{(\gamma+1)v}{(\gamma-1)}\right]\left(\frac{d\Phi_i^{\rm eff}}{dx}\right) + \frac{A\alpha g a^2(ga^2+\gamma v^2)}{\gamma v}\left(\frac{d\ln F_i(x)}{dx}\right) + \frac{2A\lambda(ga^2+\gamma v^2)}{x^2}, \tag{4.10}$$

and

$$D = \frac{2a^2}{(\gamma-1)} - \frac{(\gamma+1)v^2}{(\gamma-1)} - A\alpha(ga^2+\gamma v^2)\left[(2g-1) - \frac{ga^2}{\gamma v^2}\right]. \tag{4.11}$$

Using equation (4.4) and (4.9), we calculate the gradient of angular momentum as,

$$\frac{d\lambda}{dx} = \frac{\alpha}{\gamma v}(ga^2+\gamma v^2) + \frac{2\alpha x g a}{\gamma v}\left(\frac{da}{dx}\right) + \alpha x\left(1-\frac{ga^2}{\gamma v^2}\right)\left(\frac{dv}{dx}\right) \tag{4.12}$$

Further, we calculate the gradient of sound speed using equations (4.1 - 4.3) as,

$$\frac{da}{dx} = \left(\frac{a}{v} - \frac{\gamma v}{a}\right)\frac{dv}{dx} + \frac{3a}{2x} - \frac{a}{2}\left(\frac{d\ln F_i(x)}{dx}\right) - \frac{\gamma}{a}\left(\frac{d\Phi_i^{\rm eff}}{dx}\right). \tag{4.13}$$

As discussed, the accreting matter around black hole is smooth everywhere along the flow streamline and therefore, the radial velocity gradient must be real and finite always. However, depending on the flow variables, D may vanish at some radial coordinate. Since dv/dx remains smooth always, the point where D tends to zero, N must also vanish there. Such a point where both N and D simultaneously goes to zero is identified as critical point and $N = D = 0$ are the critical point conditions. Setting $D = 0$, we find the radial velocity of the flow (v_c) at the critical point (x_c) as,

$$v_c^2 = \frac{-m_b - \sqrt{m_b^2 - 4m_a m_c}}{2m_a} a_c^2, \tag{4.14}$$

where a_c is the sound speed at x_c and

$$\begin{aligned} m_a =& -A\alpha\gamma^2(\gamma-1)(2g-1)-\gamma(\gamma+1), \\ m_b =& 2\gamma - 2A\alpha g\gamma(\gamma-1)(g-1), \\ m_c =& A\alpha g^2(\gamma-1). \end{aligned}$$

Setting $N=0$, we calculate a_c as,

$$a_c = \frac{-a_2-\sqrt{a_2-4a_1a_3}}{2a_1}, \tag{4.15}$$

where

$$\begin{aligned} a_1 =& -\frac{A\alpha(g+\gamma M_c^2)^2}{\gamma x} - \frac{3M_c^2}{(\gamma-1)x} + \frac{M_c^2}{(\gamma-1)}\left(\frac{d\ln F_i(x)}{dx}\right) - \frac{3A\alpha g(g+\gamma M_c^2)}{\gamma x} \\ &+ \frac{A\alpha g(g+\gamma M_c^2)}{\gamma}\left(\frac{d\ln F_i(x)}{dx}\right), \\ a_2 =& \frac{2A\lambda M_c(g+\gamma M_c^2)}{x^2}, \\ a_3 =& -\left[2A\alpha g(g+\gamma M_c^2)+\frac{(\gamma+1)M_c^2}{(\gamma-1)}\right]\left(\frac{d\Phi_i^{\rm eff}}{dx}\right). \end{aligned}$$

Here, M_c refers the Mach number at x_c where Mach number of the flow is defined as $M=v/a$.

The nature of the critical point is determined by the value of dv/dx at x_c ([170], reference therein). At the critical point, $dv/dx = 0/0$ and therefore, we apply l'Hospital rule to calculate $(dv/dx)_c$. Usually, $(dv/dx)_c$ possesses two values. When both the derivatives are real and of opposite sign, the critical point is called as saddle type critical point and any physically acceptable accretion solution can only pass through it. When shock forms, accretion flow passes through two saddle type critical points: one in the pre-shock region and the other in the post-shock region ([232], references therein). In the subsequent sections, we refer the saddle type critical point as critical point only. In general, critical points in the post-shock flow form very close to the horizon and called as inner critical points ($x_{\rm in}$). On the other hand, critical points in the pre-shock flow usually form far away from the black hole and called as outer critical points ($x_{\rm out}$).

4.1.3 Equations for Outflow and Computation of Mass Loss

Due to the shock transition, the post-shock flow becomes very hot and dense and eventually, PSC acts as effective boundary around black hole. As a result, a part of the accreting matter is deflected by PSC and driven out in the vertical direction by the excess thermal gradient force across the shock, producing bipolar outflows ([41, 43, 44], and reference therein). To calculate the mass outflow rates, we follow the exact same procedures as mentioned in Aktar et al. (2015, 2017) [228, 248]. As the jets are tenuous in nature, we ignore viscosity in the outflowing matter. We also consider that the outflowing matter obey the polytropic equation of states i.e., $P_j = K_j \rho_j^{\gamma}$, where '$j$' subscript and K_j represent the jet variables and measure of specific entropy of the jet, respectively. The equations of motion for the outflow are given below.

(i)The energy conservation equation of outflow:

$$\mathcal{E}_j = \frac{v_j^2}{2} + \frac{a_j^2}{\gamma - 1} + \Phi_i^{\rm eff}, \tag{4.16}$$

where, $\mathcal{E}_j$, v_j and a_j are the specific energy, velocity and sound speed for the outflowing matter, respectively. $\Phi_i^{\rm eff}$ is the effective pseudo-Kerr potentials mentioned in section 1.6.3.

(ii)The mass conservation equation of outflow:

$$\dot{M}_{\rm out} = \rho_j v_j \mathcal{A}_j, \tag{4.17}$$

where, $\dot{M}_{\rm out}$ and $\mathcal{A}_j$ are the outflowing mass rate and area function for the jet, respectively. We calculate $\mathcal{A}_j$ by knowing the radius of two boundary surfaces, namely centrifugal barrier (CB) and funnel wall (FW) [154]. The radius of CB is obtained using pressure maximum surface i.e., $(d\Phi_i^{\rm eff}/dx)_{r_{\rm CB}} = 0$ and the radius of FW is defined as the pressure minimum surface i.e., $\Phi_i^{\rm eff} = 0$ [154, 228, 248]. We also consider the projection factor $\sqrt{1 + (dx_j/dy_j)^2}$ for calculating jet area function [45, 248].

As the outflow is originated from the post-shock region and, so we assume that the outflow is essentially launched with the same density as in the PSC, i.e. $\rho_j = \rho_+$. Therefore, using the equations (4.2), (4.3) and (4.17), we calculate the mass outflow

rates as

$$R_{\dot{m}} = \frac{Rv_j(x_s)\mathcal{A}_j(x_s)}{4\pi\sqrt{\frac{1}{\gamma}}F_i^{-1/2}(x_s)a_+v_-}, \tag{4.18}$$

where, R is the compression ratio defined as $R = \Sigma_+/\Sigma_-$. Also, $v_j(x_s)$, $\mathcal{A}_j(x_s)$ and $F_i(x_s)$ are the jet velocity, jet area function and pseudo-Kerr force calculated at the shock x_s, respectively. We use the successive iterative method to calculate $R_{\dot{m}}$ as described in [228, 248, 256].

4.2 Results

4.2.1 Global Accretion Solution including shock

To obtain the global transonic accretion solution, we choose a set of flow variables, namely, critical point (x_c), angular momentum at x_c (λ_c) and viscosity parameter (α) and simultaneously integrate equations (4.12 - 4.14) from the critical point once inward up to the horizon and then outward up to a large distance representing the outer edge of the disc ($x_{\rm edge}$). Finally, we join these two parts of the solution to get a complete global transonic accretion solution around black hole. We note the values of all the flow variables at $x_{\rm edge}$. In actuality, we would get the same accretion solution obtained above, when equations (4.12 - 4.14) are solved using the outer edge flow variables.

In §4.1.2, we point out that shocked accretion flow must contains two critical points. In reality, during the course of accretion, subsonic accretion flow from the outer edge of the disc first crosses the outer critical point ($x_{\rm out}$) to become supersonic and continues to accrete towards the black hole. Meanwhile, centrifugal repulsion becomes dominant in the vicinity of the black hole and hence, inflowing matter is forced to be slowed down there. Effectively, a virtual centrifugal barrier is formed that triggers the discontinuous transitions of flow variables in the subsonic region which is commonly know as shock transition. In order for standing shock transition, RH shock conditions need to be satisfied (see Chpater 2 and Chapter 3). After the shock transition, flow gradually picks its speed due to the strong gravitational pull and ultimately enters into the black hole supersonically after passing through the inner critical point ($x_{\rm in}$). In this subsection, we consider no mass loss from the disk i.e., $R_{\dot{m}} = 0$.

In Fig. 4.1, we compare the shock induced global accretion solutions obtained

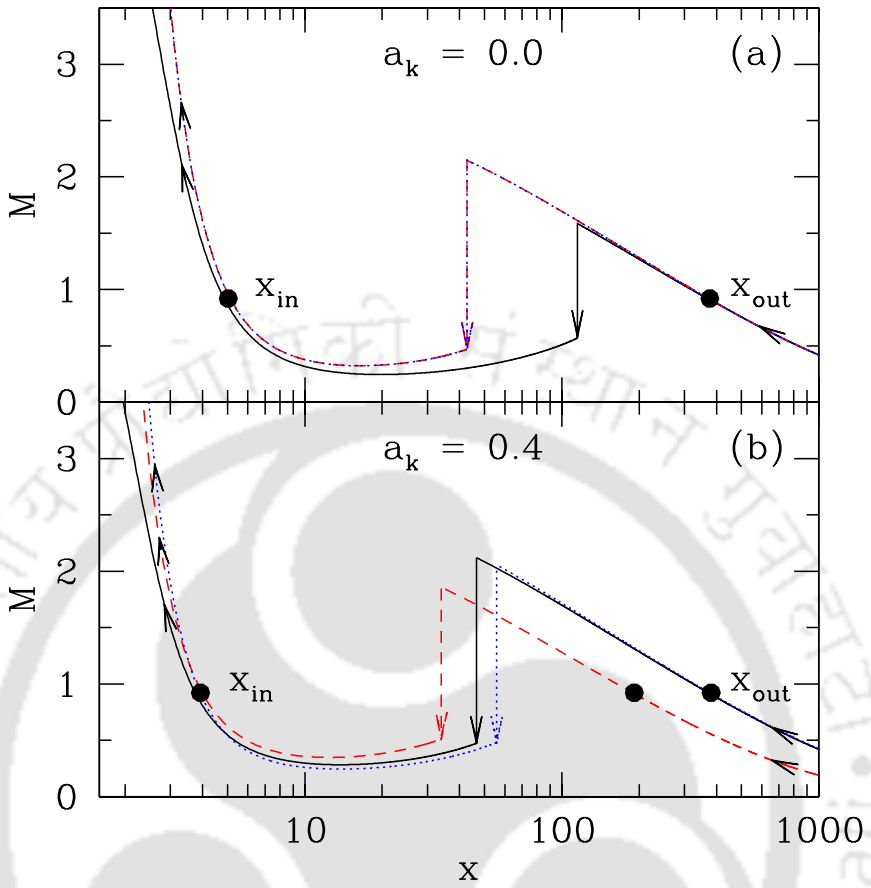

Figure 4.1: Illustration of shocked accretion solution where the variation of Mach number ($M = v/a$) is shown with radial distance (x). In the upper panel, results are shown for non-rotating ($a_k = 0$) black hole whereas in the lower panel, $a_k = 0.4$ is chosen. Solid, dotted and dashed curves represent the solutions obtained for CM06, MU02 and ABN96 potentials, respectively. Here, we fix $\gamma = 1.4$. See text for details.

using different pseudo-Kerr potentials. Here, the input parameters of the flow are kept fixed at the outer edge of the disc. In the upper panel (Fig. 4.1a) , we choose the outer edge of the disc as $x_{\rm edge} = 1000$ and inviscid accreting flow is injected from $x_{\rm edge}$ with energy $\mathcal{E}_{\rm edge} = 0.001$ and $\lambda_{\rm edge} = 3.35$ on to a non-rotating black hole. Solid, dotted and dashed curves represent the results obtained for CM06, MU02 and ABN96 potentials where the verticals arrows indicate the location of shock transitions at 115.07 for CM06 and at 42.84 for both MU02 and ABN96 potentials. In the case of non-rotating black hole (a_k), since MU02 and ABN96 potential become identical, accretion solutions for these two potentials display complete overlap all throughout. In the lower panel (Fig. 4.1b), we choose $a_k = 0.4$ and compare the shocked accretion solutions for three different potentials considering the same set of inflow parameter fixed at $x_{\rm edge}$. Here, we fix $x_{\rm edge} = 1000$, $\mathcal{E}_{\rm edge} = 0.001$, $\lambda_{\rm edge} =$

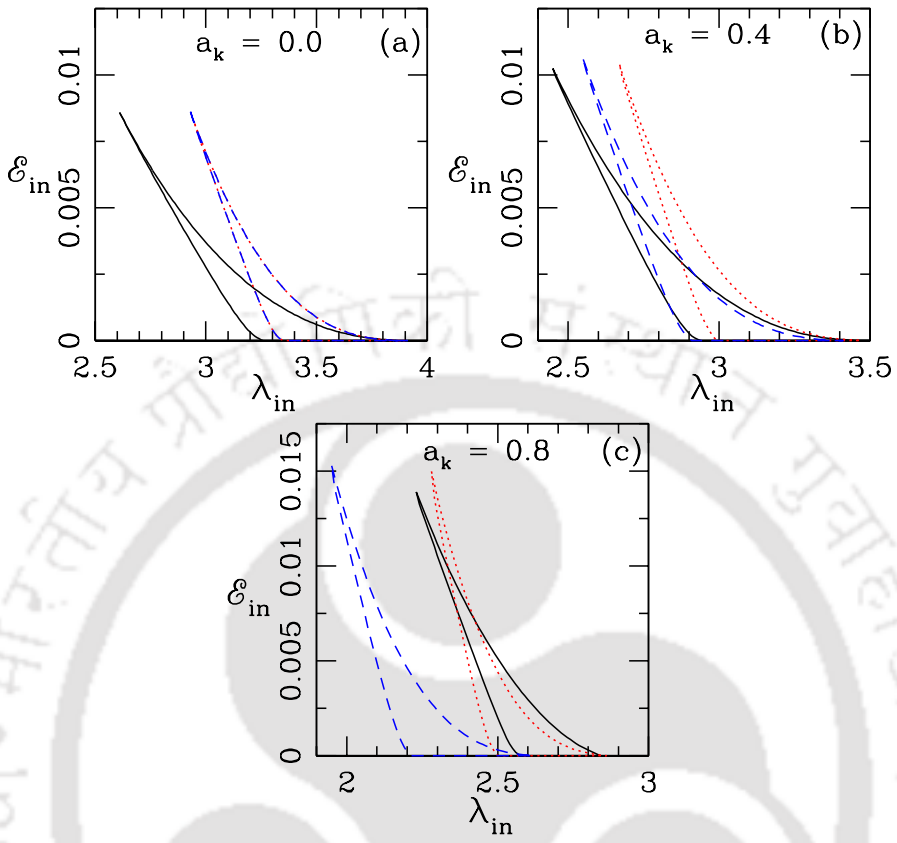

Figure 4.2: Classification of shock parameter space for three different pseudo-Kerr potentials. Here, inviscid flow ($\alpha = 0.0$) is considered for three different spin values ($a_k = 0.0, 0.4$ and 0.8) which are marked in each panel. Solid, dotted and dashed curves represent results for CM06, MU02 and ABN96 pseudo-Kerr potentials, respectively. Here, we fix $\gamma = 1.4$. See text for details.

2.98 and $\alpha = 0$. As before, solid, dotted and dashed curves denote the results corresponding to CM06, MU02 and ABN96 potentials and the respective shock locations are calculated as 46.56 (CM06), 33.99 (MU02), 55.79 (ABN96), respectively. From the figure, it is clear that even for the same set of input parameters, the adopted potentials display noticeably different results as far as the shock transition is concerned. This possibly happens due to the fact that these potentials are primarily approximated and they tentatively mimic the space-time geometry around rotating black hole. In both panels, inner critical point ($x_{\rm in}$) and outer critical point ($x_{\rm out}$) are marked with filled circles and overall direction of the flow motion is indicated by arrows.

It is generally believed that in the context of understanding the black hole spectral properties [46] as well as jets and outflows [228, 248, 257, 258], shock induced

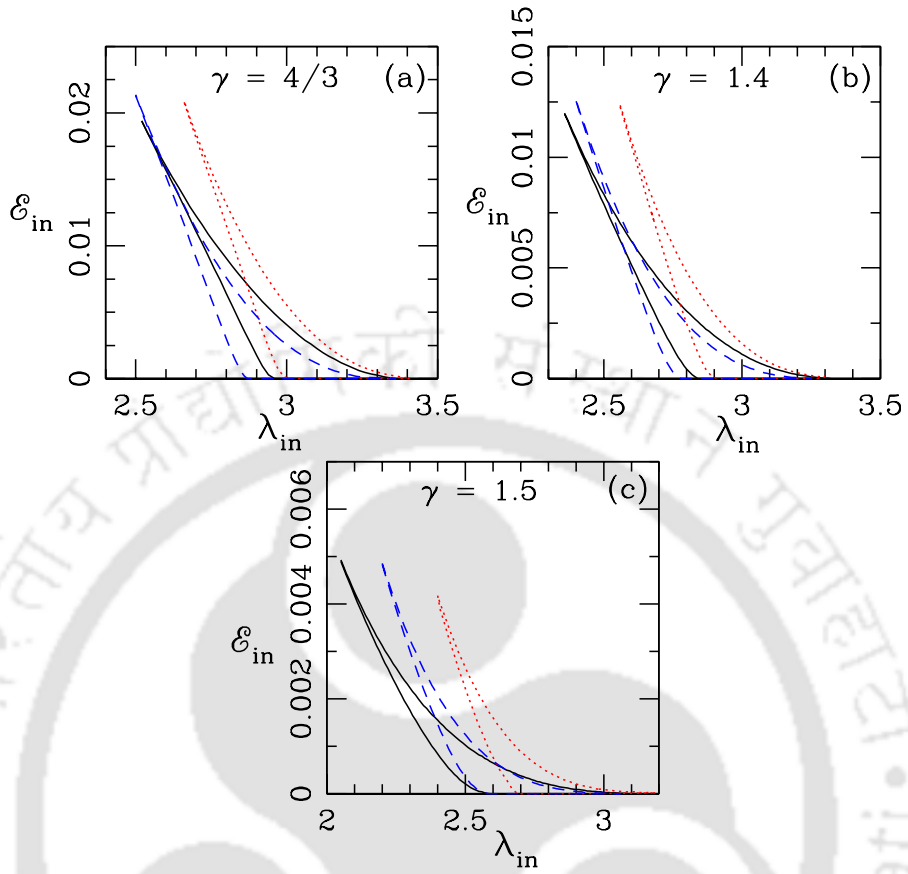

Figure 4.3: Comparison of shock parameter space in $\lambda_{in} - \mathcal{E}_{in}$ plane for different γ values. Region separated using solid, dotted and dashed curves are obtained for CM06, MU02 and ABN96 pseudo-Kerr potentials, respectively. Here, we consider $\alpha = 0$ and $a_k = 0.5$. In each panel, the value of γ is marked. See text for details.

global accretion solutions are potentially preferred over the shock free solutions. Therefore, it is worth identifying the range of flow parameters that admits shocks. Towards this, in Fig. 4.2, we obtain the shock parameter space spanned by the energy ($\mathcal{E}_{in}$) and angular momentum (λ_{in}) of the inviscid flow measured at the inner critical point (x_{in}). In the figure, we fix the spin values as $a_k = 0.0$ (a), 0.4 (b) and 0.8 (c), respectively and in each panel, region bounded by the solid, dotted and dashed curves are obtained for CM06, MU02 and ABN96 pseudo-Kerr potentials. As expected, in Fig. 4.2a, the shock parameter spaces for MU02 and ABN96 potentials are overlapped. This is obvious because MU02 and ABN96 potentials exactly reduce to same potential form for $a_k = 0.0$ as mentioned earlier. But, the shock parameter space for CM06 significantly differs from the same obtained for the remaining two potentials although a common overlapping region is found. In Fig. 4.2b, we choose

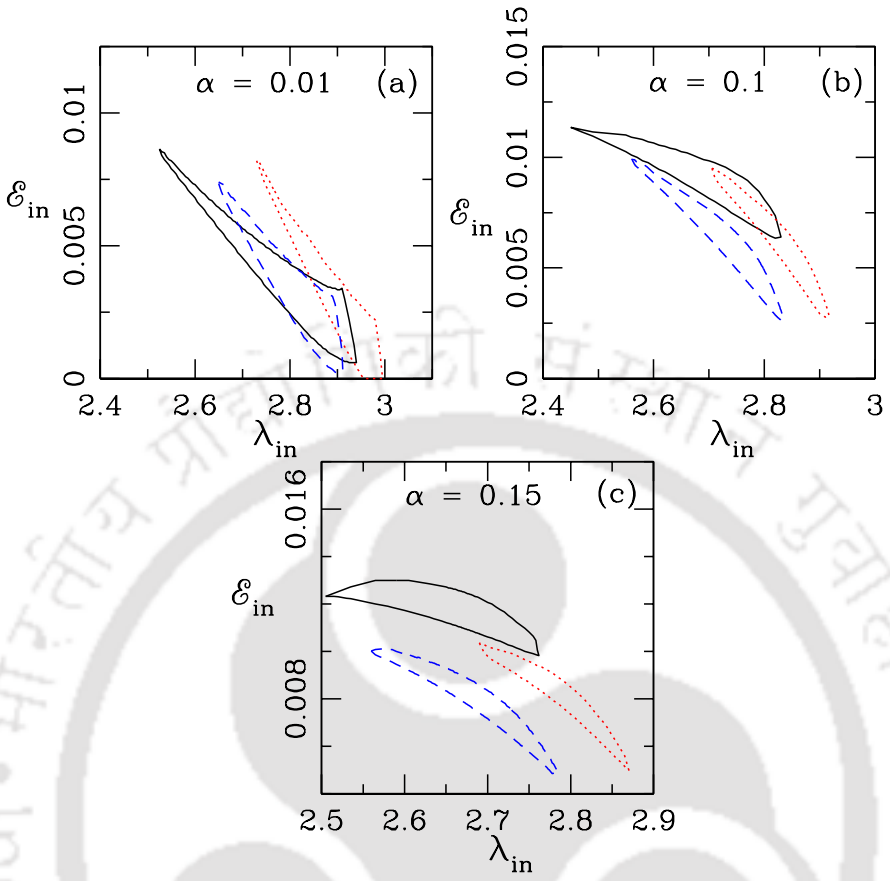

Figure 4.4: Modification of shock parameter space for dissipative accretion flow in $\lambda_{in} - \mathcal{E}_{in}$ plane. Effective region bounded with solid, dotted and dashed curves are calculated for CM06, MU02 and ABM96 pseudo-potential, respectively. Here, the results are obtained considering $a_k = 0.4$ and $\gamma = 1.4$. In each panel viscosity parameter is marked. See text for details.

$a_k = 0.4$ and observe that the shock parameter spaces deviate from each other for all the potentials. Interestingly, here also a common region among the parameter spaces is found. These common regions are particularly important to compare the accretion solutions among different adopted potentials (see Fig. 4.1). Moreover, we observe that the parameter spaces shift towards higher energy and lower angular momentum domain with the increase of black hole spin (a_k) for all the potentials. This apparently indicates that the accretion flow continues to sustain standing shock around rapidly rotating black holes provided its energy is relatively high. When the black hole spin is further increased as $a_k = 0.8$, shock parameter space for ABN96 is significantly shifted to the low angular momentum side and completely separated from the rest leaving any short of common overlapping region with others.

Until now, we have regarded the accreting matter to be adiabatic in nature and

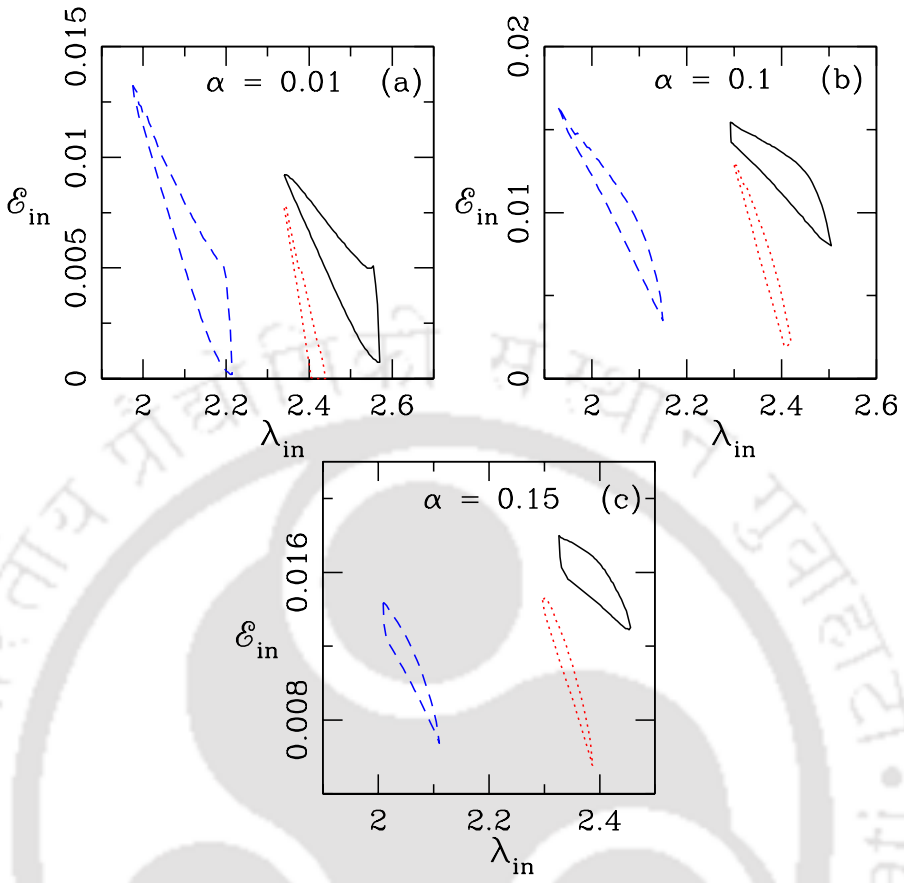

Figure 4.5: Same as Fig. 4.4 but black hole spin is chosen as $a_k = 0.8$.

the flow is characterized by an adiabatic index having a representative value $\gamma = 1.4$. However, in reality, the acceptable theoretical limit of the adiabatic index lies in the range $4/3 \leq \gamma \leq 5/3$ [5]. In order to understand the role of the γ values in deciding the global accretion solutions containing standing shock, we study the shock parameter space as function of γ for all the potentials. While doing this, the accretion flow is considered to be of three types, namely thermally ultra-relativistic ($\gamma \sim 4/3$), thermally trans-relativistic ($\gamma \sim 1.4$) and thermally semi-non-relativistic ($\gamma \sim 1.5$), respectively [169, 228] and obtain the shock parameter space as in Fig. 4.2. Here, we choose, $a_k = 0.5$ and $\alpha = 0$ and the obtained results are plotted in Fig. 4.3 where in each panel, solid, dotted and dashed curves represent the results corresponding to CM06, MU02 and ABN96 potentials. Also, γ values are marked in each panel. We find that for a given γ, the effective region of parameter spaces are different from each other for all the three potentials. In addition, we observe that as the γ value is increased, the shock parameter spaces shift towards the lower angular momentum and lower energy sides irrespective to the any chosen form of potential.

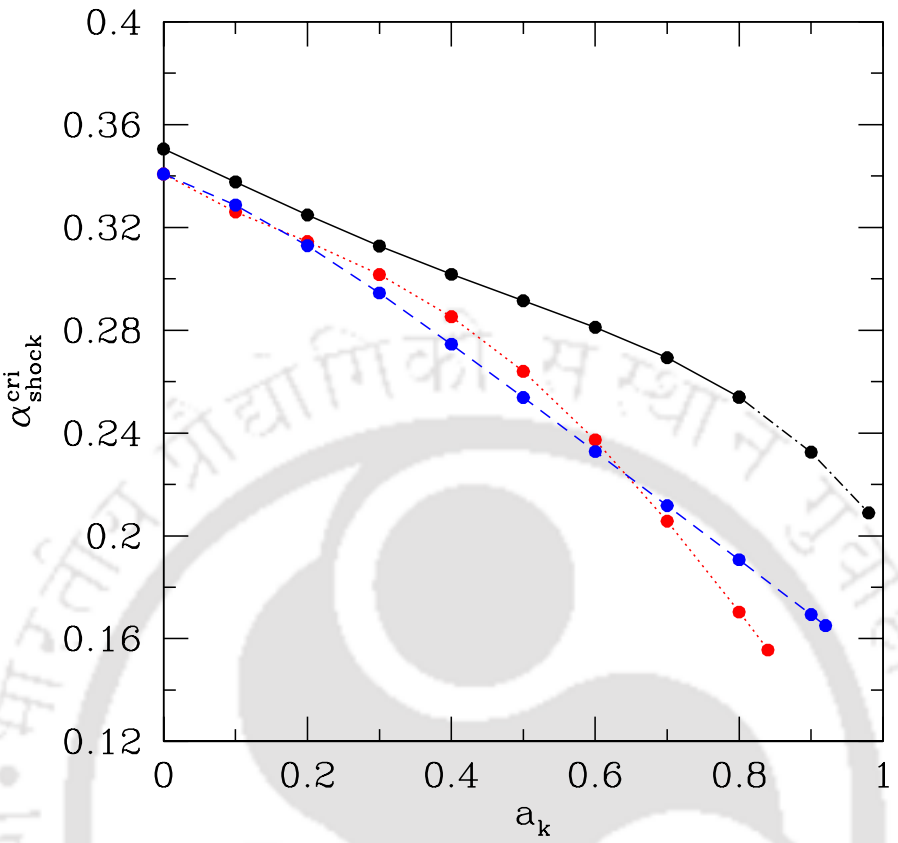

Figure 4.6: Variation of critical viscosity parameter ($\alpha_{\rm shock}$) for shock as function of black hole spin (a_k). Filled circles joined with solid, dotted and dashed lines represent results obtained using CM06, MU02 and ABN96 pseudo-potentials, respectively. For CM06, we extend the calculation of $\alpha^{\rm cri}_{\rm shock}$ beyond $a_k > 0.8$ to examine the overall trend and show the result using dot-dashed curve. Here, we choose $\gamma = 1.4$. See text for details.

What is more is that effective region of the parameter space is shrunk as γ value of increased. This essentially indicates that the possibility of shock formation is reduced when the flow moves towards non-relativistic limit [228].

So far, we have studied the shocked accretion solutions for non-dissipative flow. In our subsequent analysis, we relax this criteria and consider the viscous dissipation process to be active in the flow. With this, we calculate the standing shock parameter space for all the adopted potentials in terms of viscosity parameter (α) and display the results in Fig. 4.4 and Fig. 4.5. We choose $a_k = 0.4$ in Fig. 4.4 and $a_k = 0.8$ in Fig. 4.5 and in both figures, vary the viscosity parameter as $\alpha = 0.01$ (a), 0.1 (b) and 0.15 (c), respectively. In each panel, solid, dotted and dashed curves represent the results corresponding to CM06, MU02 and ABN96 potentials, respectively. Inside the disc, viscosity plays dual role; in one hand viscosity transports

angular momentum outward reducing its value at the inner edge and in the outer hand, viscous dissipation cause the heating of the flow as it accretes. Because of this, as viscosity is increased, standing shock parameter space is overall shifted towards the higher energy and lower angular momentum side for all the potentials. Moreover, the increase of α introduces enhanced viscous dissipation inside the flow and therefore, the possibility of shock formation is reduced [170, 232, 248] which is being realized as the effective region of the parameters space is shrunk when the value of the α parameter is increased. However, it is not possible to increase α indefinitely, because beyond a critical limit ($\alpha^{\rm cri}_{\rm shock}$), shock solutions disappears completely.

Further, we calculate the critical viscosity parameter ($\alpha^{\rm cri}_{\rm shock}$) that allows standing shock solutions and plot the variation of $\alpha^{\rm cri}_{\rm shock}$ with the spin parameter (a_k) for three different potentials, as depicted in Fig. 4.6. Here, filled circles connected by solid lines, dotted lines and dashed lines are for CM06, MU02 and ABN96 potentials, respectively. While calculating $\alpha^{\rm cri}_{\rm shock}$ for a fixed a_k, we freely vary the flow parameters, namely $x_{\rm in}$, $\mathcal{E}_{\rm in}$ and $\lambda_{\rm in}$, respectively. Usually, in the weak viscosity limit, the sub-Keplerian flow joins with Keplerian disc quite far away from black hole. Hence, the possibility of finding standing shock which requires the existence of multiple critical points increases at the lower viscosity range. On the contrary, when $\alpha > \alpha^{\rm cri}_{\rm shock}$, Keplerian disc approaches very close to the black hole resulting the flow to pass through the inner critical point only [230] without having a shock. We find that $\alpha^{\rm cri}_{\rm shock}$ is anti-correlated with a_k for all the potentials. Note that we calculate shock solutions for CM06 potential considering rapidly rotating black hole ($a_k \to 0.98$) as well, although this potential bears limitation to mimic the Kerr geometry satisfactorily for $a_k > 0.8$. Certainly, this introduces error in our calculation, however, it provides us the overall trend of $\alpha^{\rm cri}_{\rm shock}$ variation towards the highest value of a_k. In case of MU02 and ABN96 potentials, no such restriction is imposed on the upper limit of a_k values. But, we do not find standing shock solutions beyond $a_k > 0.84$ for MU02 and $a_k > 0.92$ for ABN96 potentials, respectively. In addition, we observe that $\alpha^{\rm cri}_{\rm shock}$ obtained from different potentials possesses close by values for weakly rotating black holes and it starts deviating from each other with the increase of a_k.

4.2.2 Estimation of maximum outflow rates

So far, we have performed a comparative study for the accretion flows using pseudo-Kerr potentials ignoring any mass loss from the disk. But, due to the shock transi-

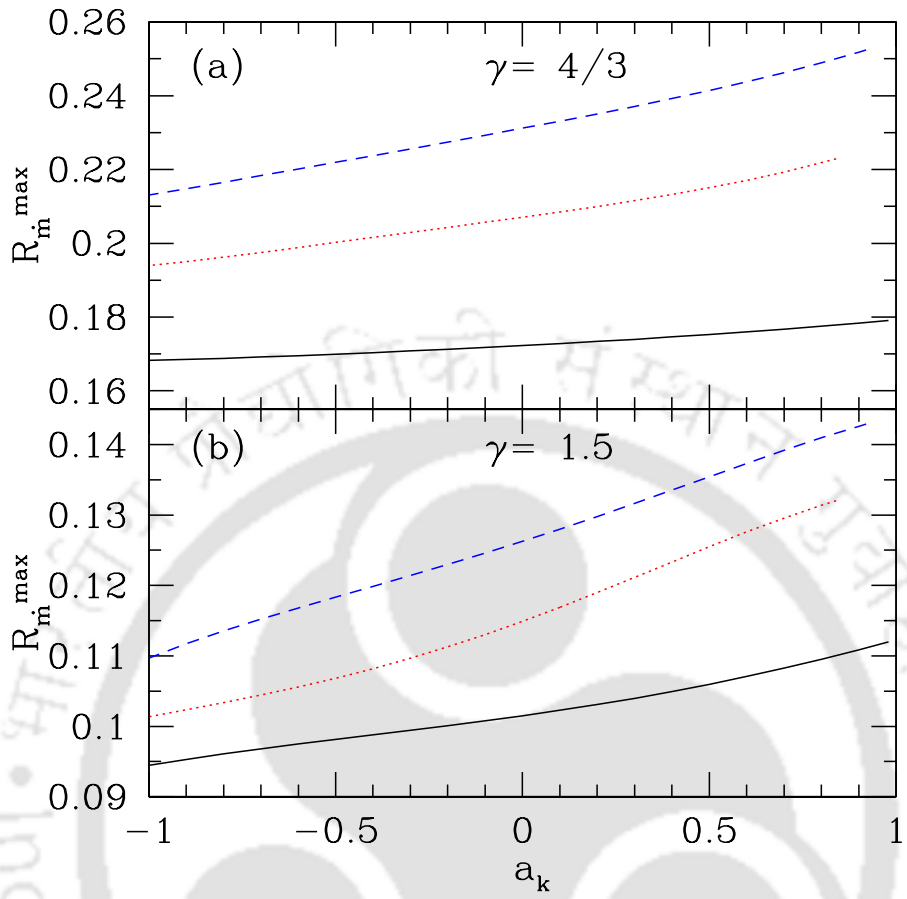

Figure 4.7: Variation of maximum outflow rates $R_{\dot{m}}^{\max}$ with the black hole spin a_k. Upper panel (a): for $\gamma = 4/3$ and lower panel (b): for $\gamma = 1.5$, respectively. Solid, dotted and dashed curves are calculated for CM06, MU02 and ABM96 pseudo-potentials, respectively. Here, viscosity parameter is chosen as $\alpha = 0.05$. See text for details.

tion, a part of the inflowing matter emerges out from the disk as outflow. Rigorous investigations including mass loss from the disk have been already performed by Aktar et al. (2015, 2017, 2018) [228, 248, 256] using pseudo-Kerr potential. So, here we only perform a comparative study in terms of maximum outflow rates ($R_{\dot{m}}^{\max}$) with the variation of spin (a_k) using pseudo-Kerr potentials to avoid repetitions. We also extend the calculations upto the allowed ranges of spin for standing shock and estimate maximum outflow rates ($R_{\dot{m}}^{\max}$) for all the potentials. However, it introduces error in the calculation of $R_{\dot{m}}^{\max}$ in the higher ranges of spin. For this analysis, we consider the flow to be inviscid i.e., $\alpha = 0$.

Based on our accretion-ejection model, we self-consistently calculate mass outflow rates ($R_{\dot{m}}$) by supplying inflow parameters, namely flow energy ($\mathcal{E}_{in}$), flow angular momentum (λ_{in}), viscosity parameters (α), adiabatic index (γ) and spin

(a_k) of the black hole. While calculating $R_{\dot{m}}^{\max}$, we freely vary all the inflow parameters and calculate the maximum outflow rates for a particular a_k [228, 248]. In Fig. 4.7, we present $R_{\dot{m}}^{\max}$ with the variation of spin a_k for inviscid case $\alpha = 0$. Here, we choose the two extreme allowed theoretical limit of adiabatic index i.e., thermally ultra-relativistic ($\gamma = 4/3$) (upper panel (a)) and thermally semi-non-relativistic ($\gamma = 1.5$) (lower panel (b)). We observe that $R_{\dot{m}}^{\max}$ is weakly correlated with the spin a_k of the black hole for all the potentials [228]. This result indicates that the strong correlation between jet and spin is still illusive from our accretion-ejection model. Also, we observe that the ultra-relativistic ($\gamma = 4/3$) flows produce more outflows compared to the semi-non-relativistic ($\gamma = 1.5$) flows as far as maximum outflow rates are concerned. This is due to the fact that the outflows are purely thermally driven in our model. We find that $R_{\dot{m}}^{\max}$ value lies (9-18)%, (10-22)% and (11-25)% within the whole allowed range of spin (a_k) and adiabatic index (γ) for CM06, MU02 and ABN96 potentials, respectively. It may also be noted that ABN96 pseudo potential effectively provides more $R_{\dot{m}}^{\max}$ compared to other two potentials. Moreover, we observe that $R_{\dot{m}}^{\max}$ depends on a_k very weakly for all the potentials. With this findings, we argue that the correlation between black hole spin and powering jets seems to be feeble. It may be noted that the value of $R_{\dot{m}}^{\max}$ allows us to compute the kinetic jet power ($L_{\rm jet}^{\rm est}$) for black hole sources [228, 259].

In the next section, we apply our accretion-ejection formalism to estimate the kinetic jet power and attempt to explain the observed radio jet power in the low-hard state of black hole XRBs.

4.3 Astrophysical Application

4.3.1 X-ray and radio correlation of XRBs

Fender et al. (2005, 2009) [59, 260] reported the existence of radio-X-ray correlation in the low-hard states of the XRBs. Interestingly, most of the XRBs follow a universal non-linear correlation, namely $F_R \propto F_X^b$, where $b \sim 0.5 - 0.7$ and F_R and F_X denotes radio and X-ray fluxes, respectively [4, 174, 261–263]. However, a growing number of sources e.g., H1743-322, Swift 1753.3-0127, XTE J1650-500,

XTE J1752-223 are found to lie well outside the universal radio-X-ray correlation [87–92, 264] following an outliers track. These sources follow a steeper correlation as $b \sim 1.4$ [88].

4.3.2 Kinetic jet power of steady-compact jets: theory and observation

In this section, we compare the theoretically obtained kinetic jet power with observations. While doing that we convert the observed radio luminosity to jet power. The empirical relation between radio luminosity and jet power is computed considering a simple conical jet model of optically thick jet as [265–267],

$$L_R \propto L_{\rm jet}^{17/12}, \tag{4.19}$$

where $L_R (= 4\pi d^2 F_R)$ is the radio luminosity measured at frequency ν, F_R is the radio flux measured at frequency ν and d is the distance of the source, respectively. Later, Heinz & Grimm (2005) [268] identifies a relation between the jet power and radio luminosity for Cyg X-1 and GRS 1915+105 considering the normalization factor $\sim 6.1 \times 10^{-23}$ [264] as,

$$L_{\rm jet} = 4.79 \times 10^{15} L_R^{12/17} \text{ erg s}^{-1}, \tag{4.20}$$

In the low-hard states, the jets are not relativistically boosted and thus we ignore Doppler correction while estimating jet power [263]. In the present analysis, we employ equation (4.20) to estimate the kinetic jet power from radio luminosity for all the sources under consideration. We also calculate the accretion power by using X-ray luminosity (L_X) as $\dot{M}_{\rm in} c^2 = L_X/\eta_{\rm acc}$, where $\eta_{\rm acc}$ is the accretion efficiency factor and $L_X = 4\pi d^2 F_X$, F_X being the X-ray flux. We obtain F_X (1-10 keV) and L_R (8.6 GHz) fluxes for the various sources from Corbel et al. (2013) [4], references therein) and plotted in Fig. 4.8. The different symbols and colors represent the different sources. It is noteworthy that the spin value of some of the selected sources is not yet settled. Hence, for simplicity, we choose $\eta_{\rm acc} \sim 0.15$ while calculating the accretion power for all the selected sources [5, 6], presented in Fig. 4.8.

Employing our accretion-ejection model formalism, we compute the maximum kinetic jet power [228] as,

$$L_{\rm jet}^{\rm max} = \eta_{\rm jet} \times R_{\dot{m}}^{\rm max} \times \dot{M}_{\rm in} \times c^2 \text{ erg s}^{-1}, \tag{4.21}$$

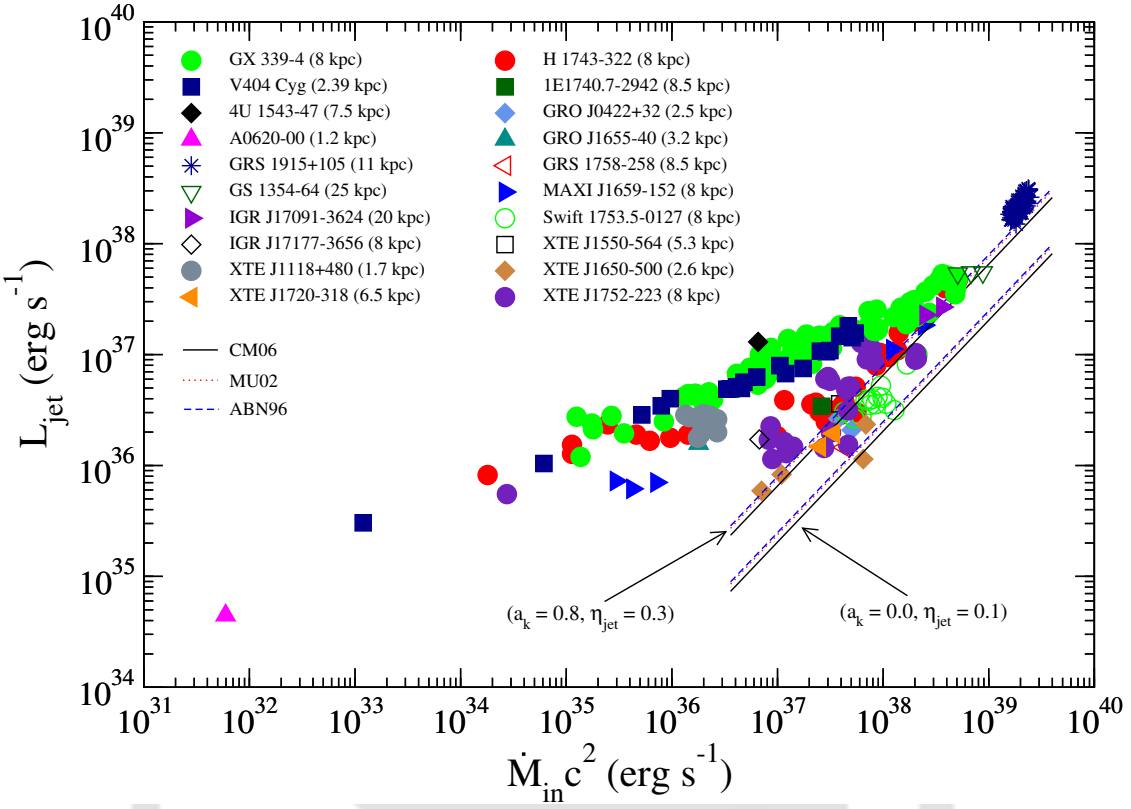

Figure 4.8: Comparison of observed and theoretical kinetic jet power as a function of accretion power. The different symbols and colors represent the data of low-hard state of 20 black hole XRBs which are taken from Corbel et al. (2013) [4]. Length scale mentioned within the parenthesis indicates the distance of the source. The corresponding solid, dotted and dashed lines represent the maximum kinetic jet power from theoretical model for CM06, MU02 and ABN96 potentials, respectively. See the text for details.

where, $R_{\dot{m}}^{\max}$ is the maximum outflow rates and $\eta_{\rm jet}$ is the jet efficiency factor. For the purpose of representation, we choose $\alpha = 0.05$ and $\gamma = 4/3$ and calculate $R_{\dot{m}}^{\max}$ for non-rotating ($a_k = 0.0$) and rapidly rotating ($a_k = 0.8$) black holes, respectively (see Fig. 4.7). In this analysis, we consciously restrict ourselves to choose $a_k \leq 0.8$, as one of the adopted potential (CM06) fails to describe space-time geometry satisfactorily above this limiting range of spin value.

We compare our theoretical results (equation 4.21) with observation (equation 4.20) which is shown in Fig. 4.8. The solid, dotted and dashed curves represent the theoretically obtained kinetic jet power ($L_{\rm jet}^{\max}$) for CM06, MU02 and ABN96 potentials, respectively where the lower curves are for non-rotating black holes ($\eta_{\rm jet} = 0.1$) and the upper curves are for rapidly rotating black holes ($\eta_{\rm jet} = 0.3$), as depicted in Fig. 4.8. For $a_k = 0.0$, maximum outflow rates are computed as $R_{\dot{m}}^{\max} = 0.2037$ (CM06), 0.2373 (MU02) and 0.2481 (ABN96) whereas $R_{\dot{m}}^{\max} = 0.2175$ (CM06),

0.2519 (MU02), 0.2645 (ABN96) for $a_k = 0.8$, respectively. It is clear that $L_{\rm jet}^{\rm max}$ roughly remains insensitive on the choice of potential. And, finally we observe that the 'outliers' track ([4], references therein) agrees quite consistently with the model predictions for rapidly rotating black holes.

4.4 Chapter Conclusion

In this work, we present a comparative study of the global accretion solutions including shock wave by adopting three pseudo-Kerr potentials prescribed by Artemova et al. (1996) [144], Mukhopadhyay (2002) [145] and Chakrabarti & Mondal (2006) [146]. These potentials are known to describe the space-time geometry of rotating black holes quite satisfactorily. The advantage of using pseudo-Kerr potentials in lieu of the general theory of relativity (GTR) is that it allows us to investigate the accretion flow properties following the Newtonian approach (i.e. avoiding the rigorous mathematical complexity of GTR) while retaining all the salient features of complex space time geometry around a rotating black hole. Accordngly, utilizing these potentials, we present the generalized governing equations that describe the dissipative accretion flow around the rotating black hole. We then simultaneously solve these equations to obtain the global transonic accretion solutions and employing the Rankine-Hugoniot shock conditions, we further obtain the shock induced global accretion solutions around a rotating black hole. We summarize the results below.

We find that standing shock continues to form in all the adopted pseudo-Kerr potentials (see Fig. 4.1). We also observe that shocked solutions are not the discrete solutions, instead a wide range of flow parameters admits shock transition in the accretion flow variables. In this context, we identify the effective region of the parameter space spanned by the energy ($\mathcal{E}_{\rm in}$) and the angular momentum($\lambda_{\rm in}$) of the flow measured at the inner critical points that allows standing shock solutions and find that shock forms around weakly rotating as well as rapidly rotating black holes (see Fig. 4.2). Further, we examine the role of adiabatic index (γ) in determining the shock solutions and notice that the shock parameter space is squeezed when γ is tending to the thermally non-relativistic limit (see Fig. 4.3). This provides a hint that the formation of standing shock is more likely for flows with lower γ values.

We continue the study of shock parameter space considering dissipative accretion flow and compare the parameter space in terms of viscosity parameter (α). We find that parameter space is gradually modified and shrunk with the increase of

α for all the pseudo potentials (see Fig. 4.4-4.5). This evidently indicates that the possibility of shock formation is reduced as the viscous dissipation is enhanced. Beyond a critical limit ($\alpha > \alpha^{\rm cri}_{\rm shock}$), accretion flow fails to satisfy the standing shock conditions and therefore, shock disappears completely. Needless to say that $\alpha^{\rm cri}_{\rm shock}$ does not bear any universal value, but depends on the other input parameters (see Fig. 4.6). In case of weakly rotating black holes, $\alpha^{\rm cri}_{\rm shock}$ for all the pseudo-potentials agrees quite well, but differs considerably for rapidly rotating black holes. Hence, we argue that as far as the standing shock is concerned, qualitatively all the pseudo-potentials behave quite similarly, but they differ quantitatively from each other when the non-linear effects of space-time geometry becomes substantial. Moreover, we realize that CM06 potential provides standing shock solutions for $a_k \rightarrow 0.98$ although this potential yeilds erroneous results for $a_k \leq 0.8$ as it fails to describe the space-time geometry beyond this limit. In comparison, we do not find standing shock solutions beyond $a_k > 0.84$ for MU02 and $a_k > 0.92$ for ABN96 potentials (see Fig. 4.6).

We further compare the maximum outflow rates ($R^{\rm max}_{\dot{m}}$) in terms of the black hole spin (a_k) for all the adopted pseudo potentials considering viscous accretion flow ($\alpha = 0.05$). We find that there exist a feeble correlation between $R^{\rm max}_{\dot{m}}$ and spin a_k irrespective to the choice of potentials although potential ABN96 provides more $R^{\rm max}_{\dot{m}}$ compared to the other potentials (Fig. 4.7).

We apply our accretion-ejection model to explain the 'outliers' track of the radio-X-ray correlations in black hole XRBs. We select sources in their low-hard states from Corbel et al. (2013) [4]. We find that theoretical results obtained for the rapidly rotating black holes are in agreement with the observational findings of black hole XRBs lying along the 'outliers' track (see Fig. 4.8).

Chapter 5

Numerical Study of High Frequency Quasi-periodic Oscillations (HFQPOs) around rotating black holes

In order to examine the accretion flow properties around compact objects, numerous studies have been carried out based on analytical models, starting from Bondi [9]. Unfortunately, the scope and applicability of analytical studies are very much limited as they are restricted to the realm of steady-state solutions only. However, in reality, the astrophysical objects never remain in the steady-state as fluctuations and/or variabilities in the flow properties and in the emergent radiations are always present. One such best-known variability is the Quasi-periodic Oscillations (QPOs) seen in the power density spectrum (PDS) of X-ray variabilities of various astrophysical sources. QPOs are commonly observed in compact object systems such as black hole X-ray binaries (BH-XRBs) [49, 105, 115], neutron star (NS) [106–108], cataclysmic variables (CVs) [109, 269], active galactic nuclei (AGN) [113, 114] and Ultralumious X-ray sources (ULXs) [111, 270, 271, and references therein]. For black hole binaries, the QPO frequency lies in a wide range of frequencies $0.1 - 450$ Hz and that has been divided in general into two categories: (a) low-frequency QPOs (LFQPOs) in the range $0.1 - 30$ Hz and (b) high-frequency QPOs (HFQPOs) in the range $40 - 450$ Hz [105]. The origin of HFQPOs is of great interest as these oscillations are transient as well as subtle. Moreover, it is believed that the HFQPOs possibly the manifestations of various relativistic effects in the orbits close to the black hole and it can be used as an important tool to probe general relativity in the strong

gravitational field limit [272–274]. However, conclusive consensus on the origin of HFQPOs is not settled yet. In this chapter, we carry out the study the HFQPOs by numerical means and make an effort to comment on the mass and spin of the well known Galactic black hole source GRS $1915+105$.

5.1 Model Description

We begin with a non-steady, two-dimensional, axisymmetric, inviscid accretion flow around a rotating black hole. In order to describe the space-time geometry around the rotating black hole, we adopt a pseudo potential proposed by Artemova et al. (1996) [144]. In addition, we assume the disc to be optically thin and accordingly, we neglect the radiation pressure in our model [155]. As before, here also we use the unit system as $G = M_{\rm BH} = c = 1$, where G, $M_{\rm BH}$ and c are the gravitational constant, mass of the black hole and the speed of light, respectively. In this unit system, length, angular momentum and time are expressed in units of r_g $(= GM_{\rm BH}/c^2)$, λ_g $(= GM_{\rm BH}/c)$ and t_g $(= GM_{\rm BH}/c^3)$, respectively. Using them, the governing equations are made dimensionless.

5.1.1 Governing Equations

We choose cylindrical coordinate system (r, z, ϕ) to write down the conservation equations for mass, momentum and gas energy as given by [e.g., 155, 156, 166, and references therein],

(i) The mass conservation equation:

$$\frac{\partial \rho}{\partial t} + \nabla.(\rho \boldsymbol{v}) = 0, \tag{5.1}$$

(ii) The three components of momentum conservation equations are given by,

$$\frac{\partial(\rho v_r)}{\partial t} + \nabla \cdot (\rho v_r \boldsymbol{v}) = \frac{\rho \boldsymbol{v}_\phi^2}{r} - \frac{\partial P}{\partial r} + \rho g_r, \tag{5.2}$$

$$\frac{\partial(\rho v_z)}{\partial t} + \nabla \cdot (\rho v_z \boldsymbol{v}) = -\frac{\partial P}{\partial z} + \rho g_z, \tag{5.3}$$

$$\frac{\partial(\rho v_\phi)}{\partial t} + \nabla \cdot (\rho v_\phi \boldsymbol{v}) = 0, \tag{5.4}$$

and

(iii) The conservation of gas-energy equation:

$$\frac{\partial \varepsilon}{\partial t} + \nabla \cdot (\varepsilon \boldsymbol{v}) = -P\nabla.\boldsymbol{v} - \Lambda, \tag{5.5}$$

where ρ is the density, $\boldsymbol{v}$ $[= (v_r, v_z, v_\phi)]$ are the three velocity, P is the gas pressure and ε is the the internal energy of the gas per unit volume, respectively. The total gas-energy density is sum of internal energy density ($\rho\varepsilon$) and kinetic energy density ($\frac{1}{2}\rho v^2$). The relation between gas pressure P and specific internal energy ε is obtained from equation of ideal gas as $P = (\gamma-1)\rho\varepsilon = R_G\rho T/\mu$, where γ, R_G, μ and T are the adiabatic index, gas constant, mean molecular weight and temperature of the gas, respectively. In addition, optical thin losses is included using the quantity Λ which represents the rate of cooling of the gas per unit volume and in general a function of density and temperature. In this work, we consider only the free-free emission i.e., Bremsstrahlung as account for cooling/heating mechanism in the flow. Here, g_r and g_z denote the radial and vertical components of gravitational force $\boldsymbol{g}$ which are given by,

$$g_r = \frac{1}{R^{2-\beta}(R-R_{\rm H})^\beta}\frac{r}{R} \quad \text{and} \quad g_z = \frac{1}{R^{2-\beta}(R-R_{\rm H})^\beta}\frac{z}{R}, \tag{5.6}$$

where $R = \sqrt{r^2+z^2}$, $R_{\rm H}$ referes the event horizon calculated as $R_{\rm H} = 1+\sqrt{(1-a_k^2)}$ [275] and a_k being the spin of the black hole. Moreover, the exponent β is defined as $\beta = \frac{R_{\rm ISCO}}{R_{\rm H}} - 1$ and $R_{\rm ISCO}$ represents the innermost stable circular orbit which is determined as [142],

$$R_{\rm ISCO} = 3 + Z_2 \mp [(3-Z_1)(3+Z_1+2Z_2)]^{1/2}, \tag{5.7}$$

where $Z_1 = 1+(1-a_k^2)^{1/3}[(1+a_k)^{1/3}+(1-a_k)^{1/3}]$ and $Z_2 = (3a_k^2+Z_1^2)^{1/2}$. In equation (5.7), '$\mp$' sign stands for prograde and retrograde flow motions, respectively.

5.1.2 Simulation set up and Model parameters

We numerically solve the time-dependent equations (5.1-5.5) using the finite-difference scheme under initial and boundary conditions [156–158]. We choose a set of outer boundary parameters, namely radial velocity ($v_{\rm out}$), sound speed ($a_{\rm out}$), angular momentum (λ) and outer boundary radius ($r_{\rm out}$) that admits the non-steady shock transition in the vicinity of the black hole. Because of shock, PSC [125] reprocessed

Table 5.1: Model parameters and flow variables at the outer boundary radius $r_{\rm out} = 100$ including simulation results. Here, adiabatic index is chosen as $\gamma = 4/3$ for all the cases.

Model	Input parameters					Simulation results		
	λ ($GM_{\rm BH}/c$)	$\mathcal{E}$ (c^2)	a_k	$v_{\rm out}$ (c)	$a_{\rm out}$ (c)	$r_s^{\rm min}$ ($GM_{\rm BH}/c^2$)	$r_s^{\rm max}$ ($GM_{\rm BH}/c^2$)	$\nu^*_{\rm QPO}$ Hz
A	1.99	0.0010	0.92	-0.10174438	0.04344868	9.50	11.00	61.97 ± 0.26
B	1.97	0.0010	0.93	-0.10171432	0.04343855	9.75	11.00	62.45 ± 1.42
C	2.02	0.0012	0.91	-0.09852830	0.04536424	10.00	11.75	61.29 ± 0.19
D	1.96	0.0012	0.93	-0.09857870	0.04535299	9.50	11.50	60.28 ± 1.48
E	1.98	0.0013	0.93	-0.09716838	0.04624567	10.25	11.75	63.06 ± 1.39
F	1.98	0.0010	0.94	-0.10160294	0.04342799	10.50	10.75	No QPO

$^*\nu_{\rm QPO}$ is calculated using $M_{\rm BH} = 10M_\odot$.

the soft photons from the pre-shock disc via inverse Comptonized process to produce high energy radiations [35]. Interestingly, when PSC modulates, emitted radiations from PSC are also expected to oscillate which clearly indicates that QPOs seem to be originated due to the undulation of PSC itself [125, 234]. In this work, we choose six sets of boundary parameters based on the analytical study of 1.5D accretion flow [248, and references therein] and depicted them in Table 5.1 where Model name, angular momentum (λ), energy ($\mathcal{E}$) and spin of the black hole (a_k) are presented in column 1-4. In column 5 and 6, we mention the associated radial velocity ($v_{\rm out}$) and sound speed ($a_{\rm out}$) at the outer boundary $r_{\rm out} = 100$, respectively. Here, we consider mass of the black hole as $M_{\rm BH} = 10M_\odot$, the adiabatic index as $\gamma = 4/3$ [169, 228] and the mass accretion rate as $\dot{M} = 1.3 \times 10^{18}$ g sec^{-1} all throughout, unless otherwise stated.

5.2 Simulation Results

In Fig. 5.1, we show the four snapshots of velocity field vectors along with density contours in $r - z$ plane within a single shock oscillation period for Model E. In each panel, we zoom the inner part of the 2D disc up to $30r_g$ for better clarity where the velocity vectors are depicted by solid black arrows and the density contours drawn in logarithmic scale as log ρ (g cm^{-3}). Here, color coded bar represents the range of density. A sharp color contrasting contour meeting the equatorial plane indicates the shock location (r_s) at the equatorial plane. We calculate the shock location at equatorial plane within a single shock oscillation period as (a) $r_s \sim 10.25r_g$ ($t = 2.026 \times 10^4 t_g$), (b) $r_s \sim 11.00r_g$ ($t = 2.039 \times 10^4 t_g$), (c) $r_s \sim 10.25r_g$ ($t = 2.065 \times 10^4 t_g$) and (d) $r_s \sim 11.00r_g$ ($t = 2.073 \times 10^4 t_g$), respectively. Here, we

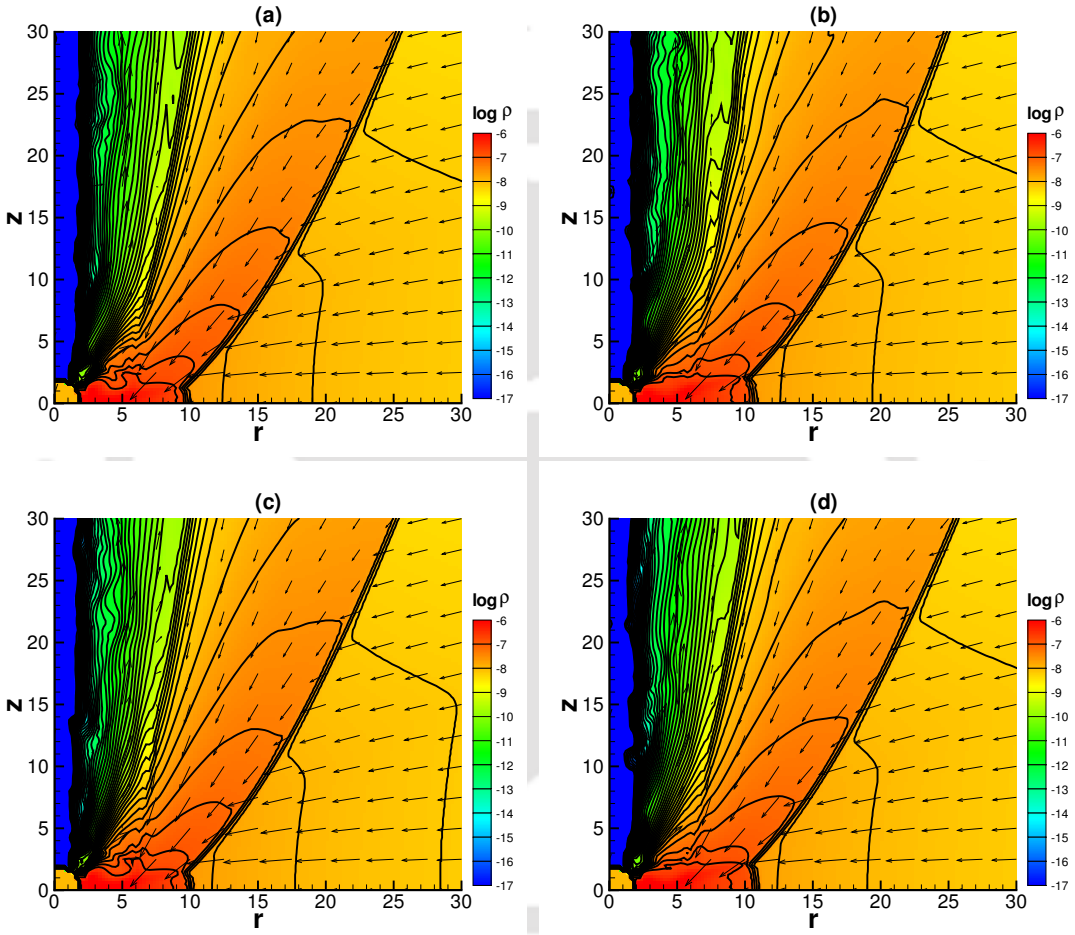

Figure 5.1: Density contours of $\log \rho$ (g cm^{-3}) and velocity vectors in $(r - z)$ plane at different time within a single oscillation period for Model E. The shock locations (r_s) at the equatorial plane are (a): $r_s \sim 10.25$, (b): $r_s \sim 11.00$, (c): $r_s \sim 10.25$ and (d): $r_s \sim 11.00$ indicate the size of PSC regions. See text for details.

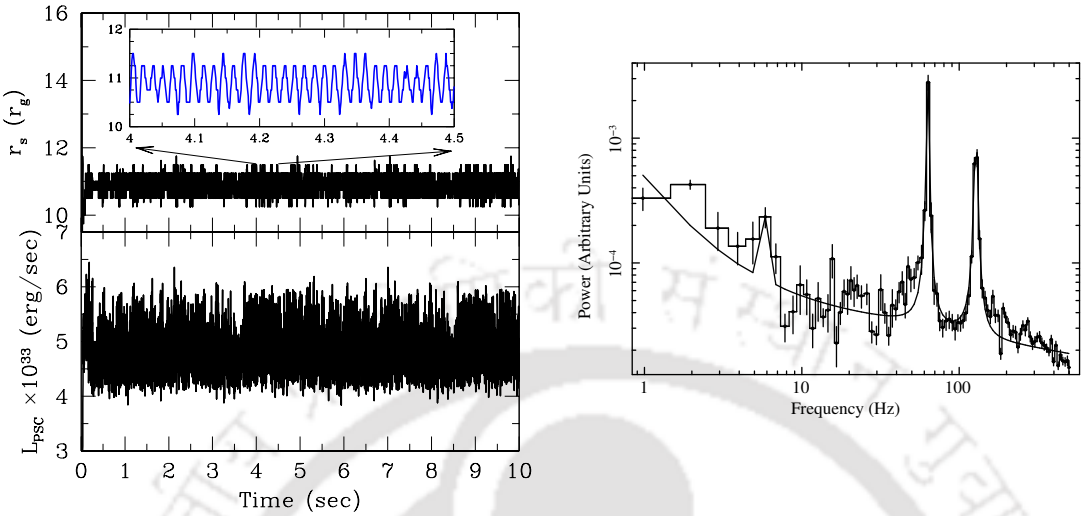

Figure 5.2: Left: Variation of shock location (r_s) at the equatorial plane (*upper panel*) and PSC luminosity ($L_{\rm PSC}$) (*lower panel*) with time for Model E. **Right**: Power density spectrum of $L_{\rm PSC}$ is shown. Fundamental QPO frequency is obtained at $\sim 63.06 \pm 1.39$ Hz. See text for details.

find that shock forms close to the horizon and the density profile of PSC increases sharply.

In Fig. 5.2(**Left**: *upper panel*), we show the over all variation of the shock location (r_s) at the disc equatorial plane for Model E. A very fast however persistent oscillation is observed which seems to be quasi-periodic in nature. Also, the amplitude of the shock oscillation remains limited within the range of $10.25 \leq r_s \leq 11.75$ [see Figure 5.1(a-d)]. Moreover, as most of the high energy radiation is likely to be emitted from the PSC region, we calculate the PSC luminosity ($L_{\rm PSC}$) due to bremsstrahlung emission and show its time variation in Fig. 5.2(**Left:** *lower panel*) where persistent non-steady variation is clearly observed. To examine the quasi-periodic nature of the emitted radiations, we calculate the power density spectrum (PDS) of $L_{\rm PSC}$ and present the result in Fig. 5.2(**Right**). We find that quasi-periodic variation of $L_{\rm PSC}$ is characterized by the fundamental frequency $\nu_{\rm QPO} = 63.06 \pm 1.39$ Hz along with harmonics at 127.8 ± 3.78 Hz. We carry out simulation study for all the remaining Models and the obtained results, namely minimum ($r_s^{\rm min}$) and maximum ($r_s^{\rm max}$) positions of the shock variation and corresponding $\nu_{\rm QPO}$ are tabulated in Table 5.1. We observe that remaining Models admit either steady (Model F) or non-steady shock solutions (Model A to Model E). For the shake of completeness, we show the results corresponding to Model F in Fig. 5.3. The variation of (r_s) and $L_{\rm PSC}$ are shown in Fig. 5.3(**Left**: *upper panel*) and 5.3(**Left**: *lower panel*). The

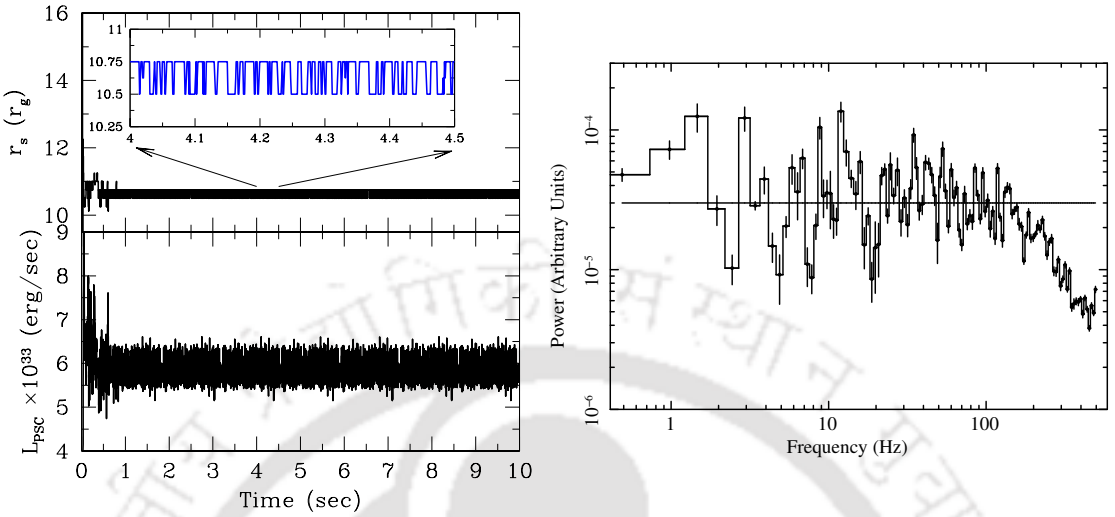

Figure 5.3: Left: Variation of shock location (r_s) at the equatorial plane (*upper panel*) and PSC luminosity ($L_{\rm PSC}$) (*lower panel*) for Model F. **Right**: Power density spectrum of $L_{\rm PSC}$ is shown. No signature of HFQPOs is seen in PDS. See text for details.

PDS of $L_{\rm PSC}$ are depicted in Fig. 5.3(**Right**) where signature of HFQPO features is not seen.

5.3 Application to GRS 1915+105

In this section, we apply our numerical findings on the observational detection of HFQPO from well studied Galactic black hole source GRS 1915+105, in which minimum HFQPO ($65-67$ Hz) [130] has been observed. Since its detection [276], GRS 1915+105 remains active in X-rays and is known to exhibit X-ray variability [[226] and references therein]. In an earlier effort, Greiner et al. (2001) [221] first estimated the mass of the source to be $M_{\rm BH} = 14 \pm 4 M_\odot$ considering the orbital period ~ 33.5 days. Recently, Steeghs et al. (2013) [277] inferred more accurate mass estimation of $M_{\rm BH} = 10.1 \pm 0.6 M_\odot$ based on precise orbital period of $\sim 33.85 \pm 0.16$ days. In parallel, several attempts have been made to calculate the spin of the source and the measured spin values is reported as $a_k = 0.98^{+0.01}_{-0.01}$ [225, 278].

In order to explain the HFQPOs observed in GRS 1915+105, several group of workers proposed various models. Morgan et. al. (1997) [130] first proposed that HFQPOs perhaps be associated with the Keplerian frequency at the inner-most stable circular orbit. Cui et. al. (1998) [279] discussed that HFQPOs could be

originated due to the relativistic Lense-Thirring precession of the orbits and they also predicted the source to be a highly spinning black hole. Nowak et. al. (1997) [280] proposed a model based on diskoseismic g-modes of oscillation for explaining the HFQPOs of the source. It is noteworthy to mention that these models do not show the consequence of accretion flow dynamics coupled with general relativistic effects around a rotating black holes.

In the next section, we use recently observed data from Large Area X-ray Proportional Counter (LAXPC) onboard India's first multi-wavelength astronomical observatory *AstroSat* [281] in order to constrain the spin of GRS 1915+105. Needless to mention that LAXPC has better detection capability above 10 keV compared to PCA instrument onboard *RXTE*.

5.3.1 Observation and Data Reduction

The source GRS 1915+105 has been observed during the period of June 11, 2016 (MJD 57550) to June 15, 2016 (MJD 57554) using Guaranteed Time (GT) of *LAXPC/AstroSat* for 100 ks. LAXPC consists of three proportional counters (LAXPC10, LAXPC20 and LAXPC30) [282] operating in the energy range $3.0 - 80.0$ keV with a high temporal resolution of 10 μs [283]. The combined effective area of the three units is $\sim 6000\ cm^2$ at 15 keV [284].

We use the analysis software available at the IUCAA science support cell page. Following the extraction and analysis procedures described in [285], we generate the background subtracted lightcurve with a time resolution of 16 sec in the energy band of $3 - 60$ keV as well as the energy spectrum in the energy range of $3 - 50$ keV. For present study, we use results only from the LAXPC10 using the observation carried out on MJD 57551 (Orbit 3819) with an exposure of 1590 sec. Detailed analysis of guaranteed time observation with ~ 100 ks exposure is under progress and will be presented elsewhere.

5.3.2 Analysis and Modeling

The background subtracted lightcurve for the specified observation (Orbit 3819) on MJD 57551 is shown in Figure 5.4a. The corresponding color-color diagram (CCD) is also included in the inset of the same Figure. The CCD is the variation of HR1=B/A vs HR2=C/A, where A, B, C are the count rates in the $3 - 6$ keV,

http://astrosat-ssc.iucaa.in/?q=data_and_analysis
https://astrobrowse.issdc.gov.in/astro_archive/archive/Home.jsp

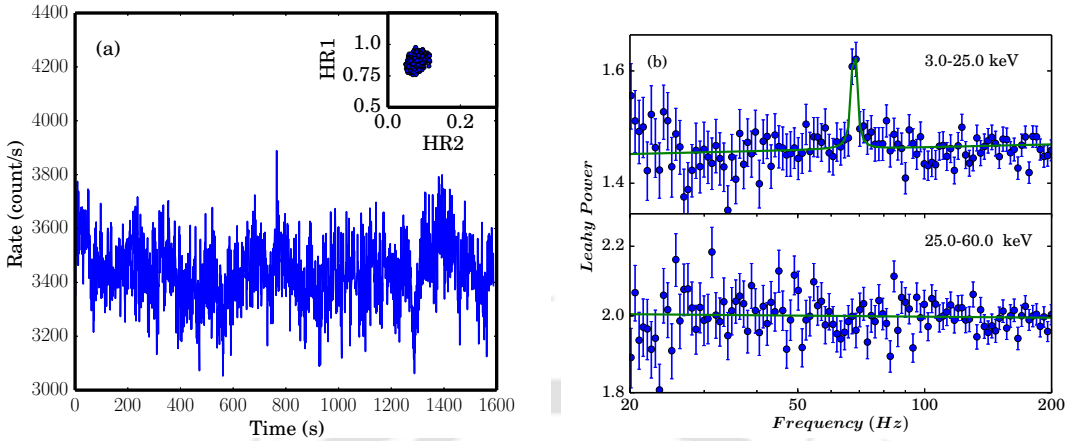

Figure 5.4: (a) Background subtracted lightcurve and (b) the corresponding power spectra obtained from LAXPC10 observation of the source GRS 1915+105 on MJD 57551.04. The color-color diagram is shown as inset in the top panel (a). The power spectra show a strong detection of HFQPO of frequency $\sim 68.09^{+0.46}_{-0.29}$ Hz in the energy band $3-25$ keV without any detection in higher energy band ($25-60$ keV). See text for details.

$6-15$ keV and $15-60$ keV energy bands, respectively. Comparing the CCD and X-ray variability with *RXTE* observation [286], we classify that the source was in its δ class during our observational campaign.

We search for the presence of QPOs in the power density spectrum upto a frequency of 1000 Hz. First, we create the lightcurves with a time resolution of 0.5 ms in the energy range of $3-25$ keV and $25-60$ keV. We use *powspec* task of XRONOSv5.22 to generate power spectra. We divide the lightcurves in intervals of 65536 newbins and the create the PDS for each interval and then average the PDS. The average PDS is normalized according to Leahy normalization. The final PDS is rebinned geometrically by a factor of 1.02 in the frequency space. The PDS in the $3-25$ keV energy band shows a narrow QPO like feature at ~ 67 Hz. Hence, we fit the PDS in the frequency range $20-200$ Hz with *constant* plus a *Lorentzian*. The PDS fitted with *Lorentzian* is shown in Figure 5.4(b). A strong QPO feature (Q-factor ~ 33.05, significance ~ 3.67 and rms $\sim 1.45\%$) at $\sim 68.09^{+0.46}_{-0.29}$ Hz has been detected in the power spectrum. The QPO feature is observed in the energy band of $3-25$ keV without any detection in the higher energy band of $25.0-60.0$ keV as shown in Figure 5.4(b). This detection is consistent with *RXTE* observation of variable HFQPOs ($63.5-71.3$ Hz), with an average of 67.3 ± 2.0 Hz [130, 287]. Besides this, Strohmayer (2001) [288] discovered a strong ~ 41 Hz QPO along with 69 Hz QPO in the same observation. A pair of HFQPOs (~ 164 Hz, ~ 328 Hz) has

also been reported [289] in harder state during 1997 observation, and later the finding was confirmed with frequency $\sim$ 170 Hz, but with marginal detection ($Q \sim 2$) [290].

We also extract source and background spectra in the energy range of $3 - 50$ keV [282, see for details]. For spectral fitting, we use the latest calibration files available provided by *AstroSat* mission team. We fit the energy spectrum with a model consisting of a thermal Comtonization component (*nthComp* in XSPEC; see [291]), a *Gaussian* feature and a *power-law* component. The hydrogen column density was fixed at 6×10^{22} $atoms/cm^2$ [283]. The model fitted energy spectrum along with residuals is shown in Figure 5.5. The model parameters of *nthComp* are electron temperature (kT_e), seed-photon temperature (kT_b) and power-law photon index (Γ). The spectral fitting with this model provides $kTe \sim 2.68$ keV, $kT_b \sim 1.32$ keV and $\Gamma \sim 2.06$. The additional *powerlaw* component required for the high energy emission (above $\sim$ 20 keV) has an photon-index of 3.34, which indicates the soft nature of the spectrum during our observation. This also further corroborates the class variability of δ, in which spectra are generally soft in nature. However, the energy spectrum does not show any signature of soft thermal component (i.e., disk blackbody emission) in the energy band of $3-10$ keV. The low electron temperature of $\sim$ 2.68 keV (i.e., high energy exponential roll over energy $\sim$ 10 keV) and $\Gamma \sim 2.06$ indicate that the 'Comptonized Corona' is very compact to produce high energy emission (via inverse-Comptonization of seed photons) beyond 20 keV. This has been clearly observed in the spectrum as shown in Figure 5.5.

5.3.3 Constraining Mass and Spin

In this work, we make an attempt to simulate the HEQPO features for black hole source GRS 1915+105 that have been observed by *LAXPC/AstroSat* as well as *RXTE* missions. While doing this, for Model E, we vary the mass of the source around its recent mass estimate [277]. The obtained results are depicted in Fig. 5.6 where the numerically computed frequency of HFQPOs ($\nu_{\rm QPO}$) is plotted as the function of black hole mass. The error bars shown in the figure corresponds to FWHM of the QPOs obtained from PDS modeling. Here, we observe that $\nu_{\rm QPO}$ decreases with the increase of $M_{\rm BH}$. This is not surprising because the frequency of the QPO is expected to scale inversely with the mass of the black hole ($\nu_{\rm QPO} \sim 1/M_{\rm BH}$) [105, 122, 248]. Considering the dynamically estimated mass of the

http://astrosat-ssc.iucaa.in/?q=laxpcData

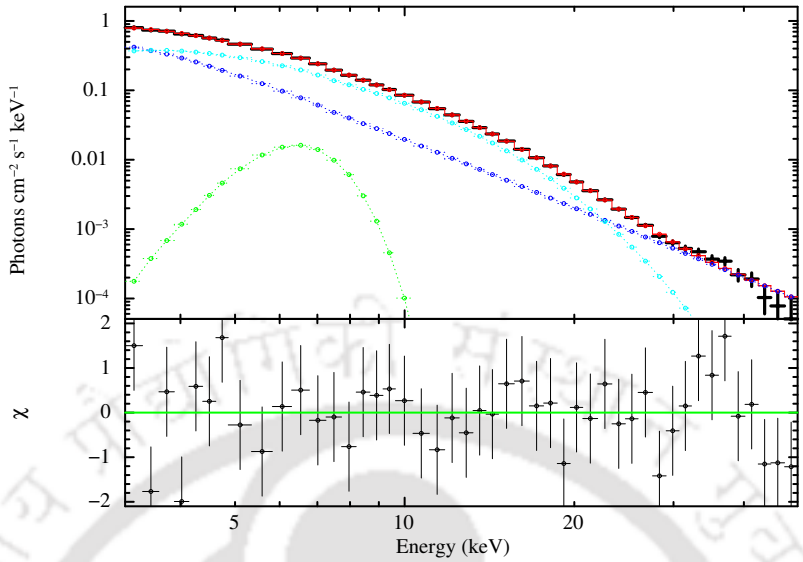

Figure 5.5: The best fit unfolded energy spectrum $(3-50$ keV) of GRS 1915+105 observed on MJD 57551.04 with *LAXPC/AstroSat*. The spectrum is modeled with *wabs(nthComp + Gaussian + powerlaw)*. The bottom panel shows residuals in units of σ.

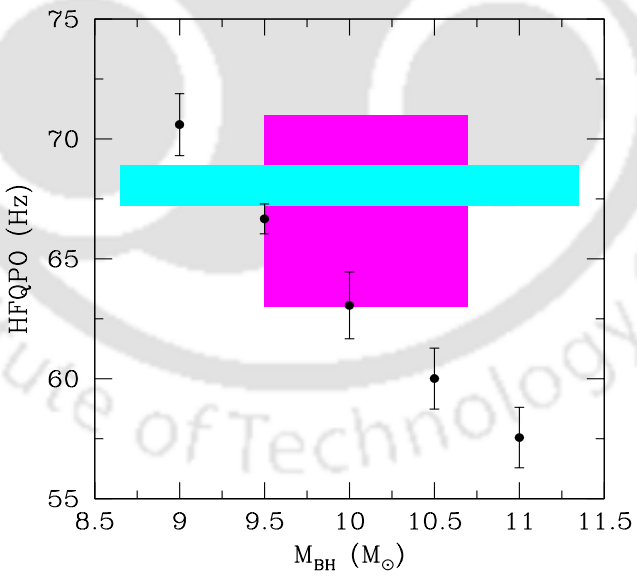

Figure 5.6: Possible range of mass and spin values of GRS 1915+105 based on observed HFQPOs and simulation results. Magenta shaded region represents the mass range $(10 \pm 0.6)M_\odot$) and HFQPO range $(64-71$ Hz) of the source estimated by means of observation. Cyan shaded region indicates the recent *LAXPC/Astrosat* observation where no mass limit is imposed. Simulation results of HFQPOs frequencies along with error bar for Model E are shown. See text for details.

source ($M_{\rm BH} = 10.1 \pm 0.6$) [277] and its observed HFQPO frequency ranges ($\nu_{\rm QPO} \sim 64 - 71$ Hz) [287], we identify the boundary of this region in $M_{\rm BH} - \nu_{\rm QPO}$ plane as depicted by the magenta shaded region in Fig. 5.6. Moreover, we also include the recently detected HFQPO as $68.09^{+0.46}_{-0.29}$ Hz in *LAXPC/AstroSat* data which is depicted using cyan shaded region where no mass limit is imposed. It is clear from the figure that a part of the simulation results are in agreement with the observational findings. Based on this, we argue that the mass of GRS 1915+105 seems to lie in the range of $9.5M_\odot \leq M_{\rm BH} \leq 10M_\odot$. Moreover, all the simulation results under consideration clearly demonstrate that HFQPO features are commonly observed for highly spinning black hole sources. In particular, the present analysis provides a hint that the black hole source GRS 1915+105 possibly spins extremely rapid with $a_k > 0.92$ to exhibit the HFQPO in the range $64 - 71$ Hz.

5.4 Chapter Conclusion

In this work, we investigate the dynamics of advective inviscid accretion flow using time-dependent hydrodynamical simulation around rotating black holes. During accretion, the accretion flow experiences a virtual barrier due to the repulsive centrifugal force against gravity and this virtual barrier triggers the shock transition. With the suitable choice of outer boundary parameters of the accreting matter, the shock starts to oscillate causing the oscillation of the inner part of the disc (PSC). This eventually exhibits the modulation of emergent radiation from PSC as well. When PSC modulates very rapidly, the signature of the HFQPOs is seen in the PDS. We find that several sets of flow parameters demonstrate the HFQPO features (see Table 5.1). We apply our simulation results of HFQPOs on to a Galactic black hole source GRS 1915+105. The source is known for producing HFQPOs ($65 - 67$) Hz [287]. Recently, India's multi-wavelength astronomical observatory *AstroSat* also observed this source . Using the observational data from *LAXPC* onboard of *AstroSat* and *RXTE*, we compare our simulation results and make an attempt to constrain the mass and spin values of this source. Based on the present formalism, we obtain the mass and spin ranges as $9.5M_\odot \leq M_{\rm BH} \leq 10M_\odot$ and $a_k > 0.92$, respectively.

Chapter 6

Conclusions

In this thesis, we self-consistently calculate the mass outflow rates from advective accretion disc around rotating black holes. Using our formalism, we explain some of the observational findings for several black hole sources.

In Chapter 2, we start with a steady, axisymmeteric, inviscid accretion flows around rotating black holes. To mimic the space-time geometry around rotating black holes, we adopt pseudo-Kerr potential proposed by Chakrabarti & Mondal (2006) [146]. The outflow geometry is constructed based on the numerical simulation work of Molteni et al. (1996) [154]. We find that the jet geometry is almost unaltered with the spin of the black hole except the region very close to the black hole horizon ($x \leq 10r_g$, $r_g = GM_{\rm BH}/c^2$). When outflow is emerged out from the inner part of the disc (PSC), post-shock pressure is decreased. As a consequence, the shock front moves towards the black hole horizon in order to maintain the pressure balance condition across the shock. We show that the shock-induced global inflow-outflow solutions exist for a wide range of inflow parameters, namely $\mathcal{E}$ and λ, respectively. We also estimate mass outflow rates ($R_{\dot{\rm m}}$) as a function of spin (a_k) for fixed inflow parameters ($\mathcal{E}, \lambda$). We observe that $R_{\dot{\rm m}}$ increases with a_k for fixed ($\mathcal{E}$, λ). This happens because of the fact that as a_k is increased, shock moves outward from black hole horizon and therefore, the amount of inflowing matter deflected by PSC becomes larger. Further, we calculate maximum outflow rates ($R_{\dot{\rm m}}^{\rm max}$) as a function a_k for different γ values. Interestingly, we observe that $R_{\dot{\rm m}}^{\rm max}$ is weakly correlated with the black hole spin a_k. Finally, we estimate the kinetic jet power based on our accretion-ejection model and find that the estimated kinetic jet power for various black hole sources (GBHs and AGNs) are in close agreement with the observed values [60, 292].

In Chapter 3, we consider a more generalized dissipative accretion flows around

rotating black holes. Here, flow suffers dissipation mainly due to viscosity and radiative cooling. We model the viscous dissipation following the mixed shear stress prescription of Chakrabarti (1996) [139] and the parametric cooling is adopted following the work of Narayan & Yi (1994) [20]. As before, we calculate the mass outflow rate and show that wide ranges of inflow parameters, namely $(\mathcal{E}_{\rm in}, \lambda_{\rm in}, \alpha)$ give rise to inflow-outflow solutions. We find that the shock front moves towards the black hole horizon with the increase of viscosity (α). This happens because the high value of α enhances the angular momentum transport outwards, reducing its value at the inner edge of the disc and this effectively weakens the centrifugal repulsion. We identify the effective region of parameter space in $\lambda_{\rm in} - \mathcal{E}_{\rm in}$ plane that admits shock in presence and absence of mass loss. We find that shock parameter space shrinks with the increase of α and ultimately disappears when the critical viscosity ($\alpha^{\rm max}$) is reached. Following that, we calculate maximum viscosity parameter that provides global shocked accretion solution with mass loss ($\alpha_{\rm o}^{\rm max}$) and without mass loss ($\alpha_{\rm no}^{\rm max}$) in terms of black hole spin (a_k). Finally, using our inflow-outflow formalism, we make an attempt to constrain the spin of the black hole source GRO J1655-40. Based on the present analysis, we find that $a_k \geq 0.57$ for this source.

In Chapter 4, we perform a comparative study of the global accretion-ejection solutions including shock wave by adopting three pseudo-Kerr potentials prescribed by Artemova et al. (1996) [144], Mukhopadhyay (2002) [145] and Chakrabarti & Mondal (2006) [146]. Here, we generalize the governing equations that describe the dissipative accretion flow around the rotating black hole and utilize these potentials accordingly. We find that standing shock continues to form in all the adopted pseudo-Kerr potentials for a wide range of flow parameters. We identify the shock parameter space in terms of energy ($\mathcal{E}_{\rm in}$) and angular momentum ($\lambda_{\rm in}$) of the flow for all the potentials. We also examine the role of adiabatic index (γ) in determining the shock solutions and notice that the shock parameter space is shrinked when γ is tending to the thermally non-relativistic limit. Further, we calculate the critical viscosity limit ($\alpha_{\rm shock}^{\rm cri}$) that allows standing shock solutions as a function of spin (a_k) for all the potentials. In case of weakly rotating black holes, we observe that $\alpha_{\rm shock}^{\rm cri}$ agrees quite well, but differs considerably for rapidly rotating black holes for all the potentials. We point out that standing shock solutions are not found beyond $a_k > 0.84$ for Mukhopadhyay (2002) [145] and $a_k > 0.92$ for Artemova et al. [144] potentials. We also compare the maximum outflow rates ($R_{\dot{\rm m}}^{\rm max}$) in terms of black hole spin (a_k) for all the potentials. A feeble correlation is observed between $R_{\dot{\rm m}}^{\rm max}$ and a_k irrespective of the choice of the potentials. Finally, we apply our accretion-

ejection model to explain 'outliers' track of the X-ray-radio correlations in black hole XRBs. All the sources are selected in their low-hard states from Corbel et al. (2013) [4]. We find that obtained results are in agreement with the observational findings of the XRBs lying along the 'outliers' track. Moreover, based on the present analysis, we point out that the 'outliers' sources seem to be rapidly rotating.

In chapter 5, we investigate the dynamics of advective, inviscid accretion flow using time-dependent hydrodynamical simulation around rotating black holes. We find that for the appropriate choice of the boundary parameters, accreting matter encounters shock transition which is oscillatory in nature. Since shock oscillates, the post-shock matter (PSC) also modulates causing the variation of emergent hard radiations from PSC as well. When the modulation of PSC becomes very rapid, it demonstrates the HFQPOs features. In this work, we carry out numerical study for five different models (Model A to E) that exhibits HFQPOs. Finally, we apply our simulation results to explain the HFQPOs signature ($\nu_{\rm QPO} \sim 65-67$ Hz) seen in GRS 1915+105 black hole source [287]. Recently, India's multi-wavelength astronomical observatory *AstroSat* also observe HFQPOs for this source. On comparing the results from simulation and observation, we find that the possible mass and spin values of GRS 1915+105 lie in the range $9.5M_{\odot} \leq M_{\rm BH} \leq 10M_{\odot}$ and $a_k > 0.92$, respectively.

Chapter 6 presents the conclusion the work of the thesis and discusses the scopes for future work.

6.1 Scopes of Future Work

Here we address some of the future prospects of this dissertation.

In this thesis, we study the dissipative accretion flow ignoring any realistic radiative cooling mechanisms, such as bremsstrahlung, synchrotron etc. However, in reality, all these cooling processes are expected to be active in the accretion flow and their roles become important in deciding the properties of accretion flow and associated mass outflows from the disc. Therefore, the investigation of accretion-ejection mechanism considering all the relevant cooling mechanisms around rotating black holes remains very much appealing.

We assume here that the coupling between electrons and ions are strong enough so that they are able to maintain a common single temperature profile all throughout the flow. However, as the inner part of the disc remains very hot and the radiative cooling time of relativistic electrons are shorter than the non-relativistic ions, the inflowing matter is expected to be characterized by the two-temperature profile at

least at the inner part of the disc. In a future work, we intend to examine the shock induced two-temperature accretion-ejection solutions around rotating black holes including all the relevant cooling mechanisms, namely, bremsstrahlung, synchrotron and Comptonization processes, respectively.

In this thesis, for the sake of simplicity, we adopt the pseudo potentials to mimic the space-time geometry around the rotating black holes. This approach provides satisfactory results for moderately rotating black holes as the non-linear effects in the vicinity of the black hole are not significant. However, in case of rapidly rotating black holes, a general relativistic treatment is unavoidable as the outflows are likely to be launched from the inner part of the disc and therefore, we plan to investigate accretion-ejection mechanism considering the general relativistic approach.

Further, we have not addressed the issue of transient relativistic ejections and its collimation mechanisms. Also, we consider constant adiabatic index instead of calculating it self-consistently based on its thermal properties. It would the important endeavors to investigate the underline role of all these effects on the accretion-ejection solutions around rotating black hole.

Bibliography

[1] C. L. Carilli and P. D. Barthel, The Astronomy and Astrophysics Review **7**, 1 (1996).

[2] R. Fender and T. Belloni, Science **337**, 540 (2012).

[3] B. Paczyńsky and P. J. Wiita, Astronomy and Astrophysics **88**, 23 (1980).

[4] Corbel et al., Monthly Notices of the Royal Astronomical Society: Letters **431**, L107 (2013).

[5] J. Frank, A. King, and D. J. Raine, *Accretion Power in Astrophysics: Third Edition*, 2002.

[6] M. S. Longair, *High Energy Astrophysics*, 2011.

[7] F. Hoyle and R. A. Lyttleton, Proceedings of the Cambridge Philosophical Society **35**, 405 (1939).

[8] H. Bondi and F. Hoyle, Monthly Notices of the Royal Astronomical Society **104**, 273 (1944).

[9] H. Bondi, Monthly Notices of the Royal Astronomical Society **112**, 195 (1952).

[10] N. I. Shakura and R. A. Sunyaev, Astronomy and Astrophysics **24**, 337 (1973).

[11] I. D. Novikov and K. S. Thorne, Astrophysics of black holes., in *Black Holes (Les Astres Occlus)*, edited by C. Dewitt and B. S. Dewitt, pages 343–450, 1973.

[12] S. L. Shapiro, A. P. Lightman, and D. M. Eardley, The Astrophysical Journal **204**, 187 (1976).

[13] T. Piran, The Astrophysical Journal **221**, 652 (1978).

[14] M. A. Abramowicz, B. Czerny, J. P. Lasota, and E. Szuszkiewicz, The Astrophysical Journal **332**, 646 (1988).

[15] M. Jaroszynski, M. A. Abramowicz, and B. Paczynski, Acta Astronomica **30**, 1 (1980).

[16] A. M. Beloborodov, Monthly Notices of the Royal Astronomical Society **297**, 739 (1998).

[17] A. Sądowski, The Astrophysical Journal Supplement **183**, 171 (2009).

[18] S. Ichimaru, The Astrophysical Journal **214**, 840 (1977).

[19] R. Narayan and R. Popham, Nature **362**, 820 (1993).

[20] R. Narayan and I. Yi, The Astrophysical Journal **428**, L13 (1994).

[21] R. Narayan and I. Yi, The Astrophysical Journal **444**, 231 (1995).

[22] R. Narayan and I. Yi, The Astrophysical Journal **452**, 710 (1995).

[23] M. A. Abramowicz, X. Chen, S. Kato, J.-P. Lasota, and O. Regev, The Astrophysical Journal **438**, L37 (1995).
[24] X. Chen, Monthly Notices of the Royal Astronomical Society **275**, 641 (1995).
[25] X. Chen, M. A. Abramowicz, J.-P. Lasota, R. Narayan, and I. Yi, The Astrophysical Journal **443**, L61 (1995).
[26] M. A. Abramowicz, X.-M. Chen, M. Granath, and J.-P. Lasota, The Astrophysical Journal **471**, 762 (1996).
[27] X. Chen, M. A. Abramowicz, and J.-P. Lasota, The Astrophysical Journal **476**, 61 (1997).
[28] R. D. Blandford and M. C. Begelman, Monthly Notices of the Royal Astronomical Society **303**, L1 (1999).
[29] R. D. Blandford and M. C. Begelman, Monthly Notices of the Royal Astronomical Society **349**, 68 (2004).
[30] M. C. Begelman, Monthly Notices of the Royal Astronomical Society **420**, 2912 (2012).
[31] R. Narayan, I. V. Igumenshchev, and M. A. Abramowicz, The Astrophysical Journal **539**, 798 (2000).
[32] E. Quataert and A. Gruzinov, The Astrophysical Journal **539**, 809 (2000).
[33] M. A. Abramowicz, I. V. Igumenshchev, E. Quataert, and R. Narayan, The Astrophysical Journal **565**, 1101 (2002).
[34] I. V. Igumenshchev, The Astrophysical Journal **577**, L31 (2002).
[35] S. Chakrabarti and L. G. Titarchuk, Astrophysical Journal **455**, 623 (1995).
[36] S. K. Chakrabarti, *Theory of Transonic Astrophysical Flows*, World Scientific Publishing Co, 1990.
[37] J. Fukue, Astronomical Society of Japan **39**, 309 (1987).
[38] S. K. Chakrabarti, The Astrophysical Journal **347**, 365 (1989).
[39] P. A. Becker and D. Kazanas, The Astrophysical Journal **546**, 429 (2001).
[40] L. D. Landau and E. M. Lifshitz, *Fluid mechanics*, 1959.
[41] S. K. Chakrabarti, Astronomy and Astrophysics **351**, 185 (1999).
[42] S. Das, I. Chattopadhyay, and S. K. Chakrabarti, The Astrophysical Journal **557**, 983 (2001).
[43] I. Chattopadhyay and S. Das, New Astronomy **12**, 454 (2007).
[44] S. Das and I. Chattopadhyay, New Astronomy **13**, 549 (2008).
[45] R. Kumar and I. Chattopadhyay, Monthly Notices of the Royal Astronomical Society **430**, 386 (2013).
[46] S. K. Chakrabarti and S. Mandal, The Astrophysical Journal **642**, L49 (2006).
[47] S. Mondal, D. Debnath, and S. K. Chakrabarti, The Astrophysical Journal **786**, 4 (2014).
[48] D. Debnath, S. Mondal, and S. K. Chakrabarti, Monthly Notices of the Royal Astronomical Society **447**, 1984 (2015).
[49] A. Nandi, D. Debnath, S. Mandal, and S. K. Chakrabarti, Astronomy and Astro-

physics **542**, A56 (2012).
[50] D. Radhika and A. Nandi, Advances in Space Research **54**, 1678 (2014).
[51] N. Iyer, A. Nandi, and S. Mandal, The Astrophysical Journal **807**, 108 (2015).
[52] I. F. Mirabel, L. F. Rodriguez, B. Cordier, J. Paul, and F. Lebrun, Nature **358**, 215 (1992).
[53] I. F. Mirabel and L. F. Rodríguez, Nature **371**, 46 (1994).
[54] R. M. Hjellming and M. P. Rupen, Nature **375**, 464 (1995).
[55] A. Ferrari, Annual Review of Astronomy and Astrophysics **36**, 539 (1998).
[56] W. Junor, J. A. Biretta, and M. Livio, Nature **401**, 891 (1999).
[57] C. C. Cheung, The Astrophysical Journal Letters **581**, L15 (2002).
[58] I. Mirabel, New Astronomy Reviews **47**, 471 (2003).
[59] R. P. Fender, J. Homan, and T. M. Belloni, Monthly Notices of the Royal Astronomical Society **396**, 1370 (2009).
[60] J. M. Miller et al., The Astrophysical Journal Letters **759**, L6 (2012).
[61] M. Mezcua, T. P. Roberts, A. D. Sutton, and A. P. Lobanov, Monthly Notices of the Royal Astronomical Society **436**, 3128 (2013).
[62] M. Mezcua, T. P. Roberts, A. P. Lobanov, and A. D. Sutton, Monthly Notices of the Royal Astronomical Society **448**, 1893 (2015).
[63] R. Fender and T. Muñoz-Darias, The balance of power: Accretion and feedback in stellar mass black holes, in *Lecture Notes in Physics, Berlin Springer Verlag*, volume 905 of *Lecture Notes in Physics, Berlin Springer Verlag*, page 65, 2016.
[64] M. L. Lister et al., The Astronomical Journal **138**, 1874 (2009).
[65] R. P. Fender, T. M. Belloni, and E. Gallo, Monthly Notices of the Royal Astronomical Society **355**, 1105 (2004).
[66] R. Fender and E. Gallo, Space Science Reviews **183**, 323 (2014).
[67] P. Casella, T. Belloni, and L. Stella, The Astrophysical Journal **629**, 403 (2005).
[68] R. Fender et al., The Astrophysical Journal Letters **519**, L165 (1999).
[69] Miller-Jones et al., Monthly Notices of the Royal Astronomical Society **421**, 468 (2012).
[70] D. M. Russell, J. C. A. Miller-Jones, T. J. Maccarone, Y. J. Yang, R. P. Fender, and F. Lewis, The Astrophysical Journal Letters **739**, L19 (2011).
[71] R. Penrose, Nuovo Cimento Rivista Serie **1** (1969).
[72] R. D. Blandford and R. L. Znajek, Monthly Notices of the Royal Astronomical Society **179**, 433 (1977).
[73] A. Tchekhovskoy, R. Narayan, and J. C. McKinney, The Astrophysical Journal **711**, 50 (2010).
[74] T. Kudoh, R. Matsumoto, and K. Shibata, The Astrophysical Journal **508**, 186 (1998).
[75] S. Koide, K. Shibata, and T. Kudoh, The Astrophysical Journal **522**, 727 (1999).
[76] T. Kuwabara, K. Shibata, T. Kudoh, and R. Matsumoto, Publications of the Astronomical Society of Japan **52**, 1109 (2000).
[77] J. F. Hawley and S. A. Balbus, The Astrophysical Journal **573**, 738 (2002).

[78] J. C. McKinney and C. F. Gammie, The Astrophysical Journal **611**, 977 (2004).
[79] J. C. McKinney, The Astrophysical Journal **630**, L5 (2005).
[80] J.-P. De Villiers, J. F. Hawley, J. H. Krolik, and S. Hirose, The Astrophysical Journal **620**, 878 (2005).
[81] S. S. Komissarov, Monthly Notices of the Royal Astronomical Society **382**, 995 (2007).
[82] A. Tchekhovskoy, R. Narayan, and J. C. McKinney, Monthly Notices of the Royal Astronomical Society **418**, L79 (2011).
[83] A. Sądowski, R. Narayan, R. Penna, and Y. Zhu, Monthly Notices of the Royal Astronomical Society **436**, 3856 (2013).
[84] F. Yuan and R. Narayan, Annual Review of Astronomy and Astrophysics **52**, 529 (2014).
[85] E. G. Körding, R. P. Fender, and S. Migliari, Monthly Notices of the Royal Astronomical Society **369**, 1451 (2006).
[86] A. Merloni and S. Heinz, *Evolution of Active Galactic Nuclei*, pages 503–566, Springer Netherlands, Dordrecht, 2013.
[87] Jonker et al., Monthly Notices of the Royal Astronomical Society **401**, 1255 (2010).
[88] Coriat et al., Monthly Notices of the Royal Astronomical Society **414**, 677 (2011).
[89] Cadolle Bel et al., The Astrophysical Journal **659**, 549 (2007).
[90] Soleri et al., Monthly Notices of the Royal Astronomical Society **406**, 1471 (2010).
[91] S. Corbel, R. P. Fender, J. A. Tomsick, A. K. Tzioumis, and S. Tingay, The Astrophysical Journal **617**, 1272 (2004).
[92] Ratti et al., Monthly Notices of the Royal Astronomical Society **423**, 2656 (2012).
[93] M. S. Longair, *High energy astrophysics. Volume 2. Stars, the Galaxy and the interstellar medium.*, 1994.
[94] R. P. Fender, Monthly Notices of the Royal Astronomical Society **322**, 31 (2001).
[95] J. F. Steiner, J. E. McClintock, R. A. Remillard, R. Narayan, and L. Gou, The Astrophysical Journal Letters **701**, L83 (2009).
[96] J. F. Steiner, J. E. McClintock, R. A. Remillard, L. Gou, S. Yamada, and R. Narayan, The Astrophysical Journal Letters **718**, L117 (2010).
[97] J. F. Steiner et al., Monthly Notices of the Royal Astronomical Society **416**, 941 (2011).
[98] A. K. Kulkarni et al., Monthly Notices of the Royal Astronomical Society **414**, 1183 (2011).
[99] L. Gou et al., The Astrophysical Journal **790**, 29 (2014).
[100] R. Narayan and J. E. McClintock, Monthly Notices of the Royal Astronomical Society: Letters **419**, L69 (2012).
[101] J. F. Steiner, J. E. McClintock, and R. Narayan, The Astrophysical Journal **762**, 104 (2013).
[102] J. E. McClintock, R. Narayan, and J. F. Steiner, Space Science Reviews **183**, 295 (2014).

[103] D. M. Russell, E. Gallo, and R. P. Fender, Monthly Notices of the Royal Astronomical Society **431**, 405 (2013).
[104] S. E. Motta, P. Casella, M. Henze, T. Muñoz-Darias, A. Sanna, R. Fender, and T. Belloni, Monthly Notices of the Royal Astronomical Society **447**, 2059 (2015).
[105] R. A. Remillard and J. E. McClintock, Annual Review of Astronomy and Astrophysics **44**, 49 (2006).
[106] M. van der Klis, Annual review of astronomy and astrophysics **27**, 517 (1989).
[107] J. Homan, M. van der Klis, P. G. Jonker, R. Wijnands, E. Kuulkers, M. Méndez, and W. H. G. Lewin, The Astrophysical Journal **568**, 878 (2002).
[108] T. Belloni, J. Homan, S. Motta, E. Ratti, and M. Méndez, Monthly Notices of the Royal Astronomical Society **379**, 247 (2007).
[109] J. Patterson, E. L. Robinson, and R. E. Nather, The Astrophysical Journal **214**, 144 (1977).
[110] B. Warner, The Publications of the Astronomical Society of the Pacific **116**, 115 (2004).
[111] T. E. Strohmayer and R. F. Mushotzky, The Astrophysical Journal Letters **586**, L61 (2003).
[112] Bachetti et al., Nature **514**, 202 (2014).
[113] M. Gierliński, M. Middleton, M. Ward, and C. Done, Nature **455**, 369 (2008).
[114] M. Middleton and C. Done, Monthly Notices of the Royal Astronomical Society **403**, 9 (2010).
[115] T. M. Belloni and S. E. Motta, *Transient Black Hole Binaries*, pages 61–97, Springer Berlin Heidelberg, Berlin, Heidelberg, 2016.
[116] L. Stella and M. Vietri, The Astrophysical Journal Letters **492**, L59 (1998).
[117] L. Stella, M. Vietri, and S. M. Morsink, The Astrophysical Journal Letters **524**, L63 (1999).
[118] S. E. Motta, T. M. Belloni, L. Stella, T. Muñoz-Darias, and R. Fender, Monthly Notices of the Royal Astronomical Society **437**, 2554 (2014).
[119] M. Tagger and R. Pellat, Astronomy and Astrophysics **349**, 1003 (1999).
[120] Varnire, P. and Tagger, M., Astronomy and Astrophysics **394**, 329 (2002).
[121] Rodriguez, J., Varnire, P., Tagger, M., and Durouchoux, Ph., Astronomy and Astrophysics **387**, 487 (2002).
[122] D. Molteni, H. Sponholz, and S. K. Chakrabarti, Astrophysical Journal **457**, 805 (1996).
[123] K. Giri, S. K. Chakrabarti, M. M. Samanta, and D. Ryu, Monthly Notices of the Royal Astronomical Society **403**, 516 (2010).
[124] S. K. Garain, H. Ghosh, and S. K. Chakrabarti, Monthly Notices of the Royal Astronomical Society **437**, 1329 (2014).
[125] S. Das, I. Chattopadhyay, A. Nandi, and D. Molteni, Monthly Notices of the Royal Astronomical Society **442**, 251 (2014).
[126] M. A. Nowak and R. V. Wagoner, Astrophysical Journal **418**, 187 (1993).

[127] L. Titarchuk and V. Osherovich, The Astrophysical Journal Letters **542**, L111 (2000).
[128] X.-M. Hua, D. Kazanas, and L. Titarchuk, The Astrophysical Journal Letters **482**, L57 (1997).
[129] M. Böttcher and E. P. Liang, The Astrophysical Journal **506**, 281 (1998).
[130] E. H. Morgan, R. A. Remillard, and J. Greiner, The Astrophysical Journal **482**, 993 (1997).
[131] T. M. Belloni, A. Sanna, and M. Mndez, Monthly Notices of the Royal Astronomical Society **426**, 1701 (2012).
[132] T. M. Belloni and L. Stella, Space Science Reviews **183**, 43 (2014).
[133] A. Merloni, M. Vietri, L. Stella, and D. Bini, Monthly Notices of the Royal Astronomical Society **304**, 155 (1999).
[134] Abramowicz, M. A. and Kluniak, W., Astronomy and Astrophysics **374**, L19 (2001).
[135] W. Kluzniak and M. A. Abramowicz, Acta Physica Polonica B **32**, 3605 (2001).
[136] M. A. Abramowicz, W. Kluniak, J. E. McClintock, and R. A. Remillard, The Astrophysical Journal Letters **609**, L63 (2004).
[137] K. Schwarzschild, Abh. Konigl. Preuss. Akad. Wissenschaften Jahre 1906,92, Berlin,1907 **1916** (1916).
[138] S. L. Shapiro and S. A. Teukolsky, *Black holes, white dwarfs, and neutron stars: The physics of compact objects*, 1983.
[139] S. K. Chakrabarti, Physics Reports **266**, 229 (1996).
[140] R. P. Kerr, Phys. Rev. Lett. **11**, 237 (1963).
[141] R. H. Boyer and R. W. Lindquist, Journal of Mathematical Physics **8**, 265 (1967).
[142] J. M. Bardeen, W. H. Press, and S. A. Teukolsky, The Astrophysical Journal **178**, 347 (1972).
[143] S. K. Chakrabarti and R. Khanna, Monthly Notices of the Royal Astronomical Society **256**, 300 (1992).
[144] I. V. Artemova, G. Bjoernsson, and I. D. Novikov, The Astrophysical Journal **461**, 565 (1996).
[145] B. Mukhopadhyay, The Astrophysical Journal **581**, 427 (2002).
[146] S. K. Chakrabarti and S. Mondal, Monthly Notices of the Royal Astronomical Society **369**, 976 (2006).
[147] O. Semerák and V. Karas, Astronomy and Astrophysics **343**, 325 (1999).
[148] R. I. Ivanov and E. M. Prodanov, Physics Letters B **611**, 34 (2005).
[149] S. Ghosh and B. Mukhopadhyay, The Astrophysical Journal **667**, 367 (2007).
[150] S. Ghosh, T. Sarkar, and A. Bhadra, Monthly Notices of the Royal Astronomical Society **445**, 4463 (2014).
[151] R. Fernández, D. Kasen, B. D. Metzger, and E. Quataert, Monthly Notices of the Royal Astronomical Society **446**, 750 (2015).
[152] S. Mondal and S. K. Chakrabarti, Monthly Notices of the Royal Astronomical Society **371**, 1418 (2006).

[153] C. Clarke and B. Carswell, *Principles of Astrophysical Fluid Dynamics*, 2007.
[154] D. Molteni, D. Ryu, and S. K. Chakrabarti, The Astrophysical Journal **470**, 460 (1996).
[155] W. Kley, Astronomy and Astrophysics **208**, 98 (1989).
[156] T. Okuda, M. Fujita, and S. Sakashita, Publications of the Astronomical Society of Japan **49**, 679 (1997).
[157] T. Okuda, V. Teresi, E. Toscano, and D. Molteni, Publications of the Astronomical Society of Japan **56**, 547 (2004).
[158] T. Okuda, V. Teresi, and D. Molteni, Monthly Notices of the Royal Astronomical Society **377**, 1431 (2007).
[159] I. F. Mirabel and L. F. Rodríguez, Nature **392**, 673 (1998).
[160] A.-C. Donea and P. L. Biermann, Astronomy and Astrophysics **316**, 43 (1996).
[161] J.-F. Lu, W.-M. Gu, and F. Yuan, The Astrophysical Journal **523**, 340 (1999).
[162] K. Fukumura and S. Tsuruta, The Astrophysical Journal **611**, 964 (2004).
[163] D. Molteni, G. Lanzafame, and S. K. Chakrabarti, The Astrophysical Journal **425**, 161 (1994).
[164] M. Machida, M. R. Hayashi, and R. Matsumoto, The Astrophysical Journal **532**, L67 (2000).
[165] T. Okuda, Monthly Notices of the Royal Astronomical Society **441**, 2354 (2014).
[166] T. Okuda and S. Das, Monthly Notices of the Royal Astronomical Society **453**, 147 (2015).
[167] S. Das, I. Chattopadhyay, A. Nandi, and S. K. Chakrabarti, Astronomy and Astrophysics **379**, 683 (2001).
[168] C. B. Singh and S. K. Chakrabarti, Monthly Notices of the Royal Astronomical Society **410**, 2414 (2011).
[169] R. Kumar, C. B. Singh, I. Chattopadhyay, and S. K. Chakrabarti, Monthly Notices of the Royal Astronomical Society **436**, 2864 (2013).
[170] S. Das, Monthly Notices of the Royal Astronomical Society **376**, 1659 (2007).
[171] S. K. Chakrabarti, D. Debnath, A. Nandi, and P. S. Pal, Astronomy and Astrophysics **489**, L41 (2008).
[172] S. K. Chakrabarti, B. G. Dutta, and P. S. Pal, Monthly Notices of the Royal Astronomical Society **394**, 1463 (2009).
[173] D. Debnath, S. K. Chakrabarti, and A. Nandi, Advances in Space Research **52**, 2143 (2013).
[174] S. Corbel, R. P. Fender, A. K. Tzioumis, M. Nowak, V. McIntyre, P. Durouchoux, and R. Sood, Astronomy and Astrophysics **359**, 251 (2000).
[175] S. Corbel et al., The Astrophysical Journal **554**, 43 (2001).
[176] R. P. Fender, R. M. Hjellming, R. P. J. Tilanus, G. G. Pooley, J. R. Deane, R. N. Ogley, and R. E. Spencer, Monthly Notices of the Royal Astronomical Society **322**, L23 (2001).
[177] S. Migliari et al., The Astrophysical Journal **670**, 610 (2007).

[178] A. G. Cantrell et al., The Astrophysical Journal **710**, 1127 (2010).
[179] L. Gou, J. E. McClintock, J. F. Steiner, R. Narayan, A. G. Cantrell, C. D. Bailyn, and J. A. Orosz, The Astrophysical Journal Letters **718**, L122 (2010).
[180] J. A. Orosz et al., The Astrophysical Journal **794**, 154 (2014).
[181] A. Kubota, C. Done, S. W. Davis, T. Dotani, T. Mizuno, and Y. Ueda, The Astrophysical Journal **714**, 860 (2010).
[182] J. F. Steiner, J. E. McClintock, J. A. Orosz, R. A. Remillard, C. D. Bailyn, M. Kolehmainen, and O. Straub, The Astrophysical Journal Letters **793**, L29 (2014).
[183] J. A. Orosz, J. F. Steiner, J. E. McClintock, M. A. P. Torres, R. A. Remillard, C. D. Bailyn, and J. M. Miller, The Astrophysical Journal **730**, 75 (2011).
[184] J. A. Orosz et al., Nature **449**, 872 (2007).
[185] J. Liu, J. E. McClintock, R. Narayan, S. W. Davis, and J. A. Orosz, The Astrophysical Journal Letters **679**, L37 (2008).
[186] J. Liu, J. E. McClintock, R. Narayan, S. W. Davis, and J. A. Orosz, The Astrophysical Journal Letters **719**, L109 (2010).
[187] J. A. Orosz, Inventory of black hole binaries, in *A Massive Star Odyssey: From Main Sequence to Supernova*, edited by K. van der Hucht, A. Herrero, and C. Esteban, volume 212 of *IAU Symposium*, page 365, 2003.
[188] W. R. Morningstar and J. M. Miller, The Astrophysical Journal Letters **793**, L33 (2014).
[189] J. A. Orosz et al., The Astrophysical Journal **697**, 573 (2009).
[190] L. Gou et al., The Astrophysical Journal **701**, 1076 (2009).
[191] J. A. Orosz, J. E. McClintock, J. P. Aufdenberg, R. A. Remillard, M. J. Reid, R. Narayan, and L. Gou, The Astrophysical Journal **742**, 84 (2011).
[192] L. Gou et al., The Astrophysical Journal **742**, 85 (2011).
[193] B. M. Peterson et al., The Astrophysical Journal **613**, 682 (2004).
[194] R. A. Riffel, T. Storchi-Bergmann, and C. Winge, Monthly Notices of the Royal Astronomical Society **430**, 2249 (2013).
[195] L. C. Gallo, G. Miniutti, J. M. Miller, L. W. Brenneman, A. C. Fabian, M. Guainazzi, and C. S. Reynolds, Monthly Notices of the Royal Astronomical Society **411**, 607 (2011).
[196] J. L. Walsh, A. J. Barth, L. C. Ho, and M. Sarzi, The Astrophysical Journal **770**, 86 (2013).
[197] C. Y. Kuo et al., The Astrophysical Journal Letters **783**, L33 (2014).
[198] J.-M. Wang, Y.-R. Li, J.-C. Wang, and S. Zhang, The Astrophysical Journal Letters **676**, L109 (2008).
[199] B. Aschenbach, Memorie della Societ Astronomica Italiana **81**, 319 (2010).
[200] F. Yuan, S. Markoff, and H. Falcke, Astronomy and Astrophysics **383**, 854 (2002).
[201] de Gasperin et al., Astronomy and Astrophysics **547**, A56 (2012).
[202] H. Falcke and P. L. Biermann, Astronomy and Astrophysics **342**, 49 (1999).
[203] J. Homan and T. Belloni, Astrophysics and Space Science **300**, 107 (2005).

[204] D. Debnath, S. K. Chakrabarti, A. Nandi, and S. Mandal, Bulletin of the Astronomical Society of India **36**, 151 (2008).
[205] C. Brocksopp et al., Monthly Notices of the Royal Astronomical Society **331**, 765 (2002).
[206] M. Cadolle Bel et al., Astronomy and Astrophysics **534**, A119 (2011).
[207] A. V. Filippenko and R. Chornock, IAU Circ **7644** (2001).
[208] N. Shaposhnikov and L. Titarchuk, The Astrophysical Journal **699**, 453 (2009).
[209] J. M. Corral-Santana, J. Casares, T. Shahbaz, C. Zurita, I. G. Martínez-Pais, and P. Rodríguez-Gil, Monthly Notices of the Royal Astronomical Society **413**, L15 (2011).
[210] S. E. Motta, T. Muñoz-Darias, A. Sanna, R. Fender, T. Belloni, and L. Stella, Monthly Notices of the Royal Astronomical Society **439**, L65 (2014).
[211] J. Greene, C. D. Bailyn, and J. A. Orosz, The Astrophysical Journal **554**, 1290 (2001).
[212] R. Shafee, J. E. McClintock, R. Narayan, S. W. Davis, L.-X. Li, and R. A. Remillard, The Astrophysical Journal **636**, L113 (2006).
[213] R. C. Reis, A. C. Fabian, R. R. Ross, and J. M. Miller, Monthly Notices of the Royal Astronomical Society **395**, 1257 (2009).
[214] T. Chen, The determination of the GX 339-4's mass based on its 2010 outburst, in *Jets at All Scales*, edited by G. E. Romero, R. A. Sunyaev, and T. Belloni, volume 275 of *IAU Symposium*, pages 327–328, 2011.
[215] R. I. Hynes, D. Steeghs, J. Casares, P. A. Charles, and K. O'Brien, The Astrophysical Journal **609**, 317 (2004).
[216] R. C. Reis, A. C. Fabian, R. R. Ross, G. Miniutti, J. M. Miller, and C. Reynolds, Monthly Notices of the Royal Astronomical Society **387**, 1489 (2008).
[217] J. M. Miller et al., The Astrophysical Journal Letters **679**, L113 (2008).
[218] M. Kolehmainen and C. Done, Monthly Notices of the Royal Astronomical Society **406**, 2206 (2010).
[219] S. Yamada et al., The Astrophysical Journal Letters **707**, L109 (2009).
[220] J. F. Steiner, J. E. McClintock, and M. J. Reid, The Astrophysical Journal Letters **745**, L7 (2012).
[221] J. Greiner, J. G. Cuby, and M. J. McCaughrean, Nature **414**, 522 (2001).
[222] D. J. Hurley, P. J. Callanan, P. Elebert, and M. T. Reynolds, Monthly Notices of the Royal Astronomical Society **430**, 1832 (2013).
[223] M. J. Reid, J. E. McClintock, J. F. Steiner, D. Steeghs, R. A. Remillard, V. Dhawan, and R. Narayan, The Astrophysical Journal **796**, 2 (2014).
[224] J. E. McClintock, R. Shafee, R. Narayan, R. A. Remillard, S. W. Davis, and L.-X. Li, The Astrophysical Journal **652**, 518 (2006).
[225] J. L. Blum et al., The Astrophysical Journal **706**, 60 (2009).
[226] T. Belloni, M. Méndez, and C. Sánchez-Fernández, Astronomy and Astrophysics **372**, 551 (2001).

[227] A. Nandi, S. G. Manickam, and S. K. Chakrabarti, ArXiv Astrophysics e-prints (2000).
[228] R. Aktar, S. Das, and A. Nandi, Monthly Notices of the Royal Astronomical Society **453**, 3414 (2015).
[229] S. Das, S. K. Chakrabarti, and S. Mondal, Monthly Notices of the Royal Astronomical Society **401**, 2053 (2010).
[230] S. K. Chakrabarti, Astrophysical Journal **464**, 664 (1996).
[231] R. Matsumoto, S. Kato, J. Fukue, and A. T. Okazaki, Astronomical Society of Japan **36**, 71 (1984).
[232] S. K. Chakrabarti and S. Das, Monthly Notices of the Royal Astronomical Society **349**, 649 (2004).
[233] S.-J. Lee, D. Ryu, and I. Chattopadhyay, The Astrophysical Journal **728**, 142 (2011).
[234] S. Das and R. Aktar, Dynamically induced shock oscillation in the accretion disc around black holes, in *Astronomical Society of India Conference Series*, volume 12 of *Astronomical Society of India Conference Series*, 2015.
[235] P. Suková and A. Janiuk, Monthly Notices of the Royal Astronomical Society **447**, 1565 (2015).
[236] S. K. Chakrabarti, A. Nandi, S. G. Manickam, S. Mandal, and A. R. Rao, The Astrophysical Journal **579**, L21 (2002).
[237] D. Radhika, A. Nandi, V. K. Agrawal, and S. Seetha, Monthly Notices of the Royal Astronomical Society **460**, 4403 (2016).
[238] Tingay et al., Nature **374**, 141 (1995).
[239] S. N. Zhang et al., The Astrophysical Journal **479**, 381 (1997).
[240] J. I. González Hernández, R. Rebolo, and G. Israelian, Astronomy and Astrophysics **478**, 203 (2008).
[241] R. A. Remillard, M. P. Muno, J. E. McClintock, and J. A. Orosz, The Astrophysical Journal **580**, 1030 (2002).
[242] M. E. Beer and P. Podsiadlowski, Monthly Notices of the Royal Astronomical Society **331**, 351 (2002).
[243] J. M. Miller, C. S. Reynolds, A. C. Fabian, G. Miniutti, and L. C. Gallo, The Astrophysical Journal **697**, 900 (2009).
[244] Z. Stuchlík and M. Kološ, The Astrophysical Journal **825**, 13 (2016).
[245] R. A. Remillard, E. H. Morgan, J. E. McClintock, C. D. Bailyn, and J. A. Orosz, The Astrophysical Journal **522**, 397 (1999).
[246] T. E. Strohmayer, The Astrophysical Journal **552**, L49 (2001).
[247] D. A. Leahy, W. Darbro, R. F. Elsner, M. C. Weisskopf, P. G. Sutherland, S. Kahn, and J. E. Grindlay, Astrophysical Journal **266**, 160 (1983).
[248] R. Aktar, S. Das, A. Nandi, and H. Sreehari, Monthly Notices of the Royal Astronomical Society **471**, 4806 (2017).
[249] R. Kumar and I. Chattopadhyay, Monthly Notices of the Royal Astronomical Society

443, 3444 (2014).
[250] D. Ryu, S. K. Chakrabarti, and D. Molteni, The Astrophysical Journal **474**, 378 (1997).
[251] S. K. Chakrabarti and S. G. Manickam, The Astrophysical Journal **531**, L41 (2000).
[252] D. Proga and M. C. Begelman, The Astrophysical Journal **582**, 69 (2003).
[253] F. Yuan, M. Wu, and D. Bu, The Astrophysical Journal **761**, 129 (2012).
[254] F. Yuan, D. Bu, and M. Wu, The Astrophysical Journal **761**, 130 (2012).
[255] S.-J. Lee, I. Chattopadhyay, R. Kumar, S. Hyung, and D. Ryu, The Astrophysical Journal **831**, 33 (2016).
[256] R. Aktar, S. Das, A. Nandi, and H. Sreehari, Journal of Astrophysics and Astronomy **39**, 17 (2018).
[257] S. Das and S. K. Chakrabarti, Monthly Notices of the Royal Astronomical Society **389**, 371 (2008).
[258] B. Sarkar and S. Das, Monthly Notices of the Royal Astronomical Society **461**, 190 (2016).
[259] A. Nandi et al., Astrophysics and Space Science **363**, 90 (2018).
[260] R. Fender, T. Belloni, and E. Gallo, Astrophysics and Space Science **300**, 1 (2005).
[261] D. C. Hannikainen, R. W. Hunstead, D. Campbell-Wilson, and R. K. Sood, Astronomy and Astrophysics **337**, 460 (1998).
[262] Corbel, S., Nowak, M. A., Fender, R. P., Tzioumis, A. K., and Markoff, S., Astronomy and Astrophysics **400**, 1007 (2003).
[263] E. Gallo, R. P. Fender, and G. G. Pooley, Monthly Notice of the Royal Astronomical Society **344**, 60 (2003).
[264] C.-Y. Huang, Q. Wu, and D.-X. Wang, Monthly Notices of the Royal Astronomical Society **440**, 965 (2014).
[265] R. D. Blandford and A. Königl, The Astrophysical Journal **232**, 34 (1979).
[266] H. Falcke and P. L. Biermann, Astronomy and Astrophysics **308**, 321 (1996).
[267] S. Heinz and R. A. Sunyaev, Monthly Notices of the Royal Astronomical Society **343**, L59 (2003).
[268] S. Heinz and H. J. Grimm, The Astrophysical Journal **633**, 384 (2005).
[269] B. Warner, Publications of the Astronomical Society of the Pacific **116**, 115 (2004).
[270] G. C. Dewangan, L. Titarchuk, and R. E. Griffiths, The Astrophysical Journal **637**, L21 (2006).
[271] V. K. Agrawal and A. Nandi, Monthly Notices of the Royal Astronomical Society **446**, 3926 (2015).
[272] P. Rebusco, Nature **51**, 855 (2008).
[273] F. H. Vincent, H. Meheut, P. Varniere, and T. Paumard, Astronomy and Astrophysics **551**, A54 (2013).
[274] I. Z. Stefanov, Monthly Notices of the Royal Astronomical Society **444**, 2178 (2014).
[275] I. D. Novikov and V. P. Frolov, *Physics of black holes*, 1989.
[276] A. J. Castro-Tirado, S. Brandt, and N. Lund, IAU Circ. **5590** (1992).
[277] D. Steeghs, J. E. McClintock, S. G. Parsons, M. J. Reid, S. Littlefair, and V. S.

Dhillon, The Astrophysical Journal **768**, 185 (2013).
[278] J. M. Miller et al., The Astrophysical Journal Letters **775**, L45.
[279] W. Cui, S. N. Zhang, and W. Chen, The Astrophysical Journal Letters **492**, L53 (1998).
[280] M. A. Nowak, R. V. Wagoner, M. C. Begelman, and D. E. Lehr, The Astrophysical Journal Letters **477**, L91 (1997).
[281] K. P. Singh et al., In-orbit performance of SXT aboard AstroSat, in *Space Telescopes and Instrumentation 2016: Ultraviolet to Gamma Ray*, volume 9905 of *Proceedings of the SPIE*, page 99051E, 2016.
[282] P. C. Agrawal et al., Journal of Astrophysics and Astronomy **38**, 30 (2017).
[283] J. S. Yadav et al., The Astrophysical Journal **833**, 27 (2016).
[284] H. M. Antia et al., The Astrophysical Journal Supplement Series **231**, 10 (2017).
[285] V. K. Agrawal, A. Nandi, V. Girish, and M. C. Ramadevi, Monthly Notices of the Royal Astronomical Society **477**, 5437 (2018).
[286] T. Belloni, M. Klein-Wolt, M. Méndez, M. van der Klis, and J. van Paradijs, Astronomy and Astronomy **355**, 271 (2000).
[287] T. M. Belloni and D. Altamirano, Monthly Notices of the Royal Astronomical Society **432**, 10 (2013).
[288] T. E. Strohmayer, The Astrophysical Journal Letters **554**, L169 (2001).
[289] R. A. Remillard, X-ray QPOs from Black Hole Binary Systems, in *X-ray Timing 2003: Rossi and Beyond*, edited by P. Kaaret, F. K. Lamb, and J. H. Swank, volume 714 of *American Institute of Physics Conference Series*, pages 13–20, 2004.
[290] T. Belloni, P. Soleri, P. Casella, M. Méndez, and S. Migliari, Monthly Notices of the Royal Astronomical Society **369**, 305 (2006).
[291] A. A. Zdziarski, W. N. Johnson, and P. Magdziarz, Monthly Notices of the Royal Astronomical Society **283**, 193 (1996).
[292] R. Fender and T. Belloni, Annual Review of Astronomy and Astrophysics **42**, 317 (2004).

Vita

Md Ramiz Aktar was born on 2nd April, 1988 in Baduria, West bengal, India. He did his B.Sc. with Physics Honours in 2009 from Barasat Government College, under University of Calcutta and M.Sc. in physics from Acharya Prafullah Chandra College, New Barrackpore, under West Bengal State University in 2011. He had enrolled into the Ph.D programme at Indian Institute of Technology Guwahati in 2012. He had qualified Graduate Aptitude Test in Engineering (GATE) in 2012. He has earned the Senior Research Fellowship in 2014 by Indian Institute of Technology Guwahati.